On the Quasi One-Dimensional Structure of Two-Dimensional Cellular Detonations in a Duct

Christopher Uyeda

A thesis submitted in partial fulfillment of the requirements for the degree of

Master of Science in Aeronautics and Astronautics

University of Washington

2015

Committee:

Antonino Ferrante, Chair

Mitsuru Kurosaka

Program Authorized to Offer Degree:
William E. Boeing Department of Aeronautics & Astronautics

University of Washington

Abstract

On the Quasi One-Dimensional Structure of Two-Dimensional Cellular Detonations in a Duct

Christopher Uyeda

Chair of the Supervisory Committee:
Assistant Professor Antonino Ferrante
William E. Boeing Department of Aeronautics & Astronautics

Adaptive mesh refinement combined with a WENO-TCD hybrid numerical method are used to simulate cellular detonations in ducts using a detailed chemical mechanism linked to the inviscid Euler equations. Using this computational setup, we were able to reproduce the detonation cells and structure that other researchers have produced in their work and then used the results to validate what is called the cross-current dynamics theory, developed by Kurosaka & Tsuboi (2014). This theory uses the conservation laws, Rankine-Hugoniot jump condition, and detonation front curvature to determine the velocity directly behind the detonation front. Comparisons of the velocity ratio calculated from the cross-current dynamics theory and the data from the simulation verify the accuracy of the theory.

Next we simulate a detonation propagating from the closed end of a duct and compare the one-dimensional ZND solution, which we used to initiate the two-dimensional detonations, to the area-averaged properties and the properties of particles tracked along their pathlines from the detonation front to their sonic points. Despite the complex structures that appear within the detonation, the one-dimensional solution proves to also model the structure of the area-averaged and particle properties. Disagreements between the particle properties and the one-dimensional solution are concentrated near the detonation front where the transverse wave and Mach stem introduce larger jumps in the flow properties than in the one-dimensional case. We also show the particle pathlines are dominated by a one-dimensional motion with slight drifts in the vertical direction downstream from the detonation front. By reviewing the particles' v-velocity to u-velocity ratio in the reference frame attached to the detonation front, we observe the quick transition the particles experience from a two-dimensional to a quasi one-dimensional motion. These findings give us new found appreciation of the quasi one-dimensional nature of two-dimensional detonations.

TABLE OF CONTENTS

Page

List of Figures iii

List of Tables viii

Chapter 1: Introduction 1

Chapter 2: Detonation Background 3
  2.1 Experimental Observations of Detonations in a Duct 3
  2.2 Classical Detonation Theories 7

Chapter 3: Shockwave Cross-Current Dynamics Theory 15

Chapter 4: Mathematical Description 18
  4.1 AMROC Framework 18
  4.2 Reactive Euler Equation Formulation 19
  4.3 Computation of Pressure and Temperature 20
  4.4 Boundary Conditions 21
  4.5 WENO/TCD Method 23
  4.6 Chemistry Computations 27

Chapter 5: Two-Dimensional Detonations 28
  5.1 Two-Dimensional Detonations in an Open Ended Duct 28
  5.2 Two-Dimensional Detonations In Open/Closed Ended Duct 41

Chapter 6: Conclusions 68

Appendix A: Appendices 72
  A.1 Derivation of Analytical ZND Structure 72

A.2 Chemical Reaction 75
A.3 Cross-Current Dynamics 76
A.4 Area-Average with One Detonation Cell at Later Times 79
A.5 Area-Averages During Transient Phase of Mach 83
A.6 Detonations in Open/Closed Duct with Two Detonation Cells 87

LIST OF FIGURES

Figure Number Page

2.1 Half of the detonation front structure made up of an incident shock, transverse shock, Mach stem, and slip line. The intersection of the two shocks and wave is referred to as the triple point. 4

2.2 Soot track of a two-dimensional cellular detonation in a $2H_2 + O_2 + 7AR$ gaseous mixture from Strehlow (1968) 5

2.3 Detonation cell of height H and length L. The detonation front is overlayed on the first and last half of the detonation cell to show the change in configuration of the front. 6

2.4 ZND model which includes the shock, induction zone, and combustion zone. 10

2.5 One-dimensional structure of a detonation propagating in a duct from a wall with four distinct regions: initial unreacted region, ZND region, expansion wave region, and constant state region. The expansion wave begins behind the CJ-plane where the downstream flow may be assumed to be isentropic. 13

4.1 Schematic of the implementation of the slip-wall boundary condition. 22

4.2 Results of SOD Shocktube simulation using a second order WENO-TCD method compared to the analytical solution for u-velocity (a), density (b), and pressure (c). 26

5.1 The computational setup of detonations in a duct with two open ends. . . . 29

5.2 The one-dimensional ZND solution created from Shepard (2000) for (a) Mach, (b) u-velocity, (c) pressure, (d) density, and temperature (e) in the reference frame attached to the detonation front using the chemical mechanism by Boris *et al.* (1982). 31

5.3 The one-dimensional ZND solution created from Shepard (2000) for the species over the entire ZND region (a,b) and a magnified view at the detonation front (c,d) using the chemical mechanism by Boris *et al.* (1982). 32

5.4 a). Density schlieren contour and b). pressure contour of the detonation front at t = 240 μs. 33

5.5 a). Density schlieren contour and b). pressure contour of one detonation cell using the initial conditions in Table 5.1 in an open ended duct. Dimensions of the cell are 3 cm x 5.25 cm. 35

5.6 Cross-current u-velocity plotted with the numerical solution v-velocity at t = 232 μs (a), 240 μs (b), and 248 μs (c). 36

5.7 Cross-current v-velocity plotted with the numerical solution v-velocity at t = 232 μs (a), 240 μs (b), and 248 μs (c). 38

5.8 Cross-current ratio of v-velocity to u-velocity plotted with the numerical solution v-velocity as well as the slope curvature at t = 232 μs (a,b) and 240 μs (c,d). 40

5.9 Cross-current ratio of v-velocity to u-velocity plotted with the numerical solution v-velocity as well as the slope curvature at t = 248 μs. 41

5.10 Contours of the v-velocity to u-velocity ratio, in the reference frame attached to the detonation front, at t = 232 μs (a), 240 μs (b), and 248 μs (c). . . . 42

5.11 Contours of the density gradient magnitude at t = 232 μs (a), 240 μs (b), and 248 μs (c). 43

5.12 Contours of ω/ρ at t = 232 μs (a), 240 μs (b), and 248 μs (c). 44

5.13 Contours of pressure at t = 232 μs (a), 240 μs (b), and 248 μs (c). 45

5.14 The computational setup of detonations in a duct with an open and closed end. 46

5.15 a). Density schlieren contour and b). pressure contour of one detonation cell using the initial conditions in Table 5.1 in a duct with a closed and open end. Dimensions of the cell are 3 cm x 5.25 cm. 47

5.16 Area-averaged Mach (a) and u-velocity (b) in the reference frame attached to the detonation front compared to the computed one-dimensional ZND solution at t = 555 μs. 48

5.17 Area-averaged pressure (a), density (b), and temperature (c) compared to the computed one-dimensional ZND solution at t = 555 μs. 49

5.18 Area-averaged mass fraction of species compared to the computed one-dimensional ZND solution at t = 555 μs. 50

5.19 Area-averaged Mach and pressure in the reference frame attached to the detonation front compared to the computed one-dimensional ZND solution at t = 575 μs (a,b) and 605 μs (c,d). 52

5.20 Area-averaged Mach (a) and u-velocity (b) in the reference frame attached to the detonation front compared to the the analytical post CJ-structure at t = 555 μs. 53

5.21 Area-averaged pressure (a), density (b), and temperature (c) compared to the the analytical post CJ-structure at t = 555 μs. 54

5.22 Magnified view of the area-averaged Mach (a), pressure (b), density (c), and temperature (d) in the reference frame attached to the detonation front compared to the computed one-dimensional ZND solution and the analytical post CJ-structure at t = 555 μs. The sonic plane and CJ-plane are both also shown. 56

5.23 Visual representation of the particle tracking method. In the shock reference frame, the detonation front from the initial release time of the particles is shown. 57

5.24 (a) Zoomed in view of the origin of the particle pathlines and (b) detonation front reference frame of 7 particle pathlines tracked to the sonic point where the dashed black line represents the upper and lower walls of the duct. The particles were tracked from t = 270 μs to 645 μs. 58

5.25 Ratio of v-velocity to u-velocity, in the reference frame attached to the detonation front, of particles that are tracked from the detonation front to after the sonic plane. 59

5.26 Mach (a,b)) and u-velocity (c,d) in the reference frame attached to the detonation front of particles that are tracked from the detonation front to after the sonic plane are plotted with the area-averaged properties. 61

5.27 Pressure (a,b) and density (c,d) of particles that are tracked from the detonation front to after the sonic plane are plotted with the area-averaged properties. 62

5.28 Temperature of particles that are tracked from the detonation front to after the sonic plane. 63

5.29 Species mass fraction of particles that are tracked from the detonation front to after the sonic plane are plotted with the area-averaged properties. . . . 64

5.30 (a) Zoomed in view of the origin of the particle pathlines and (b) detonation front reference frame of multiple particle pathlines to their sonic point. The particles were tracked from t = 270 μs to 645 μs. 65

5.31 Ratio of v-velocity to u-velocity, in the reference frame attached to the detonation front (a), temperature (b), density (c), and pressure (d) of multiple particles that are tracked from the detonation front to after the sonic plane are plotted with the area-averaged properties. 66

5.32 Mach (a) and u-velocity (b), in the reference frame attached to the detonation front, of particles that are tracked from the detonation front to after the sonic plane are plotted with the area-averaged properties. 67

A.1 Pressure (a), u-velocity (b), and v-velocity (c) at t = 232 μs with an isoline indicating the end of the induction zone. 76

A.2 Pressure (a), u-velocity (b), and v-velocity (c) at t = 240 μs with an isoline indicating the end of the induction zone. 77

A.3 Pressure (a), u-velocity (b), and v-velocity (c) at t = 248 μs with an isoline indicating the end of the induction zone. 78

A.4 Area-averaged u-velocity (a), density (b), and temperature (c) compared to the computed one-dimensional ZND solution at t = 575 μs. 79

A.5 Area-averaged mass fraction of species compared to the computed one-dimensional ZND solution at t = 575 μs. 80

A.6 Area-averaged u-velocity (a), density (b), and temperature (c) compared to the computed one-dimensional ZND solution at t = 605 μs. 81

A.7 Area-averaged mass fraction of species compared to the computed one-dimensional ZND solution at t = 605 μs. 82

A.8 Area-averaged Mach in reference frame attached to detonation front compared to the computed one-dimensional ZND solution at t = 0 (a), 25 (b), 50 (c), and 75 (d) μs. 83

A.9 Area-averaged Mach in reference frame attached to detonation front compared to the computed one-dimensional ZND solution at t = 100 (a), 125 (b), 150 (c), and 175 (d) μs. 84

A.10 Area-averaged pressure compared to the computed one-dimensional ZND solution at t = 0 (a), 25 (b), 50 (c), and 75 (d) μs. 85

A.11 Area-averaged pressure compared to the computed one-dimensional ZND solution at t = 100 (a), 125 (b), 150 (c), and 175 (d) μs. 86

A.12 The computational setup of detonations in a duct with an open and closed end that produced two detonation cells. 87

A.13 a). Density schlieren contour and b). pressure contour of the detonation front at t = 266 μs with two cells. 88

A.14 Area-averaged Mach (a) and u-velocity (b) in the reference frame attached to the detonation front compared to the computed one-dimensional ZND solution and the analytical post CJ-structure at t = 266 μs. 89

A.15 Area-averaged pressure (a), density (b), and temperature (c) compared to the computed one-dimensional ZND solution and the analytical post CJ-structure at t = 266 μs. 90

A.16 Area-averaged Mach (a) and u-velocity (b) in the reference frame attached to the detonation front compared to the computed one-dimensional ZND solution and the analytical post CJ-structure at t = 670 μs. 91

A.17 Area-averaged pressure (a), density (b), and temperature (c) compared to the computed one-dimensional ZND solution and the analytical post CJ-structure at t = 670 μs. 92

A.18 Magnified view at t = 690 μs of the area-averaged Mach (a), pressure (b), density (c), and temperature (d) in the reference frame attached to the detonation front compared to the computed one-dimensional ZND solution and the analytical post CJ-structure. The sonic plane and CJ-plane are both also shown. 93

A.19 a). Shock reference frame of 7 particle paths and b). zoomed in view of the origin of the particle paths. The particles were tracked from t = 275 μs to 690 μs. 94

A.20 Flow properties of 7 randomly chosen particles that are tracked from the detonation front to after the sonic plane are plotted with the area-average for Mach (a) and u-velocity (b) in the reference frame attached to the shock. . 94

A.21 Flow properties of 7 randomly chosen particles that are tracked from the detonation front to after the sonic plane are plotted with the area-average for pressure (a), density (b), and temperature (c). 95

A.22 a). Shock reference frame of multiple particle paths and b). zoomed in view of the origin of the particle paths. The particles were tracked from t = 275 μs to 690 μs. 96

LIST OF TABLES

Table Number Page

4.1 Initial properties used to initiate the left and right side of the SOD Shocktube simulation. 27

5.1 Initial conditions for simulation 1. 29

5.2 AMR tolerances 30

ACKNOWLEDGMENTS

First I wish to express my sincere appreciation to Assistant Professor Antonino Ferrante for taking me on as a student, mentoring me throughout my research and thesis, and providing me with the tools needed to reach this point in my academic career. I also wish to express appreciation to Professor Mitsuru Kurosaka for mentoring me in the field of detonations, a field that was unfamiliar to me two years ago. Finally, without the work of Dr. Deiterding in creating the AMROC framework, none of my work could have been accomplished.

I am grateful for the individuals in my research group and friends that made my academic experience enjoyable. I would like to acknowledge Sean McMahon who layed the foundation of the detonation code for my use and to Barrett McCann for his guidance when I had troubles with the AMROC framework. Finally I would like to thank Michael Dodd and Eric Lovejoy for their support when I first began my computational studies.

DEDICATION

to my forever supporting parents, Derek and Hyun Sook, and loving brother, Brian.

Chapter 1

INTRODUCTION

The flow properties of detonations in a constant area duct has long been studied and proven to be an extremely complex process which involves chemical kinetics and hydrodynamic flows. Because studying the internal hydrodynamic properties are quite difficult in experiments, many researchers turn to simulations. Many have been successful in the reproduction of the detonation phenomena in simulations and have used these to make advancements in the field. They are able to study the internal process of detonations with great precision, specifically, the area behind the detonation front. This area downstream of the detonation front has many complex structures which include the triple point, shear layers, and unburned pockets. These components all directly play a role in the behavior of the detonation.

Despite all the complex features of a detonation, many researchers have proven that the simple Chapman-Jouguet theory does predict the average propagation speed of the detonation front. They have also recreated the detonation cells that are observed in experiments with a reasonable amount of accuracy. Instead of attempting to understand each individual complex feature, we will attempt to shed light on the quasi one-dimensional behavior of a two-dimensional detonation. We will initiate the two-dimensional detonation using the one-dimensional ZND solution with an initial perturbation and compare the ZND solution to the area-averaged flow structure and the structure of the particle properties as they are tracked downstream from the detonation front. Few researchers, such as Radulescu, Sharpe, Law & Lee (2007), have used this approach by comparing the area-averaged properties of a two-dimensional detonation, initiated with a different one-dimensional solution, to the classical ZND detonation theory; however, their simulations do not account for the complex chemical kinetics and they do not compare their results with the one-dimensional structure they initiated the detonation with. Rather than using a single irreversible step reaction to model the reactions, we account for the many complex chemical kinetics that occur which yields more accurate results. In addition, we adopt the AMROC framework, developed by Deiterding (2003), to employ adaptive mesh refinement for efficiently capturing the complex features of a detonation.

Chapter 2

DETONATION BACKGROUND

In this chapter, we will summarize past findings from detonation experiments in ducts and the classical detonation theories that laid the foundation for all prospective detonation research. The observations from detonation experiments in a rectangular duct will be presented in Sec. 2.1 which include the structure of the detonation front and the appearance of detonation cells. In Sec. 2.2, the classical detonation theories will be discussed to lay the groundwork for presenting the results. These include the CJ-theory, the ZND model, and the post CJ-structure. We will provide an adequate summary of the derivations while pointing to the research papers and books for details.

2.1 Experimental Observations of Detonations in a Duct

2.1.1 Detonation Front

In a two-dimensional detonation, a distinct structure appears at the head of the detonation wave which is made up of a slip line and three different waves as indicated in Fig. 2.1: incident shock, transverse wave, and Mach stem. The incident shock and Mach stem are both adiabatic shock waves that make up the front of the detonation front where the incident shock is essentially a normal shock and the Mach stem may be considered as an oblique shock. Consequently, the Mach stem is stronger and dissociates the chemical reactants faster than the incident shock, so the induction zone behind the Mach stem is smaller than the induction zone behind the incident shock. The line that divides the material passing through the Mach stem from the incident shock and transverse wave is the slip line, or shear line. This fact is highlighted in Fig. 2.1 by the jump in the induction zone length across the slip line.

The transverse wave extends laterally from the point that the incident shock and Mach

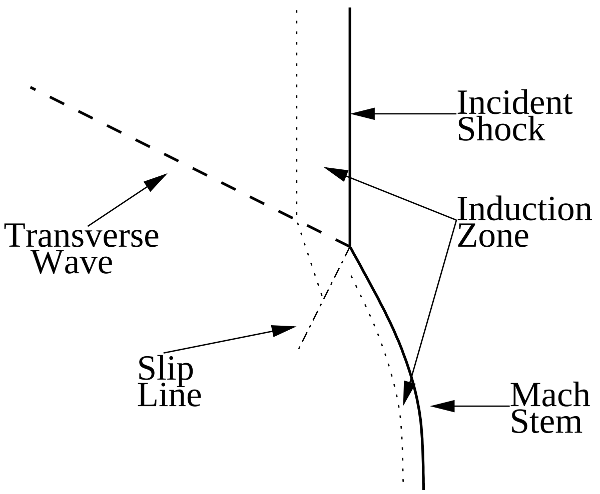

Figure 2.1: Half of the detonation front structure made up of an incident shock, transverse shock, Mach stem, and slip line. The intersection of the two shocks and wave is referred to as the triple point.

stem meet, formally known as the triple point, and moves laterally along the shock front until it collides with another transverse wave or a wall. The strength of the tranverse wave decays away from the detonation front because there is less fresh reactants and the pressure gradient behind the Mach stem and incident shock converge behind the front. The movement of the transverse waves control the convex curvature of the Mach stem such that as the transverse waves move apart, the Mach stem's curvature slowly degrades until it eventually becomes an incident shock. Due to this movement of the transverse wave, the detonation front structure is unsteady; however, it has been pointed out that the flow close to the triple point is almost steady Fickett & Davis (1979).

2.1.2 Detonation Cells

Movement of the transverse waves up and down the forward moving detonation front also corresponds to the movement of the triple points. As the triple points move up and down, they eventually intersect each other and define a cellular structure. Consequently, the cellular structure is simply the triple point tracks and they have been visualized in experiments by

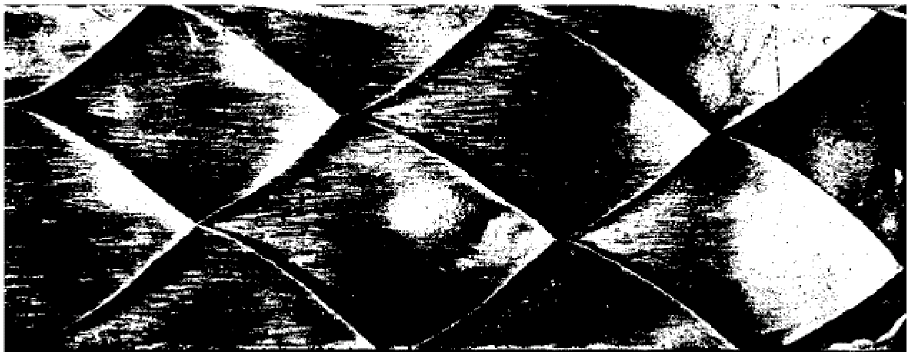

Figure 2.2: Soot track of a two-dimensional cellular detonation in a $2H_2 + O_2 + 7AR$ gaseous mixture from Strehlow (1968)

using a coat of soot along the rectangular duct's walls as shown in Fig. 2.2 from an experiment conducted by Strehlow (1968). It has been noted that these cells only regularly appear when the duct height is approximately the height of the detonation cell.

Currently, one of the most widely used methods for characterizing a detonation in a rectangular duct is by the cell's characteristic length, L, and height, H, because the details of the complex flow are difficult to measure. The ratio of the length and height of the detonation cells are related to the ratio of the propagation speed of the detonation front to the transverse waves. Figure 2.3 illustrates the dimensions of the detonation cell along with the change in the configuration of the detonation front from the first to last half of the cell. The change in the detonation front configuration is a result of the triple points moving away, first half of cell, or towards, last half of cell, each other. The Mach stem and incident shock switch at the peak height of the cell when the triple points switch from moving apart to moving towards each other.

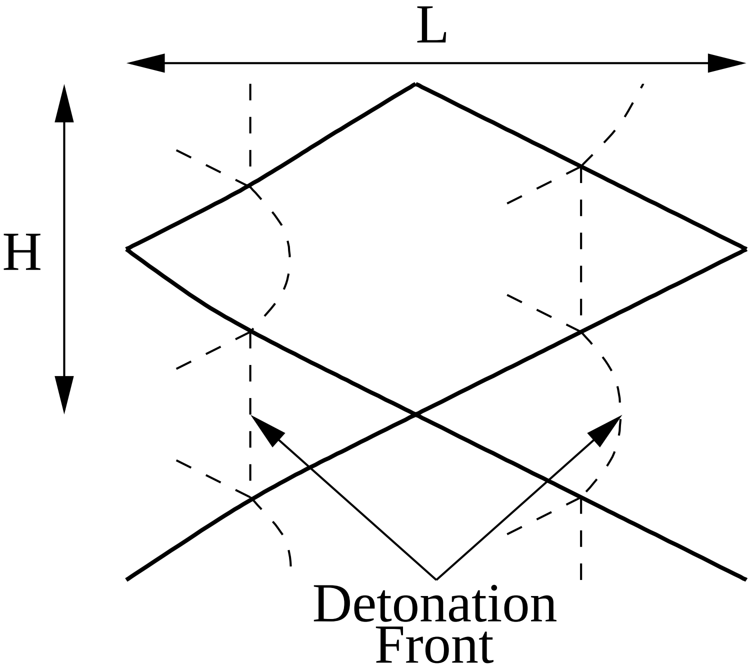

Figure 2.3: Detonation cell of height H and length L. The detonation front is overlayed on the first and last half of the detonation cell to show the change in configuration of the front.

2.2 *Classical Detonation Theories*

2.2.1 Chapman-Jouget Detonation Theory

The most simple detonation model was first developed by Chapman (1905) and Jouguet (1917) and is known as the Chapman-Jouguet (CJ) theory. This model assumes the flow is one-dimensional, the detonation front is a jump discontinuity through which the chemical reaction is completed instantaneously, and the jump discontinuity is steady. Under these assumptions, the conservation laws may be solved with the propagation speed of the detonation front, $\mathrm{D_{CJ}}$, to the final reacted state, as detailed in Fickett & Davis (1979). The minimum value solution to this problem is known to be the CJ-state and it should be noted that the boundary condition behind the detonation front determines $\mathrm{D_{CJ}}$.

To determine the CJ-state properties, the conservation laws in the reference frame attached to the shock, assuming an ideal gas, are first defined by

$$\rho_0 \mathrm{D_{CJ}} = \rho(\mathrm{D_{CJ}} - u) \tag{2.1}$$

$$\mathrm{p} - \mathrm{p_0} = \rho_0 u \mathrm{D_{CJ}} \tag{2.2}$$

$$e_0 + \frac{p_0}{\rho_0} + \frac{1}{2}\mathrm{D_{CJ}^2} = e + \frac{p}{\rho} + \frac{1}{2}\left(\mathrm{D_{CJ}} - u\right)^2 \tag{2.3}$$

where ρ is the density of the fluid, p is the pressure of the fluid, u is the bulk velocity of the fluid in the absolute reference frame, e is the specific internal energy, and subscript 0 represent the initial state, or the state ahead of the detonation front. The energy conservation equation, Eqn. (2.3), may be rewritten with enthalpy, $h = e + p/\rho$,

$$h_0 + \frac{1}{2}\mathrm{D_{CJ}^2} = h + \frac{1}{2}\left(\mathrm{D_{CJ}} - u\right)^2 \tag{2.4}$$

The enthalpy of the ith species can be split into its formation, $\mathrm{h}^o_{\mathrm{f}_i}$, and sensible, $\mathrm{h}_{\mathrm{s}_i}$ enthalpies given by

$$\mathrm{h}_i(\mathrm{T}) = \mathrm{h}^o_{f_i} + h_{\mathrm{s}_i} = \mathrm{h}^o_{f_i} + \int_{\mathrm{T}_o}^{\mathrm{T}} c_{p_i}(\mathrm{T})dT \tag{2.5}$$

where T is the bulk temperature, $c_{p_i}(\mathrm{T})$ is the heat capacity at constant pressure of the ith species, $\mathrm{h}^o_{f_i}$ is the enthalpy of the ith species created at standard temperature and pressure (STP), and $\mathrm{h}_{\mathrm{s}_i}$ is the difference in enthalpy of the ith species at a specified temperature and $\mathrm{h}^o_{f_i}$. The bulk enthalpy is related to the individual species enthalpy by

$$h = \sum_{i=1}^{S} \rho_i h_i = \sum_{i=1}^{S} \rho_i(\mathrm{h}^o_{f_i} + h_{\mathrm{s}_i}) \tag{2.6}$$

where S is the number of species in the reaction of interest. The resulting energy conservation equation becomes

$$h_{s_0} + q + \frac{1}{2}\mathrm{D}^2_{\mathrm{CJ}} = h_s + \frac{1}{2}\left(\mathrm{D}_{\mathrm{CJ}} - u\right)^2 \tag{2.7}$$

where the heat release, q, is

$$q = \sum_{i}^{reactants} Y_i h^o_{f_i} - \sum_{i}^{products} Y_i h^o_{f_i} \tag{2.8}$$

where Y_i is the mass fraction of the ith species. Manipulation of the conservation laws for mass and momentum, Eqn. (2.1) and (2.2), gives an equation for the Rayleigh line, $\Re$

$$\Re = \rho_0^2 {\mathrm{D}_{\mathrm{CJ}}}^2 - (\mathrm{p} - \mathrm{p}_0)/\left(\frac{1}{\rho_0} - \frac{1}{\rho}\right) = 0 \tag{2.9}$$

and manipulation of the energy equation, Eqn. (2.3), gives an equation for the Hugoniot curve, H

$$H = e - e_0 - \frac{1}{2}(\mathrm{p} + \mathrm{p}_0)\left(\frac{1}{\rho_0} - \frac{1}{\rho}\right) \tag{2.10}$$

The CJ-point is where both the Rayleigh line and Hugoniot curve are tangent on a p - $1/\rho$ diagram. Using this result, expressions may be derived for pressure, density, velocity in the absolute reference frame, and the speed of sound at the CJ-point as detailed by Fickett & Davis (1979)

$$\mathrm{p_{CJ}} = \rho_0 \frac{\mathrm{D_{CJ}^2}}{\gamma_{\mathrm{CJ}}+1} \tag{2.11}$$

$$\rho_{\mathrm{CJ}} = \rho_0 \frac{\gamma_{\mathrm{CJ}}}{\gamma_{\mathrm{CJ}}+1} \tag{2.12}$$

$$\mathrm{u_{CJ}} = \frac{\mathrm{D_{CJ}}}{\gamma_{\mathrm{CJ}}+1} \tag{2.13}$$

$$a_{\mathrm{CJ}} = \frac{\mathrm{D_{CJ}}\gamma_{\mathrm{CJ}}}{\gamma_{\mathrm{CJ}}+1} \tag{2.14}$$

where γ_{CJ} is γ at the CJ-point. The energy conservation equation in the form of Eqn. (2.7) can be manipulated for the detonation wave such that it is in terms of a nondimensionalized heat release term, q^*, $\mathrm{M_{CJ}}$, and an arbitrarily chosen M, where M = 1 ideally corresponds to the end of the chemical reactions

$$q^* = \frac{q}{\mathrm{c_p T_1}} = \left(\frac{1+\gamma \mathrm{M_{CJ}^2}}{1+\gamma \mathrm{M^2}}\right)^2 \left(\frac{\mathrm{M}}{\mathrm{M_{CJ}}}\right)^2 \left(1+\frac{\gamma-1}{2}\mathrm{M^2}\right) - \left(1+\frac{\gamma-1}{2}\mathrm{M_{CJ}^2}\right) \tag{2.15}$$

When the above relation is solved for $\mathrm{M_{CJ}}$ in terms of q from the entire chemical reaction by setting M = 1 the following expression is yielded

$$\mathrm{M_{CJ}} = \sqrt{1+\frac{q(\gamma^2-1)}{2a_0^2}} + \sqrt{\frac{q(\gamma^2-1)}{2a_0^2}} \tag{2.16}$$

where a_0 is the speed of sound ahead of the detonation front.

2.2.2 Zel'dovich-Von Neumann-Döring Detonation Model

The ZND model, Fig. 2.4, was proposed independently by Zel'dovich, von Neumann, and Döring. The basis of this model are the Euler equations in which an adiabatic shock moves through unreacted chemical reactants. The chemical mixture undergo the typical adiabatic shock jump conditions to the Von-Nuemann (VN) state across the shock moving at $\mathrm{M_{CJ}}$.

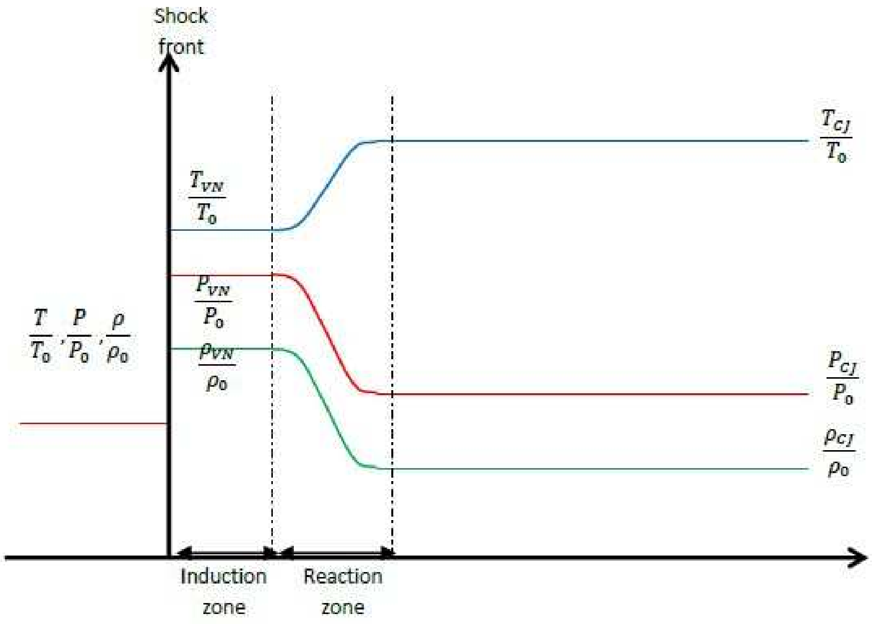

Figure 2.4: ZND model which includes the shock, induction zone, and combustion zone.

$$\begin{aligned} \mathrm{M_{VN}} &= \sqrt{\frac{(\gamma-1)\mathrm{M_{CJ}^2}+2}{2\gamma\mathrm{M_{CJ}^2}-(\gamma-1)}} \\ \frac{\mathrm{p_{VN}}}{\mathrm{p_0}} &= \frac{2\gamma\mathrm{M_{CJ}^2}-(\gamma-1)}{\gamma+1} \\ \frac{\rho_{\mathrm{VN}}}{\rho_0} &= \frac{(\gamma+1)\mathrm{M_{CJ}^2}}{(\gamma-1)\mathrm{M_{CJ}^2}+2} \\ \frac{\mathrm{T_{VN}}}{\mathrm{T_0}} &= \frac{[2\gamma\mathrm{M_{CJ}^2}-(\gamma-1)][(\gamma-1)\mathrm{M_{CJ}^2}+2]}{(\gamma+1)^2\mathrm{M_{CJ}^2}} \end{aligned} \tag{2.17}$$

The large pressure and temperature rise in the chemical reactants break up the chemical reactants into their reactive counterparts over a finite distance. The distance between the shock front and end of the chemical reactant breakup is known as the induction zone. Because the dissociation of the chemical species are highly dependent on the pressure jump across the shock, the length of the induction zone is driven by the strength of the shock and is typically very small. Naturally, the length of the induction zone is a characteristic used to describe the strength of the detonation.

After the complete break up of the reactants, the combustion of the highly reactive species begins in the region known as the reaction zone. In the ZND model, the chemical reaction is no longer observed as a single step reaction that the CJ-theory utilized, but rather a multi-step reaction over a distinct reaction zone length where heat is continuously added into the system. The evolution of the reaction may be characterized by the progress variable, λ, where $\lambda = 0$ corresponds to completely unreacted and $\lambda = 1$ corresponds to a fully reacted chemical mixture. Typically the combustion continues until the burning has ceased to a finalized downstream state, defined by the CJ-theory.

Using λ, the flow properties at any point in the reaction zone may be determined if λ is known at that point. The derivations of these equations are given in Appendix A.1

$$M = \sqrt{\frac{1 + \mathrm{M}_{\mathrm{CJ}}^2 \gamma^2 (\sqrt{1-\lambda} - \mathrm{M}_{\mathrm{CJ}}^2 (\sqrt{1-\lambda} - 1)) + \sqrt{1-\lambda} - \mathrm{M}_{\mathrm{CJ}}^2 \sqrt{1-\lambda}}{1 + \gamma(-\gamma + 2\mathrm{M}_{\mathrm{CJ}}^2 (1+\gamma) + (\mathrm{M}_{\mathrm{CJ}}^2 - 1)^2 \gamma\lambda} + \frac{\gamma(1 + \sqrt{1-\lambda} - \lambda + 2\mathrm{M}_{\mathrm{CJ}}^2 \lambda - \mathrm{M}_{\mathrm{CJ}}^4 (\lambda + \sqrt{1-\lambda} - 1))}{1 + \gamma(-\gamma + 2\mathrm{M}_{\mathrm{CJ}}^2 (1+\gamma) + (\mathrm{M}_{\mathrm{CJ}}^2 - 1)^2 \gamma\lambda}} \tag{2.18}$$

$$\frac{\mathrm{p}}{\mathrm{p}_{\mathrm{VN}}} = \frac{1 + \mathrm{M}_{\mathrm{CJ}}^2 \gamma (1 + \sqrt{1-\lambda}) - \gamma\sqrt{1-\lambda}}{1 + (2\mathrm{M}_{\mathrm{CJ}}^2 - 1)\gamma} \tag{2.19}$$

$$\frac{\rho}{\rho_{\mathrm{VN}}} = \frac{2 + \mathrm{M}_{\mathrm{CJ}}^2 (\gamma - 1)}{1 + \mathrm{M}_{\mathrm{CJ}}^2 (\gamma - \sqrt{1-\lambda}) + \sqrt{1-\lambda}} \tag{2.20}$$

$$\frac{\mathrm{T}}{\mathrm{T}_{\mathrm{VN}}} = \frac{(1 + \mathrm{M}_{\mathrm{CJ}}^2 (\gamma - \sqrt{1-\lambda}) + \sqrt{1-\lambda})(1 + \mathrm{M}_{\mathrm{CJ}}^2 \gamma (1 + \sqrt{1-\gamma}) - \gamma\sqrt{1-\lambda})}{(2 + \mathrm{M}_{\mathrm{CJ}}^2 (\gamma - 1))(1 + \gamma(2\mathrm{M}_{\mathrm{CJ}}^2 - 1))} \tag{2.21}$$

2.2.3 Post CJ-Structure

After the CJ state has been reached, the chemical reaction ceases and the downstream flow is assumed isentropic. In the one-dimensional case, where the detonation propagates away from a wall, there are two distinct acoustic waves that characterize the structure behind the CJ-plane as shown in Fig. 2.5. An analytical solution was determined by Browne, Ziegler & Shepherd (2004) by combining the CJ detonation model and Taylor-Zeldovich (TZ) similarity solution. We will briefly summarize their discussion while details may be found in their paper.

The method of characteristics is used to define the structure in the expansion wave. The two characteristics are first defined by

$$\begin{aligned} C^+ : \quad & \frac{dx}{dt} = u + a \\ C^- : \quad & \frac{dx}{dt} = u - a \end{aligned} \tag{2.22}$$

with Riemann invariants on the characteristics defined by

$$\begin{aligned} J^+ &= u + \frac{2a}{\gamma - 1} \\ J^- &= u - \frac{2a}{\gamma - 1} \end{aligned} \tag{2.23}$$

where γ is γ at the CJ-point. We assume γ to remain constant because of our isentropic assumption. The C^+ characteristics are illustrated by the dotted lines than span through the expansion wave from the origin and from the wall in the constant state region in Fig. 2.5.b. The equations that define the C^+ charactierstics are defined by

$$\begin{aligned} \frac{dx}{dt} = u + a = \frac{x}{t} \quad for \;\; a_3 < \frac{x}{t} < \mathrm{D_{CJ}} \\ \frac{dx}{dt} = a_3 \quad for \;\; 0 < \frac{x}{t} < a_3 \end{aligned} \tag{2.24}$$

where a_3 is the speed of sound in the constant state region where $u = 0$. The J^- Riemann invariant is constant along the C^- characteristics that span the expansion wave and constant state region. We utilize the J^- invariant to determine a_3 by defining the invariant by the properties at the CJ-point, state 2, and constant state region, state 3

$$J^- = u - \frac{2}{\gamma - 1}a = u_2 - \frac{2}{\gamma - 1}a_{\mathrm{CJ}} = -\frac{2}{\gamma - 1}a_3 \tag{2.25}$$

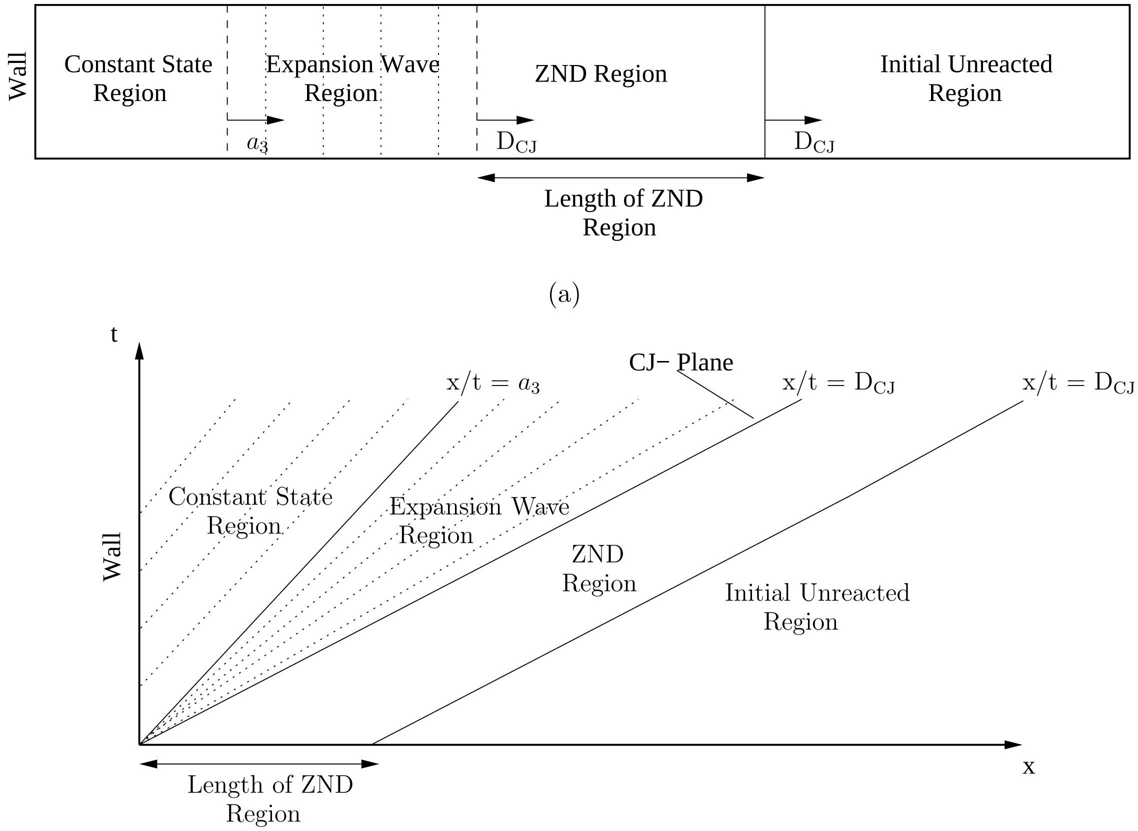

(a)

(b)

Figure 2.5: One-dimensional structure of a detonation propagating in a duct from a wall with four distinct regions: initial unreacted region, ZND region, expansion wave region, and constant state region. The expansion wave begins behind the CJ-plane where the downstream flow may be assumed to be isentropic.

where from the CJ condition

$$u_2 = \mathrm{D_{CJ}} - a_{\mathrm{CJ}} \tag{2.26}$$

The speed of sound in the constant state region can now be solved for

$$a_3 = \frac{\gamma + 1}{2} a_{\mathrm{CJ}} - \frac{\gamma - 1}{2} \mathrm{D_{CJ}} \tag{2.27}$$

Now the speed of sound structure within the expansion wave may be determined by use of the C^+ characteristic's similarity solution and the C^- characteristic Riemann invariants to be

$$a = a_3 \left[1 - \frac{\gamma - 1}{\gamma + 1}\left(1 - \frac{x}{a_3 t}\right)\right] \tag{2.28}$$

and the velocity in the absolute reference frame by

$$u = \frac{2a_3}{\gamma + 1}\left(\frac{x}{a_3 t} - 1\right) \tag{2.29}$$

The above relations can then be used to get the Mach relations by

$$\mathrm{M} = \frac{u}{a} \tag{2.30}$$

Because the flow is assumed to be isentropic, we may use isentropic relations to determine the temperature, pressure, and density from the speed of sound solution by

$$\frac{a}{a_3} = \left(\frac{\mathrm{T}}{\mathrm{T}_3}\right)^{\frac{1}{2}} = \left(\frac{\rho}{\rho_3}\right)^{\frac{\gamma-1}{2}} = \left(\frac{\mathrm{p}}{\mathrm{p}_3}\right)^{\frac{\gamma-1}{2\gamma}} \tag{2.31}$$

The temperature, pressure, and density in the constant state region are determined by Eqn. (2.31) with the speed of sound at the CJ-point, $a = a_{\mathrm{CJ}}$, and in the constant state region, a_3.

Chapter 3

SHOCKWAVE CROSS-CURRENT DYNAMICS THEORY

In this chapter we will briefly introduce the cross-current dynamics theory detailed by Kurosaka & Tsuboi (2014). The motion behind the detonation front is assumed to be structured fluid movement that is a result of the fluid particles moving through the detonation front. This motion is what will be defined as the cross-current dynamics. Normal shock wave jump relations will be used to derive the trajectory of the fluid particles through the detonation front which is sustained by the pressure gradient across and downstream of the detonation front. The transverse cross-current dynamics will be shown to not only rely on the pressure gradient, but also on the curvature of the detonation front through which the fluid particles are deflected through.

The two-dimensional Euler equations are used to describe the flow and are written in the cartesian coordinate system as

$$\begin{aligned}\frac{\partial \rho}{\partial t} + \nabla \cdot \rho \mathbf{u} &= 0 \\ \rho \frac{\mathrm{D}\mathbf{u}}{\mathrm{D}t} &= -\nabla \mathrm{p} \\ \rho \frac{\mathrm{D}h_t}{\mathrm{D}t} &= \frac{\partial \mathrm{p}}{\partial t}\end{aligned} \tag{3.1}$$

where $\frac{\mathrm{D}}{\mathrm{D}t} = \frac{\partial}{\partial t} + u\frac{\partial}{\partial x} + v\frac{\partial}{\partial y}$, $\mathbf{u} = (u, v)$, and h_t is the total enthalpy defined by

$$h_t = h_f + h_s + \frac{\mathbf{u^2}}{2} \tag{3.2}$$

Now we will derive the unit normal vector, $\mathbf{n}$, along the detonation front. First the detonation front shape is defined by

$$x = f_s(y;t) \tag{3.3}$$

where f_s is the distance from the vertical plane attached to the triple point that propagates with velocity $\mathbf{D} = (\mathrm{D_x}, \mathrm{D_y})$. In this representation, $f_s \approx 0$ along the incident shock and $f_s > 0$ along the Mach stem. Rewriting Eqn. (3.3) in terms of another arbitrary function, F, gives

$$F(x,y;t) = x - f_s(y;t) = 0 \tag{3.4}$$

such that the unit normal vector may be written

$$\mathbf{n} = \frac{\nabla F}{|\nabla F|} = \frac{\mathbf{e}_x - \frac{\partial f_s}{\partial y}\mathbf{e}_y}{\sqrt{1 + \left(\frac{\partial f_s}{\partial y}\right)^2}} \tag{3.5}$$

where $\frac{\partial f_s}{\partial y}$ is the slope of the detonation front. Now we define the relative velocity in the reference frame attached to the detonation front

$$\mathbf{u}' = \mathbf{u} - \mathbf{D} \tag{3.6}$$

The Rankine-Hugoniot jump condition for momentum is now used to relate the properties ahead, subscript 0, and behind, subscript 1, of the shock. The normal component is written as

$$(\mathrm{p}_1 - \mathrm{p}_0)\mathbf{n} = \rho_0 u'_{n0}(u'_{n0} - u'_{n1})\mathbf{n} \tag{3.7}$$

where subscript n indicates the normal component. The tangential component is given by

$$(u'_{t0} - u'_{t1})\mathbf{t} = 0 \tag{3.8}$$

where $\mathbf{t}$ is the unit tangent vector and subscript t indicates the tangent component. By combining Eqn. (3.7) and (3.8) along with Eqn. (3.6), the momentum jump condition may be written as

$$(\mathrm{p}_1 - \mathrm{p}_0)\mathbf{n} = \rho_0 u'_{n0}(\mathbf{u}'_0 - \mathbf{u}'_1) = \rho_0 u'_{n0}(\mathbf{u}_0 - \mathbf{u}_1) = \rho_0 u'_{n0}(-\mathbf{u}_1) \tag{3.9}$$

where the flow ahead of the detonation front is assumed to be static, $|\mathbf{u}_0| = 0$, and u'_{n0} is given by

$$u'_{n0} = -\mathbf{D} \cdot \mathbf{n} = \frac{-\mathrm{D}_x + \frac{\partial f_s}{\partial y}\mathrm{D}_y}{\sqrt{1 + \left(\frac{\partial f_s}{\partial y}\right)^2}} \tag{3.10}$$

Finally substituting Eqn. (3.10) and (3.5) into (3.9) will give the x-component of the cross-current velocity directly behind the detonation front by

$$u_1 = \frac{\mathrm{p}_1 - \mathrm{p}_0}{\rho_0 \left(\mathrm{D}_x - \mathrm{D}_y \frac{\partial f_s}{\partial y}\right)} \tag{3.11}$$

and the y-component by

$$v_1 = -\frac{(\mathrm{p}_1 - \mathrm{p}_0)\frac{\partial f_s}{\partial y}}{\rho_0 \left(\mathrm{D}_x - \mathrm{D}_y \frac{\partial f_s}{\partial y}\right)} \tag{3.12}$$

Typically $(\mathrm{D}_x - \mathrm{D}_y \frac{\partial f_s}{\partial y}) > 0$ which indicates that the pressure gradient, $\mathrm{p}_1 - \mathrm{p}_0$, is the driving factor of the absolute magnitude of the cross-current velocity. In the transverse direction, the curvature of the detonation front will dictate the direction of the cross-current velocity because the pressure gradient is typically positive across a shock. Therefore, the cross-current velocity in the transverse direction should be expected to be at a minimum along the incident shock and peak of the Mach stem where the slope is essentially zero, and at a maximum where the slope is greatest on the Mach stem.

Chapter 4

MATHEMATICAL DESCRIPTION

In this chapter, the details of the computational model will be discussed. We will first discuss the AMROC framework that we utilize because of its AMR capabilities in Sec. 4.1. The governing Euler equations will be discussed in Sec. 4.2 along with details for the additional equations that are required to model the development of the chemical species and how the new equations are integrated with the original Euler equations. In Sec. 4.3 we discuss how pressure and temperature are evaluated implicitly after the Euler equations are solved at each timestep. We will then discuss boundary conditions in Sec. 4.4 and the WENO/TCD method that we use in Sec. 4.5. Finally we will briefly explain how we resolve the chemical kinetics using Chemkin in Sec. 4.6.

4.1 AMROC Framework

Detonations contain multiple discontinuities and regions that require an increased mesh resolution to accurately solve the flow. The region behind the detonation front contains small scale chemical kinetics where a fine mesh allows these reactions to be adequately solved. An increased resolution is also preferred around the detonation front, transverse wave, shear layers, and unreacted pockets to avoid the diffusion of these discontinuities. To meet these requirements in an efficient manner, we employ the AMROC framework developed by Deiterding (2003) which is based on the AMR algorithms by Berger & Oliger (1984). With the AMR method, we are able to refine the mesh around discontinuities and chemical reactions while using a coarse mesh in the initial region and region after chemical reactions have ceased.

4.2 Reactive Euler Equation Formulation

Before defining the governing equations in detail, the vector of conserved quantities must first be defined

$$\mathbf{q}(\mathbf{x},t) = [\rho, m_1, ..., m_{\mathrm{d}}, \rho e, \rho_1, ..., \rho_S]^{\mathrm{T}} = [\rho, \rho u_1, ..., \rho u_{\mathrm{d}}, \rho e, \rho_1, ..., \rho_S]^{\mathrm{T}} \tag{4.1}$$

where d is the space dimensions and S is the number of species. It can now be seen that the size of the vector of conserved quantites is 2 + d + S. The total density, ρ, is related to the species densities by

$$\rho = \sum_{i=1}^{S} \rho_i \tag{4.2}$$

where ρ_i is the density of the ith species.

The governing equation for detonating flows are the reactive Euler equations for multiple species with reactive source terms (Lee, 2008) which is written as

$$\begin{aligned} \frac{\partial \rho}{\partial t} + \frac{\partial \rho u_k}{\partial k} &= 0, \\ \frac{\partial(\rho u_j)}{\partial t} + \frac{\partial(\rho u_j u_k)}{\partial k} + \frac{\partial \mathrm{p}}{\partial k} &= 0, \\ \frac{\partial(E)}{\partial t} + \frac{\partial[u_k(E+\mathrm{p})]}{\partial k} &= 0, \\ \frac{\partial(\rho_i)}{\partial t} + \frac{\partial(\rho_i u_k)}{\partial k} &= \dot{\omega}_i, \qquad i = 1, ..., S \end{aligned} \tag{4.3}$$

where u_k and u_j are the fluid velocity component in the kth and jth directions, E is the total energy (internal and kinetic), and p is the hydrostatic pressure. The total energy is defined by its internal and kinetic components

$$E = \rho e = \rho \sum_{i=1}^{S} \mathrm{Y}_i \mathrm{h_i(T)} - \mathrm{p} + \frac{1}{2}\rho \sum u_k^2, \qquad i = 1, ..., S \tag{4.4}$$

where e is the specific total energy and $\mathrm{h}_i(\mathrm{T})$ is the specific enthalpy of the ith species defined by Eqn. (2.5). The reaction rate of the ith species, $\dot{\omega}_i$, is determined by chemical kinetics as

$$\dot{\omega} = m_i \sum_{j=1}^{J} \left(\nu_{ji}^r - \nu_{ji}^f\right) \left[k_i^f \prod_{l=1}^{S} \left(\frac{\rho_l}{m_l}\right)^{\nu_{jl}^f} - k_j^r \prod_{l=1}^{S} \left(\frac{\rho_l}{m_l}\right)^{\nu_{jl}^r}\right], \qquad i = 1, ..., S \tag{4.5}$$

where ν_{ji}^r and ν_{ji}^f are, respectively, the forward and backward stoichiometric coefficients of the ith species in the jth reaction, and k_i^f and k_j^r are, respectively, the forward and backward reaction rates of the jth reaction. The forward and backward reaction rates are computed by the Arrhenius law for the jth reaction

$$k_j = A_j \mathrm{T}^{\beta_j} exp\left(-\frac{Ea_j}{\mathcal{R}\mathrm{T}}\right) \tag{4.6}$$

where A_j and β_j are experimentally determined constants of the jth reaction and Ea_j is the activation energy of the jth reaction.

4.3 Computation of Pressure and Temperature

In order to solve the Euler equations, another equation must be defined to have as many equations as unknowns which is typically given by the equation of state

$$\mathrm{p} = \sum_{i=1}^{S} \mathrm{p}_i = \rho \mathrm{T} \sum_{i=1}^{S} \mathrm{Y}_i R_i = \rho R_{mix} \mathrm{T}, \qquad i = 1, ..., S \tag{4.7}$$

where Y_i is the molar fraction of the ith species and R_i is the gas constant of the ith species defined by

$$R_i = \frac{\mathcal{R}}{m_i}, \tag{4.8}$$

where $\mathcal{R}$ is the universal gas constant and m_i is the molar mass of the ith species. Solving the energy equation given by Eqn. (4.4) for p yields

$$\mathrm{p} = \rho \sum_{i=1}^{S} \mathrm{Y}_i \mathrm{h_i}(\mathrm{T}) - \rho e + \frac{1}{2} \rho \sum u_k^2 \tag{4.9}$$

Now we have two equations, Eqn. (4.7) and (4.9), for pressure that are functions of T and the conserved variables. Combining these two equations yields

$$G(\mathbf{q},\mathrm{T}) = \rho \sum_{i=1}^{S} \mathrm{Y}_i \mathrm{h_i}(\mathrm{T}) - \rho e + \frac{1}{2}\rho \sum u_k^2 - \rho \mathrm{T} \sum_{i=1}^{S} \mathrm{Y}_i R_i = 0 \tag{4.10}$$

which must be implicitly solved for T using a Newton iteration. Once Eqn. (4.10) has been satisfied with the appropriate temperature, pressure is computed using the equation of state, Eqn. (4.7).

4.4 Boundary Conditions

Boundary conditions will govern the solution based on their proper implementation and where they are placed. The simulations used in the work documented in this thesis take advantage of four different types of boundary conditions: symmetry plane, adiabatic slip-walls, inflow, and outflow.

Symmetry Plane or Adiabatic Slip-Walls

To bound the simulation in a virtual duct, slip-walls must be enforced on the top and bottom boundaries. Slip-walls are chosen to satisfy the inviscid nature of the reactive Euler equations and are identical to a symmetry plane which forces the normal velocity component to zero by the following

$$\mathbf{u} \cdot \mathbf{n} = 0 \tag{4.11}$$

All other flow quantities are taken from the corresponding interior cells, shown in Fig. 4.1, which effectively represents an adiabatic wall because heat fluxes are suppressed at the wall.

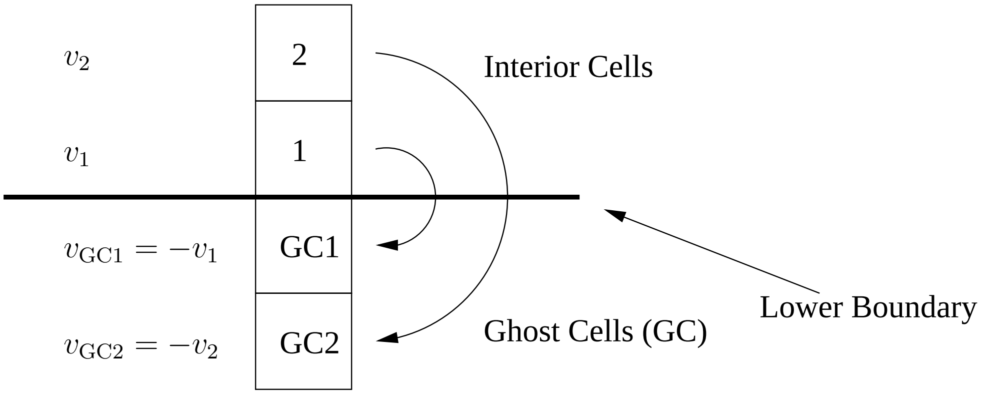

Figure 4.1: Schematic of the implementation of the slip-wall boundary condition.

Inflow and Outflow

The flow in a duct requires inflow and outflow conditions if both ends of the duct are open or either an inflow or outflow condition if only one end is open. To satisfy this we simply enforce the common Dirichlet boundary condition for inflow

$$\mathbf{q} = \mathbf{q}_{\text{inflow}} \tag{4.12}$$

where $\mathbf{q}_{\text{inflow}}$ is a fixed inflow condition, and the von Neumann boundary condition for outflow Hirsch (2007).

$$\frac{\partial \mathbf{q}}{\partial \mathbf{n}} = \mathbf{0} \tag{4.13}$$

It must be noted that the non-isentropic nature of the reacting flows requires special attention when applying boundary conditions which is challenging to implement. This requires dealing with the propagation of the characteristic waves in a non-isentropic flow and properly defining these waves at the boundary. By simplifying these boundary conditions, we may be introducing extra errors which should be fixed in the future with further advancements in CFD boundary conditions.

4.5 WENO/TCD Method

Detonations will naturally produce propagating waves as seen in Fig. 2.1 which must be accurately solved while conserving the discontinuity. For this reason, we turn to the AMROC computational framework that implements the AMR method developed by (Berger & Colella, 1989). The use of AMR allows the efficient refinement of the mesh near discontinuities such as the detonation front. A time-operator splitting approach is incorporated in AMROC to decouple the hydrodynamic transport and chemical reactions using a hybrid approach with low numerical dissipation developed by (Hill & Pullin, 2004). In smooth-flow regions, a collocated tuned centered finite differences (TCD) scheme is enforced and in regions near discontinuities and ghost-fluid boundaries, a tuned weighted essentially non-oscillatory (WENO) is enforced. A flagging method must be implemented in order to switch the methods in different regions of the flow. We will now briefly introduce the hybrid tuned WENO theory and refer to (Hill & Pullin, 2004) for a detailed discussion of the WENO-TCD approach.

The original WENO method is a flux based method that uses a convex, interpolated reconstruction of k candidate stencils over a range of $2k$ - 1 cells for the k-th order scheme. By convex, we mean the weight coefficients, ω_r, are all positive and sum up to one. WENO's stencils are oriented in an upwind biased configuration to favor the characteristic directions; however, the tuned WENO's stencils are centered around the point the flux is evaluated at. This introduces an extra stencil and increases the tuned WENO to the $(2k)$-th order of accuracy. The reconstructed flux of the tuned WENO method, $\hat{F}$, is written as

$$\mathrm{F}_{i+1/2} = \sum_{r=0}^{k} \omega_r a_{r,k} \mathrm{F}_{i-r+k-2} \tag{4.14}$$

where F is the original flux and $a_{r,k}$ are predetermined candidate stencil coefficients. The weight coefficients are calculated by

$$\omega_r = \frac{\alpha_r}{\sum_r^k \alpha_r} \tag{4.15}$$

where α_r is defined by

$$\alpha_r = \frac{C_r}{(\epsilon + IS_r)^2} \tag{4.16}$$

and IS_r is the smoothness measure of stencil r which is defined by

$$IS_r = \sum_{m=1}^{2} \int_{x_{i-1/2}}^{x_{i+1/2}} (\triangle x)^{2m-1} \left(\frac{\partial^m \mathbf{q_r}}{\partial x^m} \right)^2 dx \tag{4.17}$$

and ϵ is a regularization parameter.

The WENO weights are selected such that they correlate to the TCD stencil. This ensures the oscillations are at a minimum when the methods switch.

4.5.1 WENO/TCD Switching Mechanism

The method to select grid cells where the advection fluxes are evaluated using WENO or TCD schemes is derived from Lombardini (2008). This approach aims at efficiently locating regions in the flow where sharp gradients exist by using a pair of criteria derived by the Rankine-Hugoniot conditions. WENO is used only where the Lax entropy condition for a shock wave is satisfied, and a non-linear mapping of the pressure gradient exceeds a predefined threshold. The latter criterion ensures that WENO is not activated around acoustic waves and weak discontinuities.

First we consider the one-dimensional Riemann problem at each cell wall. Using the Lax entropy condition, we are able to characterize the waves $u \pm a$ as a shock wave if

$$u_R \pm a_R < u_\star \pm a_\star < u_L \pm a_L \tag{4.18}$$

where $a_{L,R} = \sqrt{\gamma_{L,R} p_{L,R} / \rho_{L,R}}$ are calculated using the properties at the left and right cell faces. The central state $(u_\star, a_\star)$ is calculated by the Roe's averages for the Euler equations (Leveque, 2002)

$$u_\star = \frac{\sqrt{\rho_L} u_L + \sqrt{\rho_R} u_R}{\sqrt{\rho_L + \rho_R}} \tag{4.19}$$

$$c_\star = \sqrt{(\gamma_\star - 1)\left(h_\star - \frac{1}{2} u_\star^2\right)} \tag{4.20}$$

where the enthalpy, $h_\star$, and specific heat ratio, $\gamma_\star$ are written as

$$h_\star = \frac{\sqrt{\rho_L} h_L + \sqrt{\rho_R} h_R}{\sqrt{\rho_L} + \sqrt{\rho_R}} \tag{4.21}$$

$$\gamma_\star = \frac{\mathrm{c}_{\mathrm{p}_\star}}{\mathrm{c}_{\mathrm{p}_\star} - r_{m_\star}} \tag{4.22}$$

$$\mathrm{c}_{\mathrm{p}_\star} = \frac{\sqrt{\rho_L} \mathrm{c}_{\mathrm{p,L}} + \sqrt{\rho_R} \mathrm{c}_{\mathrm{p,R}}}{\sqrt{\rho_L} + \sqrt{\rho_R}} \tag{4.23}$$

$$r_{m_\star} = \frac{\sqrt{\rho_L} r_{m,L} + \sqrt{\rho_R} r_{m,R}}{\sqrt{\rho_L} + \sqrt{\rho_R}} \tag{4.24}$$

Once again, $(h, \mathrm{c}_\mathrm{p}, r_m)_{L,R}$ are calculated at the left and right cell faces. To ensure that weak acoustic waves do not trigger the switching mechanism, a threshold is used, $\alpha_{\mathrm{Lax}}/a_\star$, when checking the inequality in Eqn. (4.18)

4.5.2 Validation of the WENO-TCD Method

The WENO-TCD method was validated by simulating a SOD Shocktube problem, without chemical reactions, because it is a widely used benchmark for a numerical algorithm's ability to solve discontinuities. We use three levels of AMR, each with a refinement factor of 2, with a base mesh of 128 x 128 over a 1 x 0.2 computational domain. The initial properties used for the SOD Shocktube are listed in Table 4.1 and the comparisons of the results with the analytical solution are shown in Fig. 4.2. The WENO-TCD method solves the shock with low dissipation at the shock and contact discontinuity where WENO is being applied which confirms the effectiveness of WENO-TCD and validates our numerical method.

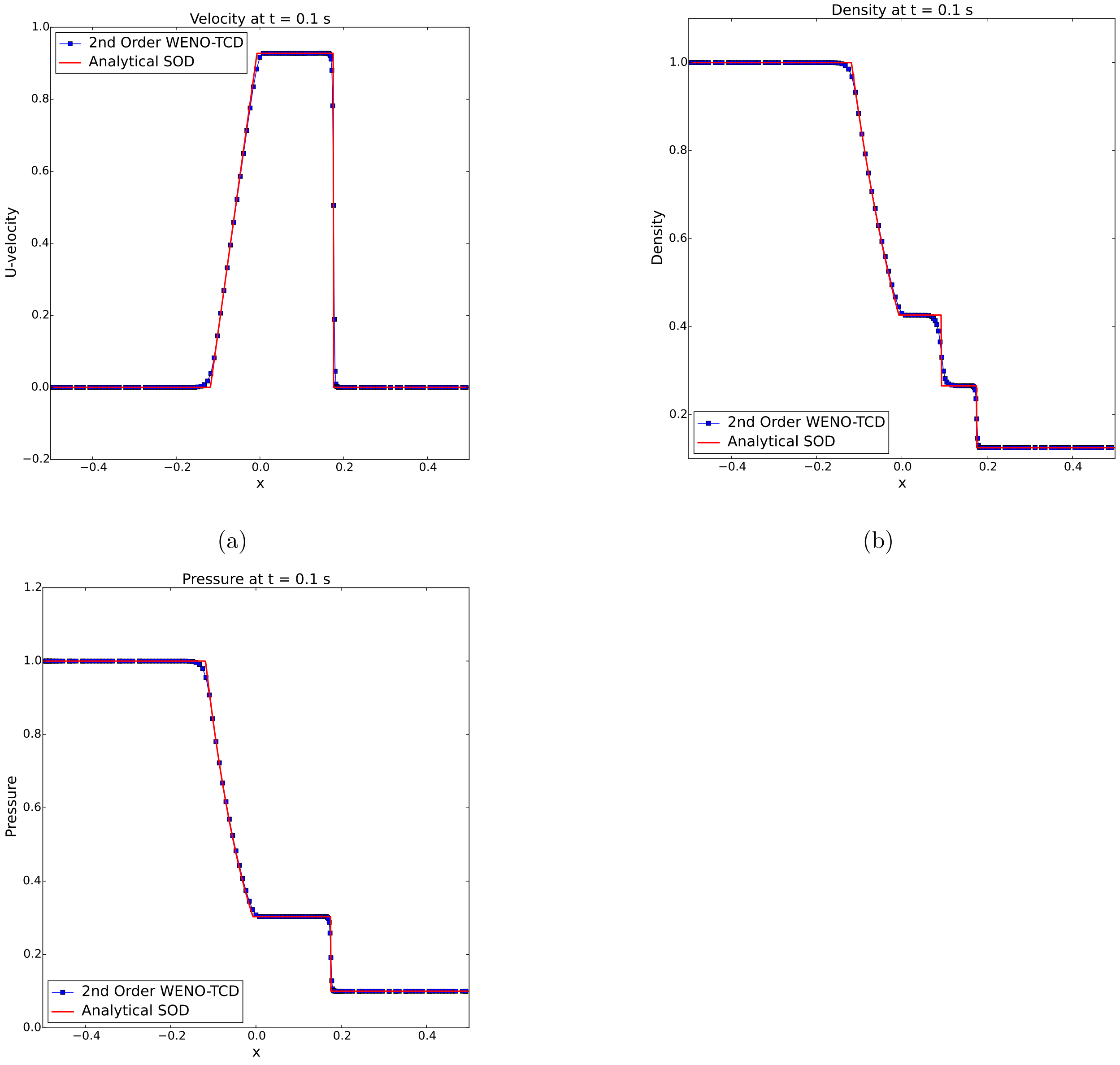

(a)

(b)

(c)

Figure 4.2: Results of SOD Shocktube simulation using a second order WENO-TCD method compared to the analytical solution for u-velocity (a), density (b), and pressure (c).

Table 4.1: Initial properties used to initiate the left and right side of the SOD Shocktube simulation.

	L	R
p	1	0.1
ρ	1	0.125
u	0	0

4.6 Chemistry Computations

The chemical kinetics, Eqn. (4.5), of the reacting Euler equations will be computed using the Chemkin package developed at Sandia Laboratories by Kerr *et al.* (1980). Chemkin is also able to calculate other gas mixture properties that are needed such as the formation enthalpies, γ, and c_p by linking it with the thermodynamic database from the NASA chemical equilibrium code. Each detonation simulation will require one specific chemical mechanism which Chemkin will use to calculate the production rates of each species. The chemical mechanism is chosen based on the reaction of interest and contains information of all the species and intermediate reactions.

Chapter 5

TWO-DIMENSIONAL DETONATIONS

The results from the simulations of detonations in a duct with both ends open, Sec. 5.1, and with one open and closed end, Sec. 5.2, will be analyzed in this chapter. First the detonation cells in a duct with both ends open is compared with previous simulations of other researchers using the same gaseous mixture and initial conditions. The results are then used to verify the shock wave cross-current dynamic theory. The next section will discuss the results from detonations in a duct with one end opened and one closed. The results are used to prove the validity of the one-dimensional detonation structure to the two-dimensional detonation.

5.1 Two-Dimensional Detonations in an Open Ended Duct

5.1.1 Computational Setup

The computational setup follows the work of Deiterding and Oran to validate our code. The simulation is started with the initial conditions shown in Table 5.1. This simulation was created with an initial 100 cm x 3 cm computational domain over 2010 x 60 cell mesh. The one-dimensional ZND solution, created from the Boris and Oran with third-body enhancements made by Peters and Rogg chemical mechanism (Boris, Oran, Peters & Rogg, 1982), was used to initiate the left region of the shock, located at x = 8.6 cm, while the region to the right of the shock was the initial conditions. A 1 x 0.7 cm pocket of unreacted gas was also placed at the bottom boundary with its center 0.8 cm to the left of the shock. This effectively represented the upper half of the simulation domain that Oran used or the full height of the computational domain that Deiterding used.

Three levels of AMR, refinement factor of 2, were used with the tolerances tabulated in

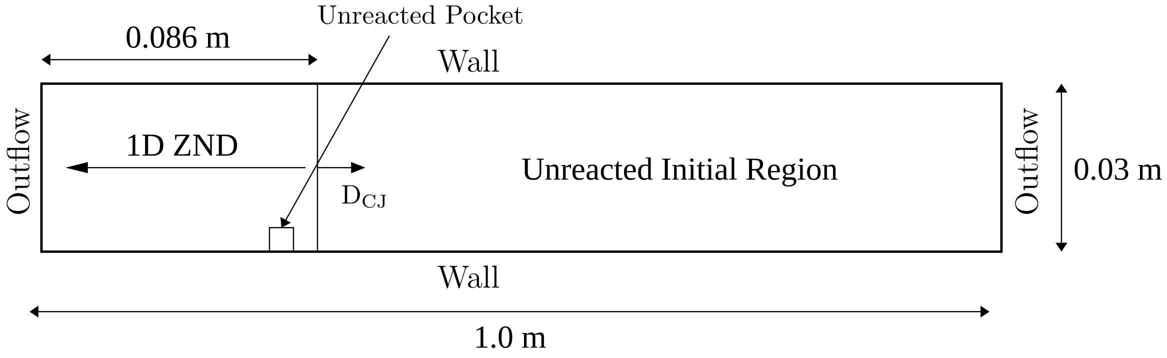

Figure 5.1: The computational setup of detonations in a duct with two open ends.

X_{H_2}	0.2	T_0 (K^o)	298
X_{O_2}	0.1	ρ_0 (kg / m^3)	0.084
X_{AR}	0.7	u_0 & v_0 (m/s)	0
P_0 (Pa)	6670		

Table 5.1: Initial conditions for simulation 1.

Table 5.2. The WENO-TCD hybrid scheme was selected for the spatial discretization, using $\alpha_{\text{Lax}} = 0.1E-2$, with a 3rd order SSP Runge-Kutta method for time discretization.

5.1.2 Chemical Mechanism

The Boris and Oran, H_2-O_2-AR, mechanism with third-body enhancements made by Peters and Rogg was used for this simulation (Boris *et al.*, 1982). The one-dimensional ZND solution was produced by a code developed by Shepard (2000) which is linked with Chemkin and the specified chemical mechanism, located in Appendix A.2. The code creates the solution by integrating the conservation equations along a Rayleigh line. The initial H_2-O_2-AR ratios of $2 : 1 : 7$, respectively, the initial conditions from Table. 5.1, and the expected $D_{CJ} = 1627$ m/s were used to create the solution as shown in Fig. 5.2 and 5.3. Throughout this detonation, 47 reactions take place amongst nine species including: H_2, H, O_2, O, H_2O, OH, HO_2, H_2O_2,

ρ	$0.1 \frac{kg}{m^3}$	H	$2.00 * 10^{-5}$
T	500 K	O_2	10^{-3}
P	$1.5 * 10^4$ Pa	O	10^{-4}
H_2	$1.2 * 10^{-4}$	H_2O	$8.5 * 10^{-4}$
OH	$1.3 * 10^{-4}$		

Table 5.2: AMR tolerances

and AR.

5.1.3 Multidimensional Detonation Front

The detonation front structure was reproduced from the simulation results at t = 240 μs, Fig. 5.4. There exists two triple points that are almost perfectly symmetric about the center of the computational domain height. The density schlieren contour highlights the differences in the inductance zone lengths behind the incident shock and Mach stem by the white zone behind the detonation front. The shear line should divide the two regions with different inductance lengths; however, this is difficult to distinguish because of the jump in density across the transverse wave.

Looking to the pressure contour of the detonation front, we note that the pressure jump is larger behind the Mach stem than the incident shock. The length of the induction zone is dependent on this pressure jump because the sudden increase in pressure the chemical reactants experience through the detonation front breaks them up into their reactive components through the induction zone. A larger pressure jump breaks the chemical reactants up faster which results in a shorter induction zone length, as observed behind the Mach stem.

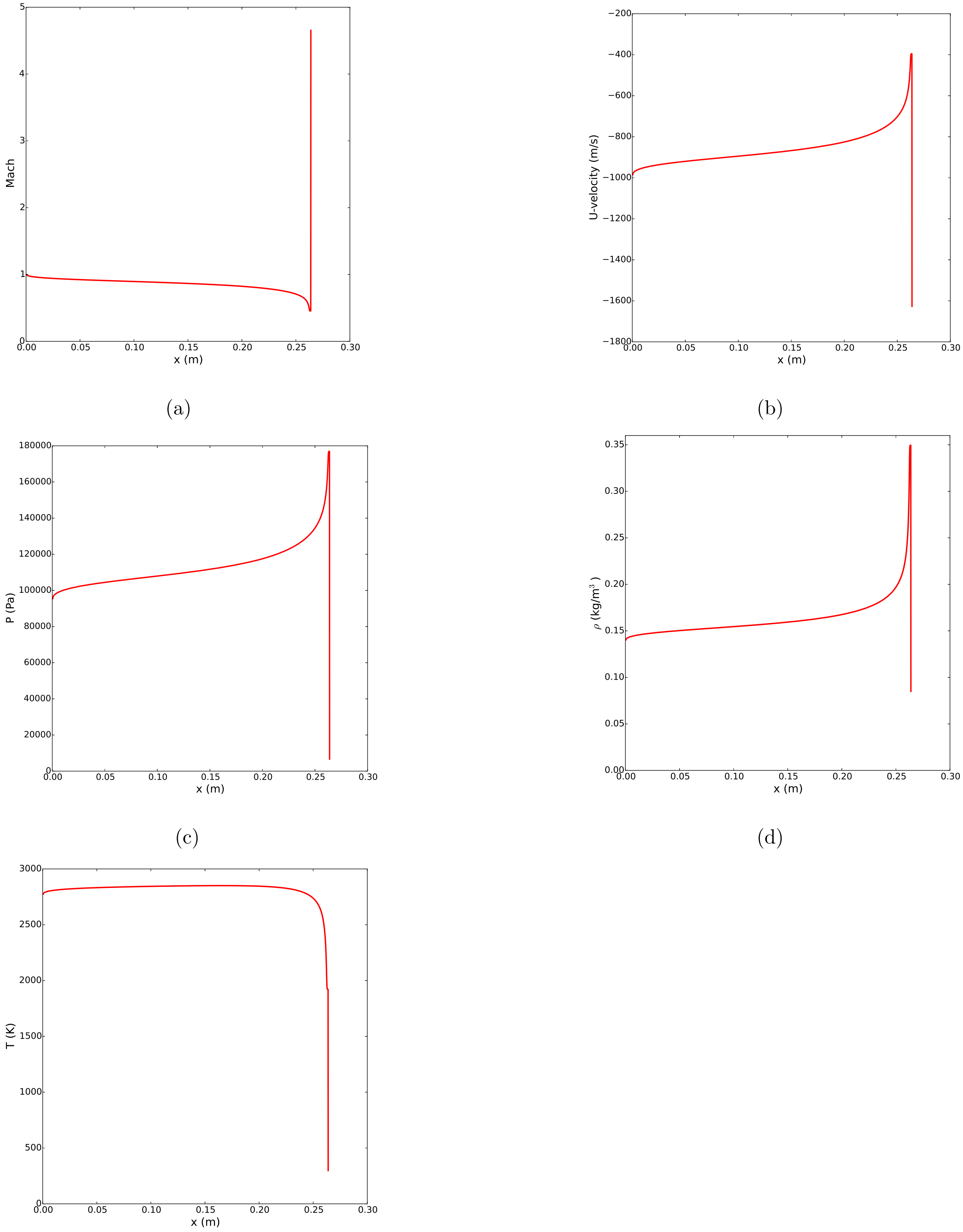

(a)

(b)

(c)

(d)

(e)

Figure 5.2: The one-dimensional ZND solution created from Shepard (2000) for (a) Mach, (b) u-velocity, (c) pressure, (d) density, and temperature (e) in the reference frame attached to the detonation front using the chemical mechanism by Boris *et al.* (1982).

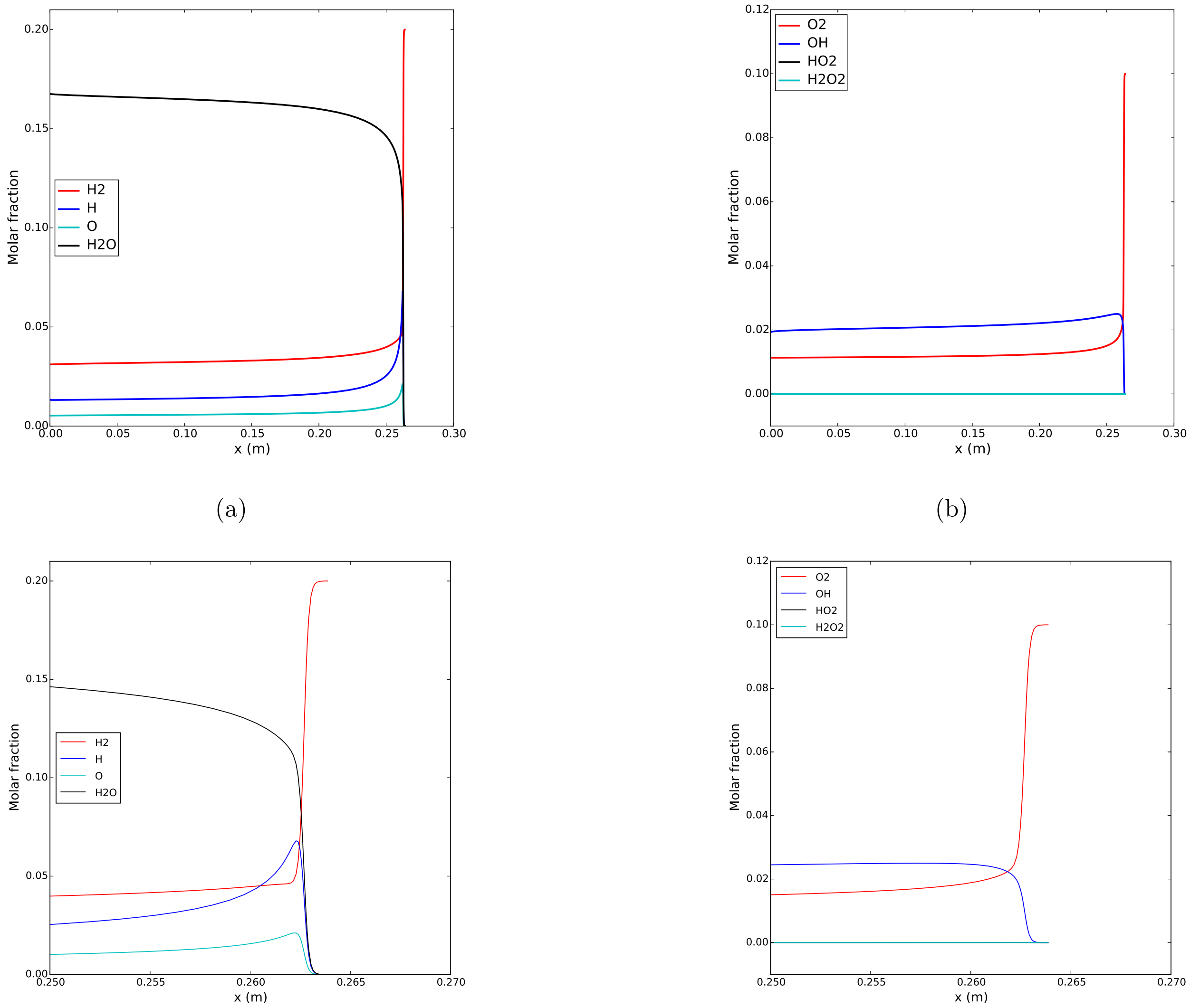

(a)

(b)

(c)

(d)

Figure 5.3: The one-dimensional ZND solution created from Shepard (2000) for the species over the entire ZND region (a,b) and a magnified view at the detonation front (c,d) using the chemical mechanism by Boris *et al.* (1982).

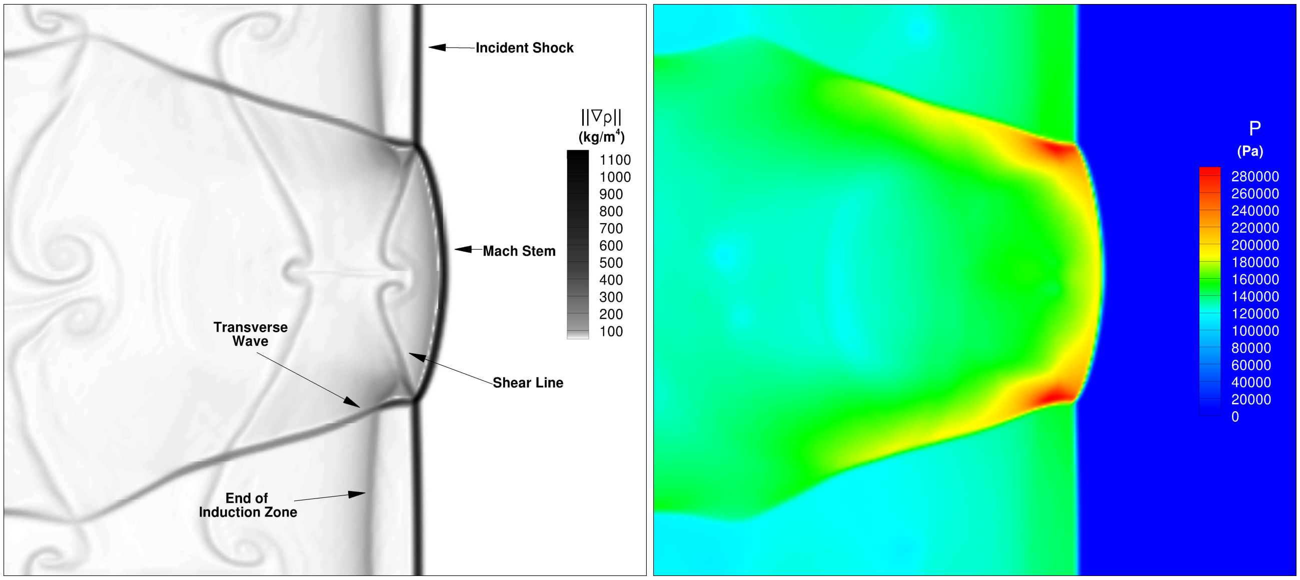

(a) (b)

Figure 5.4: a). Density schlieren contour and b). pressure contour of the detonation front at t = 240 μs.

5.1.4 *Regular Detonation Cells*

The detonation cell results of the two-dimensional detonation in an open ended duct are shown below in Fig. 5.5. There is a slight asymmetry in the detonation cell; however, the cell dimensions match Deiterding's and Oran's work. The regular detonation cell length is 5.25 cm and height 3 cm.

The triple point tracks clearly outline the detonation cell as they move away from each other and collide again approximately 32 μs later. By observation of Fig. 5.5, the driving force of the triple point movement is the pressure. The pressure jump across the Mach stem is greater than across the incident shock so the triple points naturally move towards the lower pressure region, or away from each other in the first half of the detonation cell. As the second half of the detonation cell begins to form at t = 248 μs, the Mach stem and incident shock switch positions. Now the pressure drives the triple points towards each other, because the incident shock is in the center, until they finally collide at t = 264 μs and the creation of the following detonation cell begins.

5.1.5 Cross-Current Dynamics Validation

The simulation results are now used to validate the cross-current dynamics theory that was developed in Chapter 3 at t = 232 μs, 240 μs, and 248 μs. The detonation front was constructed by locating the maximum in the pressure gradient in the longitudinal direction. The pressure jump was then used to calculate the normal Mach by using the shock relation given by

$$\frac{\mathrm{p_2}}{\mathrm{p_1}} = \frac{2\gamma \mathrm{M_n}^2 - (\gamma - 1)}{\gamma + 1} \tag{5.1}$$

where γ was chosen to be γ ahead of the shock to simplify the problem and because the sensitivity of the γ jump to M_n is relatively low. Using the defined curvature of the detonation front, the normal Mach was broken up into its x and y-components along the detonation front and finally used to define D_x and D_y with Eqn. (2.30) and the speed of sound ahead of the detonation front calculated by

$$a_0 = \sqrt{\frac{\gamma \mathrm{p_0}}{\rho_0}} \tag{5.2}$$

The resulting cross-current dynamics calculated by Eqn. (3.11) and (3.12) are plotted with the u and v-velocities extracted directly behind the detonation front in Fig. 5.6 and 5.7. A curve-fit was applied to the extracted detonation front geometry and pressure behind the detonation front as well as the extracted u-velocity to avoid large oscillations. The cross-current dynamic comparisons were chosen to correlate to Fig. 5.5 when the triple points have collided (t = 232 μs), when the triple points are half way from the walls and centerline (t = 240 μs), and when the triple points are located near the walls (t = 248 μs).

The comparison of the u-velocity along the detonation front illustrates the difficulty of the cross-current dynamic solution to predict the u-velocity due to a combination of post-processing issues and the assumptions made in the cross-current dynamics theory. The

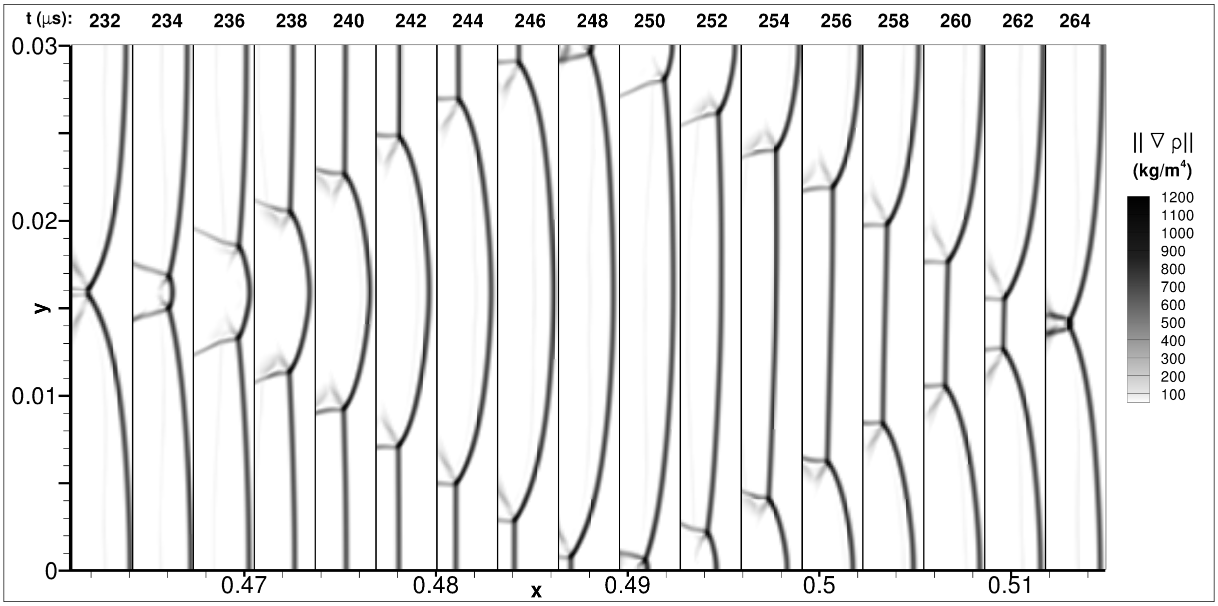

(a)

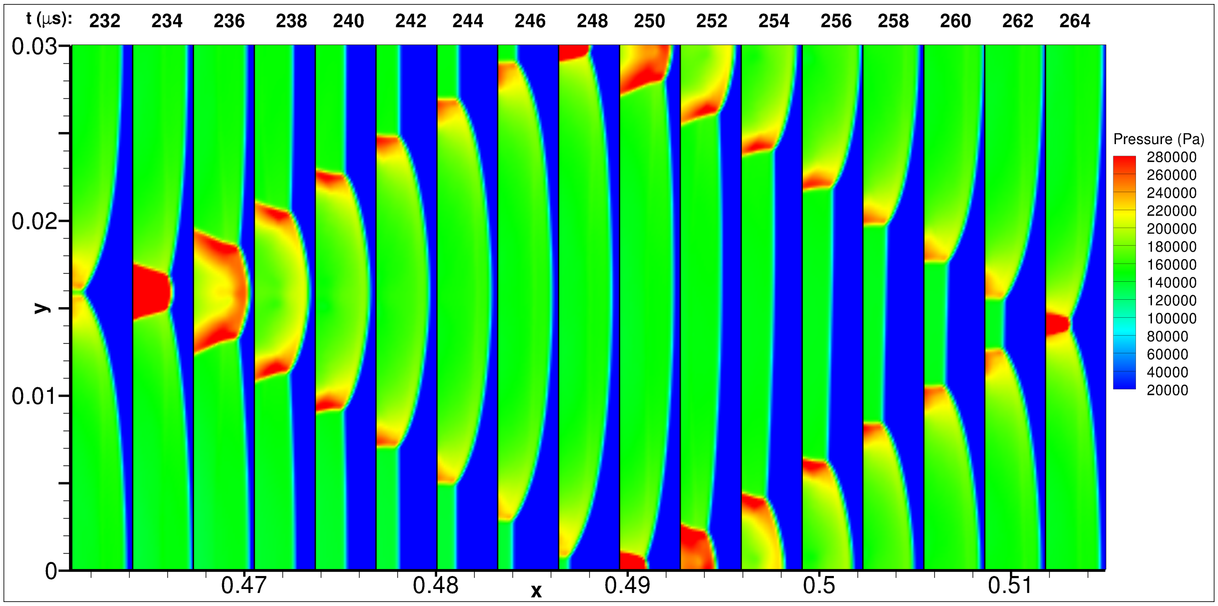

(b)

Figure 5.5: a). Density schlieren contour and b). pressure contour of one detonation cell using the initial conditions in Table 5.1 in an open ended duct. Dimensions of the cell are 3 cm x 5.25 cm.

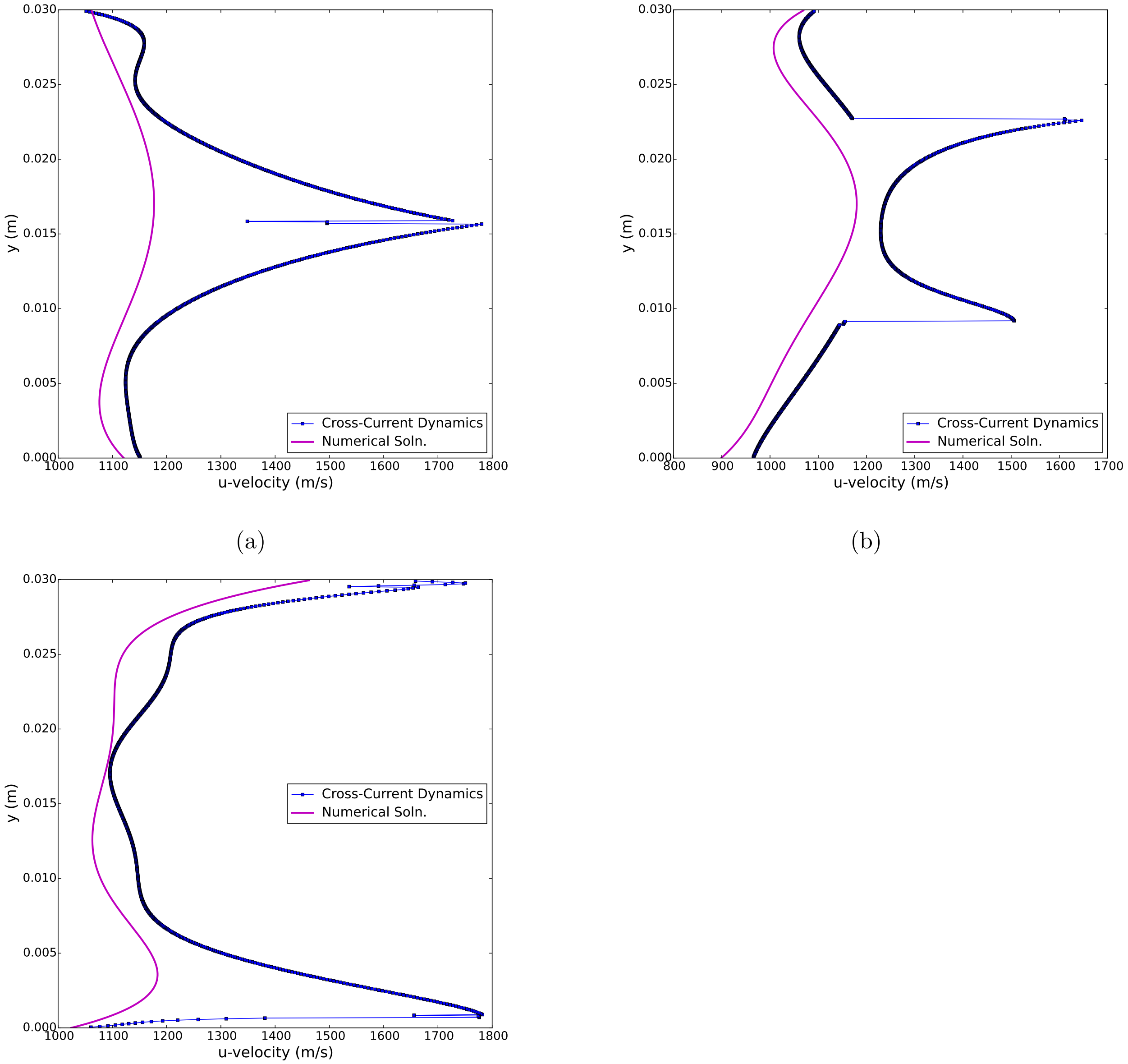

(a)

(b)

(c)

Figure 5.6: Cross-current u-velocity plotted with the numerical solution v-velocity at t = 232 μs (a), 240 μs (b), and 248 μs (c).

cross-current u-velocity, Eqn. (3.11), depends mainly on the structure of the pressure jump along the detonation front and secondarily on the shape of the detonation front. We believe the source of the large disagreement lies in the post-processing of the pressure jump from the adiabatic detonation front, especially near the triple points and along the Mach stem. As seen in Fig. 5.6, the peak in the disagreements are located at the triple points because the pressure jump in this region is the result of the both the pressure jump from the Mach stem and transverse wave, which is not accounted for in the theory. Also, the induction zone behind the Mach stem is extremely small, and shrinks near the triple points, which creates complications when trying to accurately extract the pressure from the induction zone. The pressure, u-velocity, and v-velocity contours, with a line indicating the end of the induction zone, at the times the cross-current comparison were performed are shown in Appendix A.3. These contour plots illustrates the sharp gradient in pressure near the triple points and Mach stem which explains why our results tend to have large disagreements in the Mach stem region and especially at the triple points. The best agreement among these comparisons is along the incident shock at t = 240 μs from the lower, 0.0 to 0.09 m, and upper, 0.23 to 0.03 m, region of the duct and at t = 248 μs in the center region from y = 0.05 to 0.026 m. The majority of the detonation front in t = 232 μs is a Mach stem with the triple points colliding in the middle which explain the large disagreement.

The cross-current calculated v-velocity shows much better agreement than the u-velocity, but once again we note that the max error occurs at the triple points. The detonation front curvature now has a larger influence on the v-velocity structure as seen in Eqn. (3.12) which we believe alleviates the sensitivity of the solution to the pressure jump. We are able to capture the detonation front quite accurately along the Mach stem and incident shock, but struggled at the triple points where kinks occurred in the curvature. This led to better agreement between the extracted v-velocity and cross-current calculated velocity except at the triple points where we struggled to determine the correct adiabatic pressure jump and an accurate representation of the detonation front curvature.

In order to avoid the issues with the pressure jump across the detonation front, we now

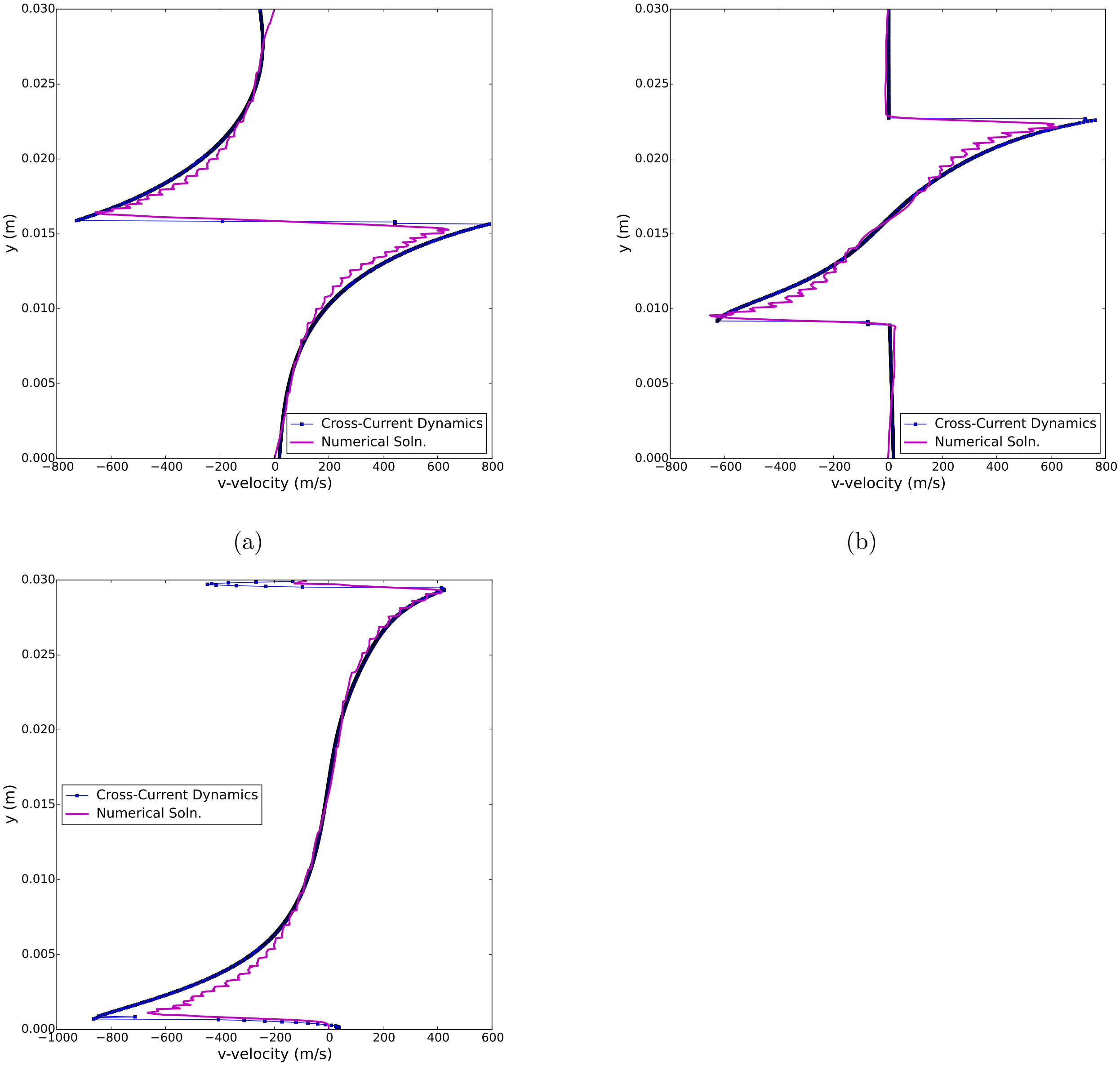

(a)

(b)

(c)

Figure 5.7: Cross-current v-velocity plotted with the numerical solution v-velocity at t = 232 μs (a), 240 μs (b), and 248 μs (c).

compare the ratio of the v-velocity to u-velocity with the ratio from the simulation data. By dividing the two cross-current equations, (3.11) and (3.12), we arrive at the following

$$\frac{v_1}{u_1} = -\frac{\partial f_s}{\partial y} \tag{5.3}$$

In this form, the ratio only relies on the curvature of the detonation front and the results are shown in Fig. 5.8 and 5.9 along with the detonation front curvature for the corresponding times. As expected, the cross-current theory compares almost perfectly with the simulation data and the ratio is the inverse of the detonation front curvature. Differences between the two velocity ratio's are a consequence of how well the detonation front was captured which was difficult at the triple points due to the kink and the curve-fitting we applied to smoothen out the data.

5.1.6 Cross-Current Dynamics Downstream of Detonation Front

Away from the detonation front, the cross-current dynamics no longer applies. The flow becomes dominantly one-dimensional further downstream as shown by the ratio of the of v-velocity to u-velocity in the reference frame attached to the detonation front, Fig. 5.10. This velocity ratio is greatest in magnitude directly behind the detonation front near the triple points. Through a qualitative observation, we note that the velocity ratio throughout the majority of the region downstream of the detonation front reduces to nearly 0. The downstream regions with larger velocity ratios are believed to be a result transverse motion produced by the transverse waves and the vorticity generated along the shear lines, Fig. 5.11 to 5.13. As the transverse wave changes orientation and position, the regions with greater v-velocity follow the transverse wave motion, due to the pressure jump across the transverse wave, and seem to be bounded by the shear lines, where vorticity exists.

An interesting pattern may also be observed in the vorticity contours by the alternating vorticity lines in Fig. 5.12. The vorticity is created by the triple points, thus these patterns are created by the movement of the triple points. These vorticity lines, or shear lines, are

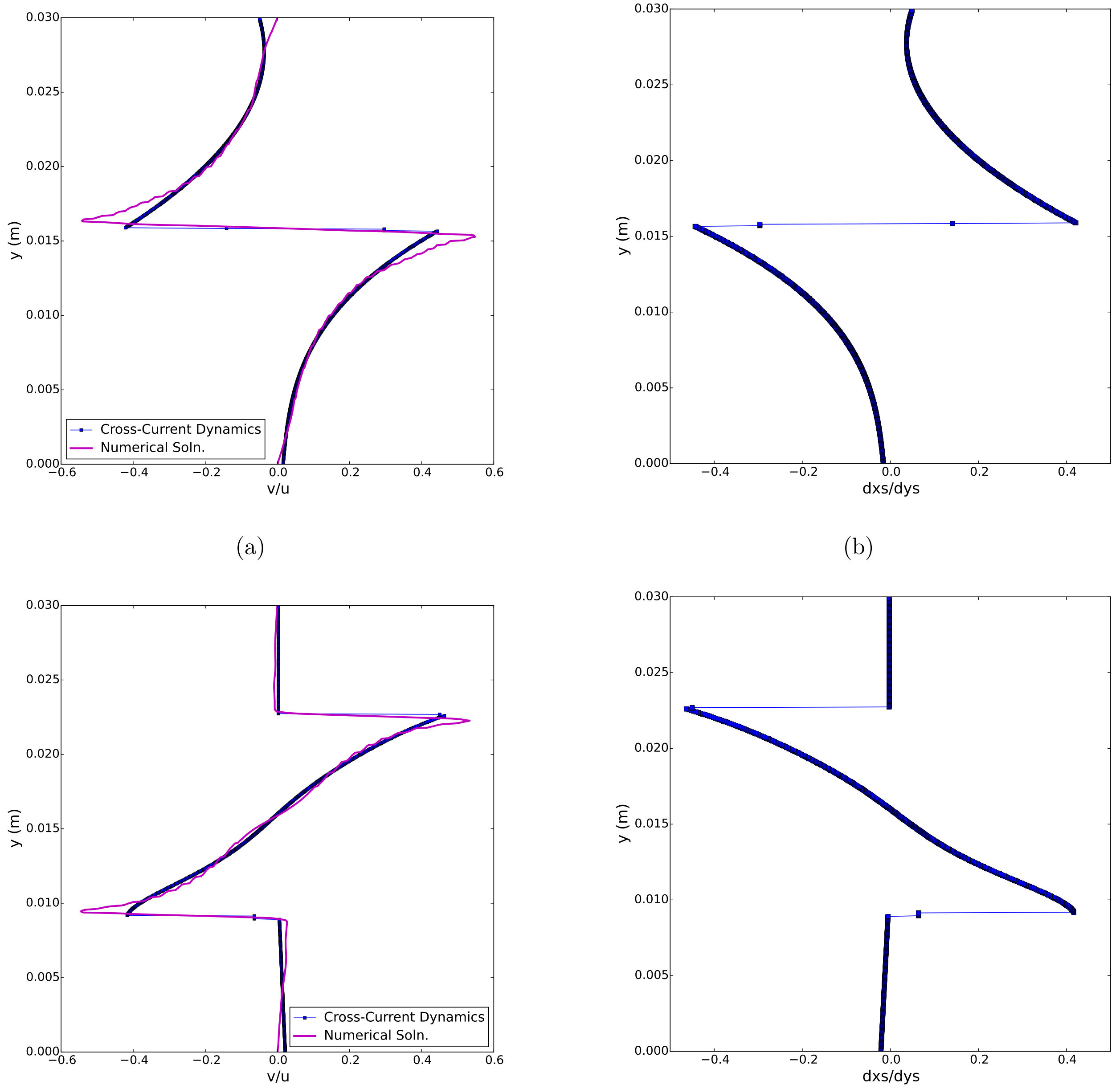

(a)

(b)

(c)

(d)

Figure 5.8: Cross-current ratio of v-velocity to u-velocity plotted with the numerical solution v-velocity as well as the slope curvature at t = 232 μs (a,b) and 240 μs (c,d).

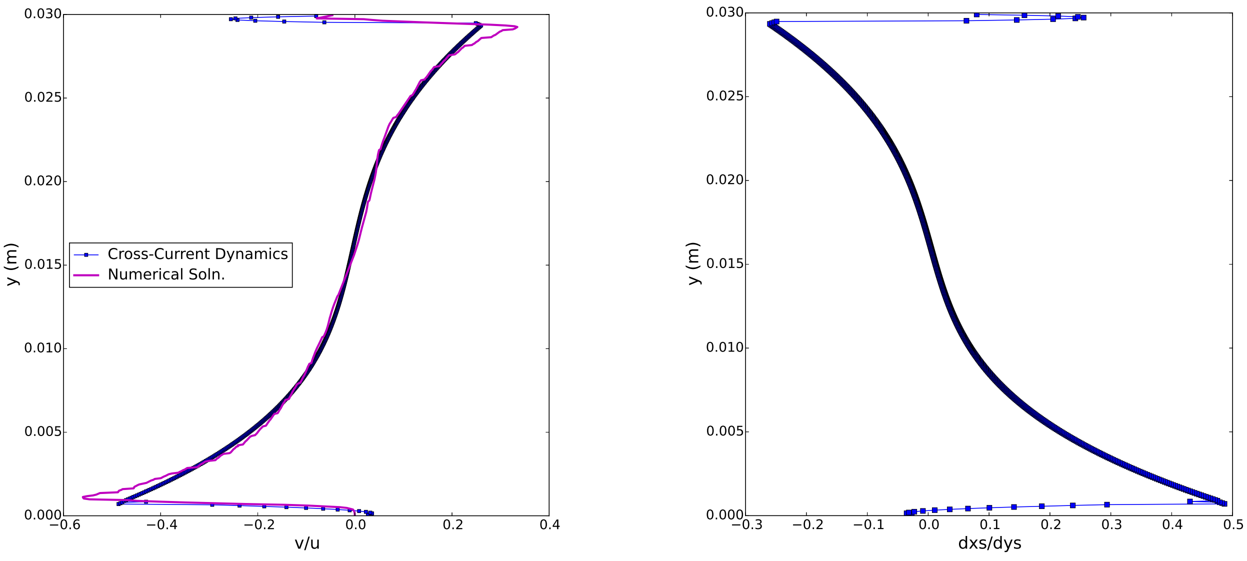

(a) (b)

Figure 5.9: Cross-current ratio of v-velocity to u-velocity plotted with the numerical solution v-velocity as well as the slope curvature at t = 248 μs.

shed from the triple points when the triple points collide with each other in the middle of the domain or with the upper and lower walls. The collision causes the triple points to move in the opposite directions which reverses the direction of the vorticity and thus separates the previously attached shear line.

5.2 Two-Dimensional Detonations In Open/Closed Ended Duct

5.2.1 Computational Setup and Initialization

The setup of this simulation was similar to the previous simulation in a duct with two open ends because it uses the same initial conditions as shown in Table 5.1. Instead of an outflow condition on the left boundary, an adiabatic wall boundary is enforced. The domain is extended to 1.5 m and the shock location is shifted to 28 cm, as shown in Fig. 5.14, with a 3030 x 50 cell mesh. The solution to the one-dimensional ZND simulation was then used to initiate the left side of the shock, located at x = 28 cm, while the right domain was

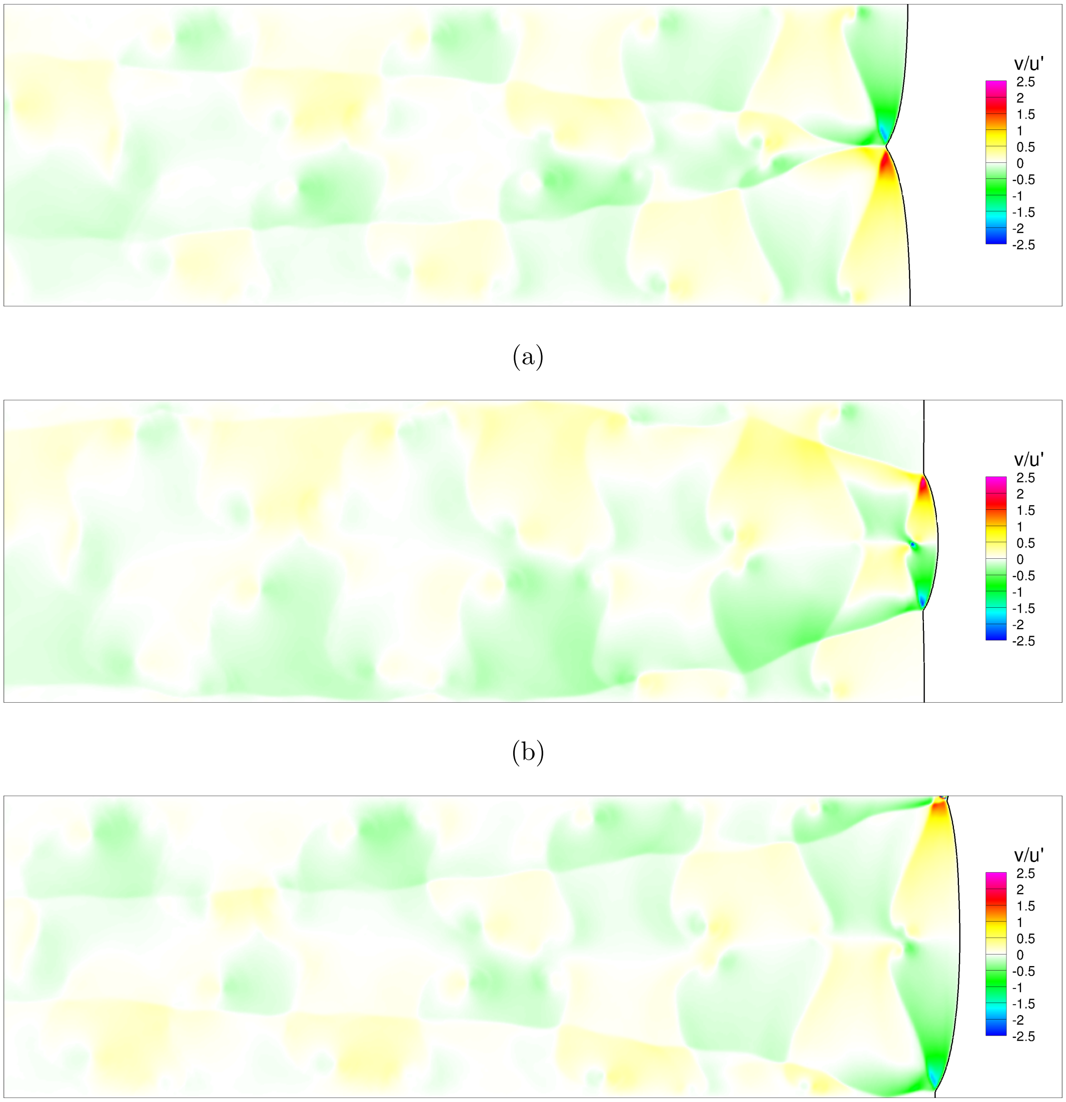

(a)

(b)

(c)

Figure 5.10: Contours of the v-velocity to u-velocity ratio, in the reference frame attached to the detonation front, at t = 232 μs (a), 240 μs (b), and 248 μs (c).

(a)

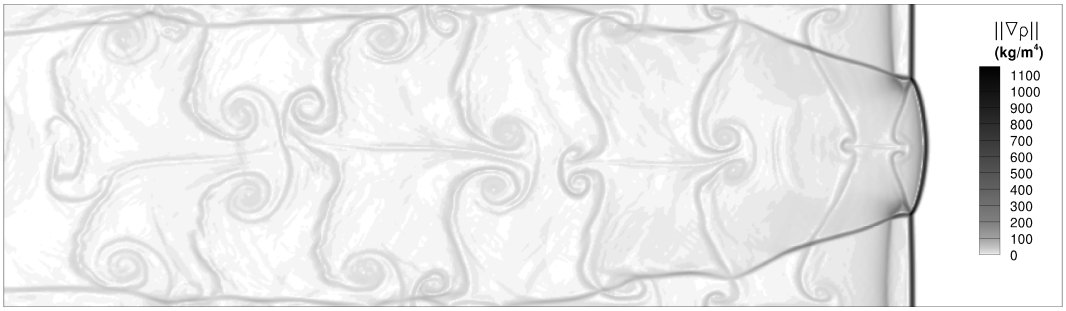

(b)

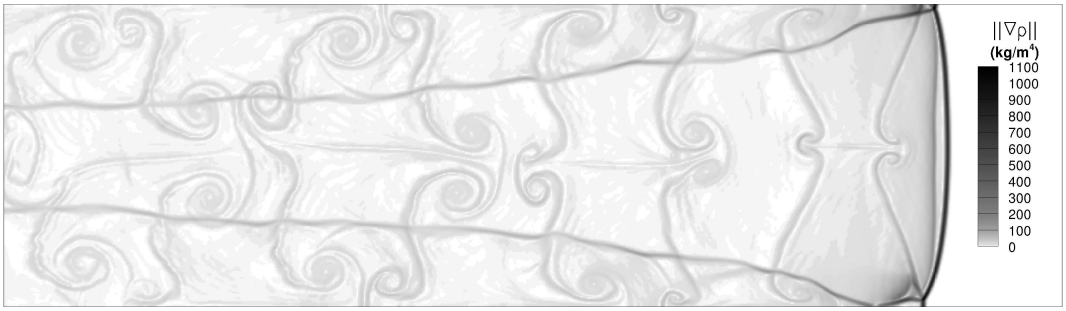

(c)

Figure 5.11: Contours of the density gradient magnitude at t = 232 μs (a), 240 μs (b), and 248 μs (c).

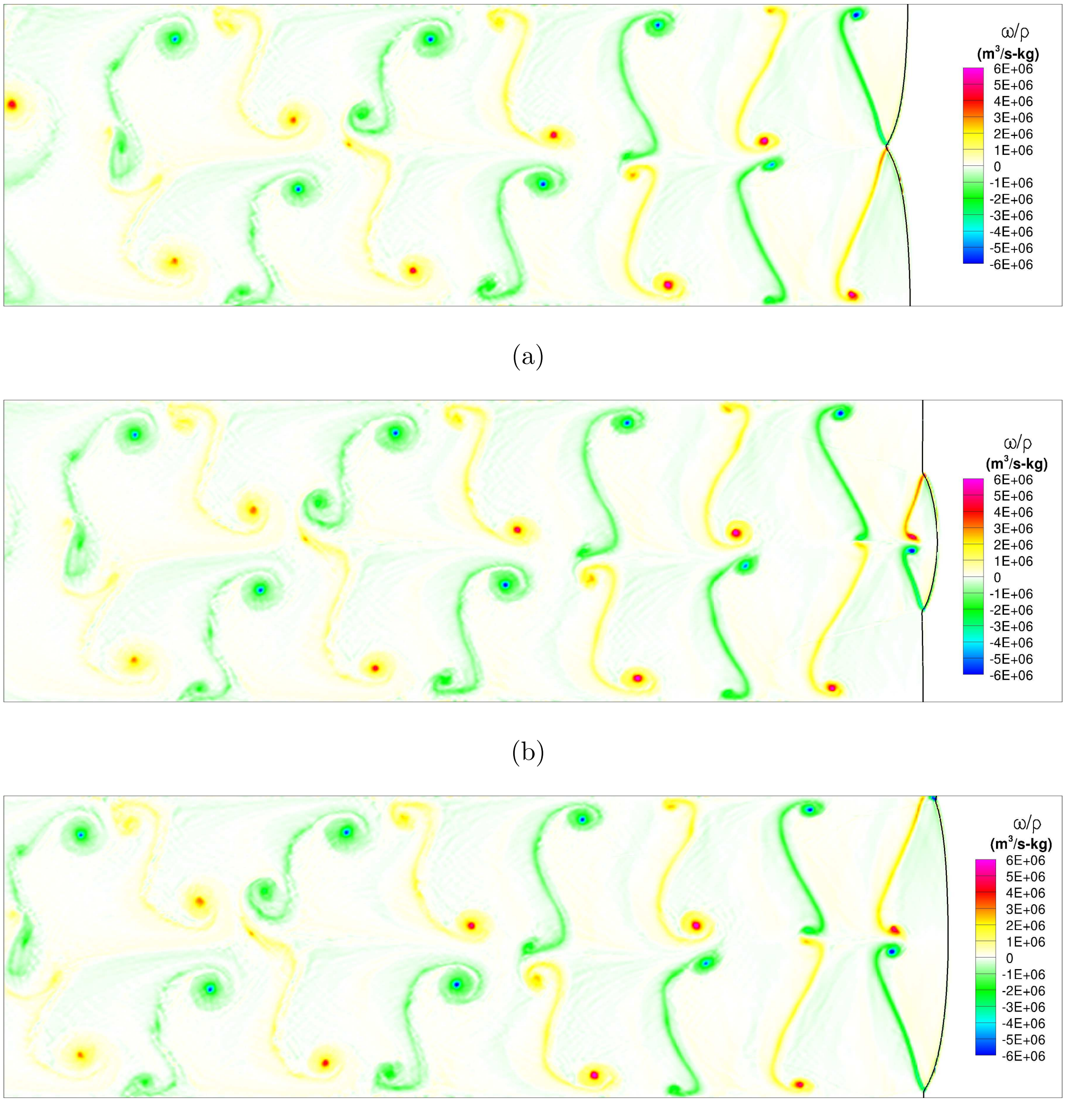

(a)

(b)

(c)

Figure 5.12: Contours of ω/ρ at t = 232 μs (a), 240 μs (b), and 248 μs (c).

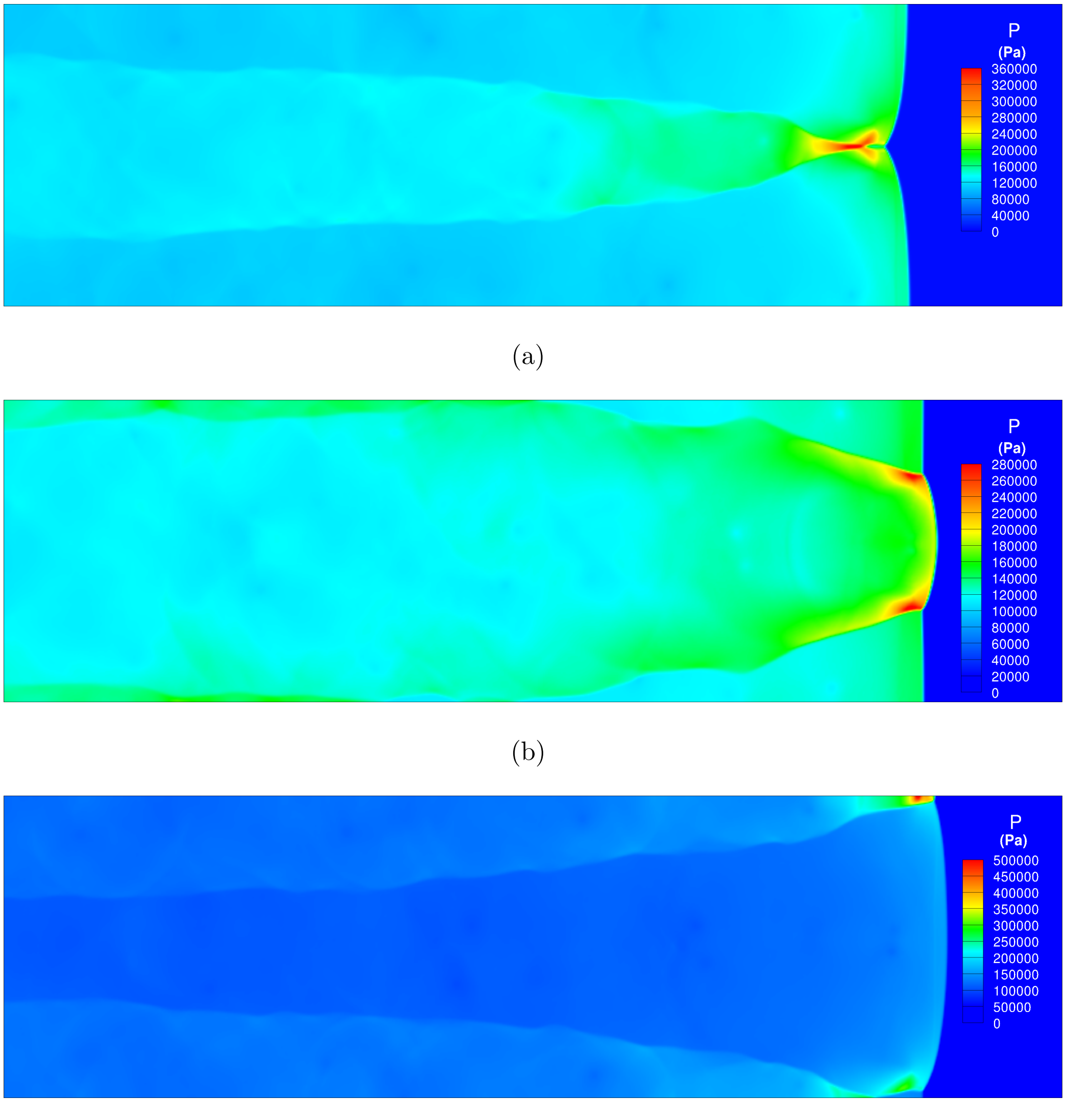

(a)

(b)

(c)

Figure 5.13: Contours of pressure at t = 232 μs (a), 240 μs (b), and 248 μs (c).

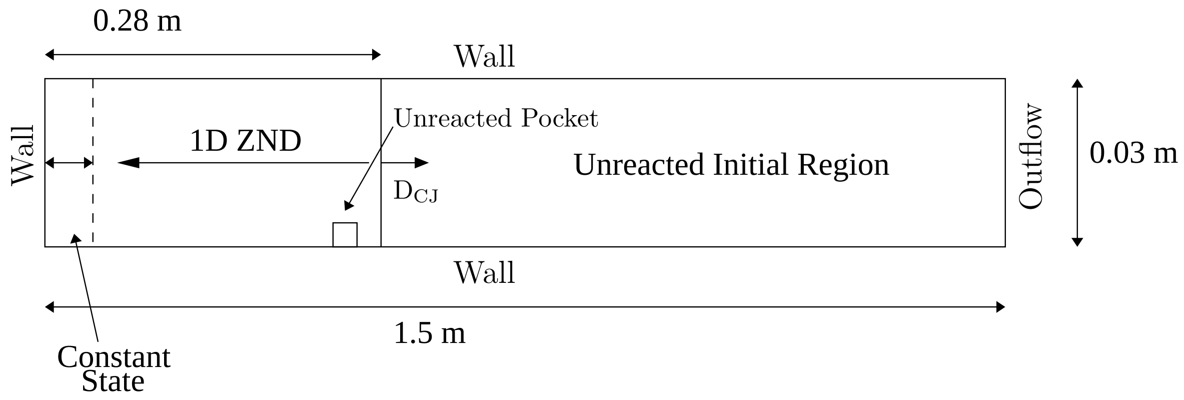

Figure 5.14: The computational setup of detonations in a duct with an open and closed end.

initiated with the unreacted H_2-O_2-AR ratios. Because the one-dimensional ZND solution has a length of approximately 26.316 cm, the flow properties at the end of the ZND solution are extrapolated to the left wall boundary, which we call the constant state region.

Three levels of AMR were used with all refinement factors set to 2 with the same AMR tolerances as the previous simulation, tabulated in Table 5.2. The WENO-TCD hybrid scheme was selected for the spatial discretization, using $\alpha_{\text{Lax}} = 0.1E - 2$, with a 3rd order SSP Runge-Kutta method for time discretization.

5.2.2 Regular Detonation Cells

The detonation cells are the same from the simulation in a duct with both ends open as we expected as shown in Fig. 5.15. Not suprisingly, the detonation front from both simulations shared the same characteristics.

5.2.3 Area-Averaged Properties Comparisons

An area-average was taken along y-slices from the detonation front to the left end of the domain using Eqn. 5.4 at each x location

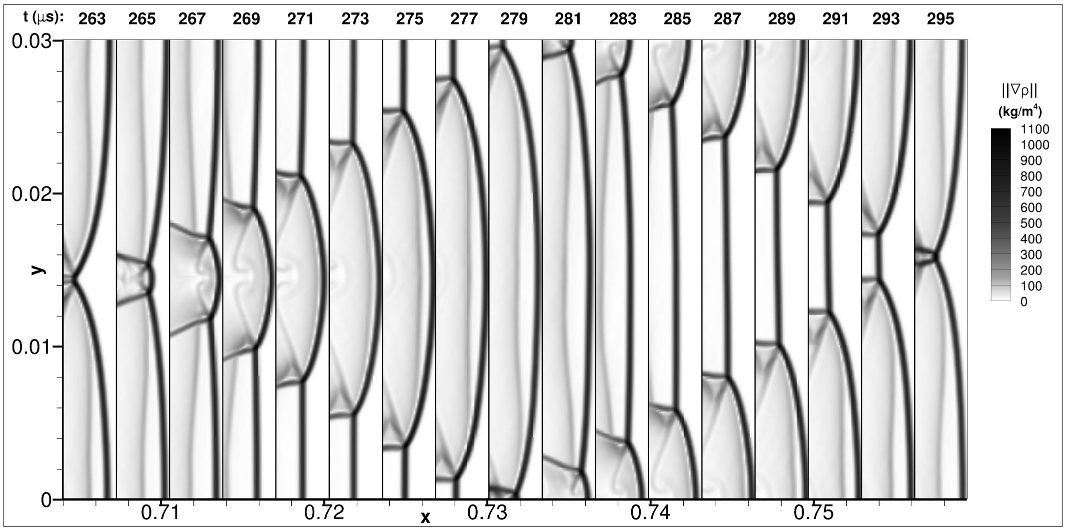

(a)

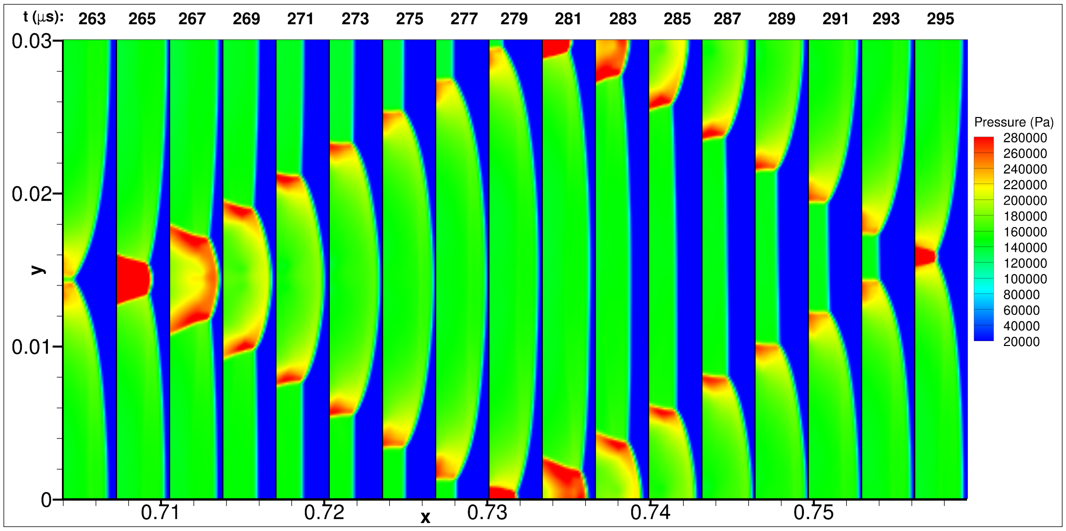

(b)

Figure 5.15: a). Density schlieren contour and b). pressure contour of one detonation cell using the initial conditions in Table 5.1 in a duct with a closed and open end. Dimensions of the cell are 3 cm x 5.25 cm.

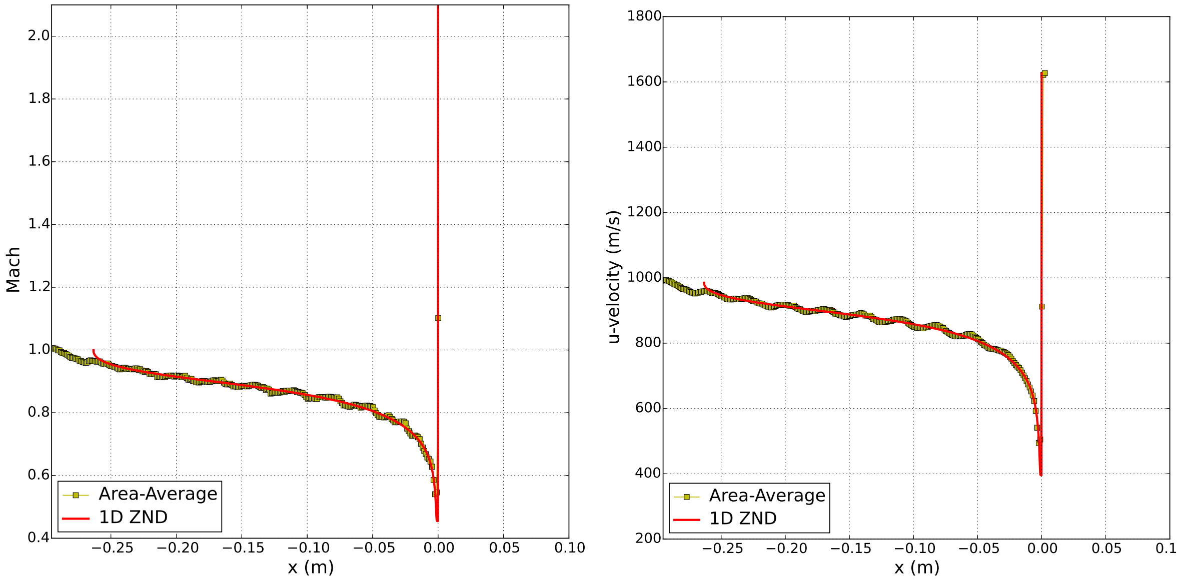

(a) (b)

Figure 5.16: Area-averaged Mach (a) and u-velocity (b) in the reference frame attached to the detonation front compared to the computed one-dimensional ZND solution at t = 555 μs.

$$\bar{B} = \frac{1}{N}\sum_{i}^{N} B_i \tag{5.4}$$

where B_i is the property at the ith cell along a y-slice and N is the total number of cells in the y-direction. The area-averaged results are then compared to the one-dimensional ZND solution that was used to initiate the two-dimensional simulation in a similar way to the work by Radulescu, Sharpe, Law & Lee (2007) as shown in Fig. 5.16 to 5.18 at t = 555 μs. We also compare the analytical post-CJ structure that was calculated as described in Sec. 2.2.3, using Eqn. (2.28) - (2.31), as shown in Fig. 5.20 and 5.21.

The comparisons of the area-averaged results with the one-dimensional ZND structure shows an almost exact agreement where the area-average slightly oscillates around the ZND solution. A close observation will reveal that the sonic plane of the fluid particles is achieved over a slightly longer distance for the area-averaged results compared to the one-dimensional

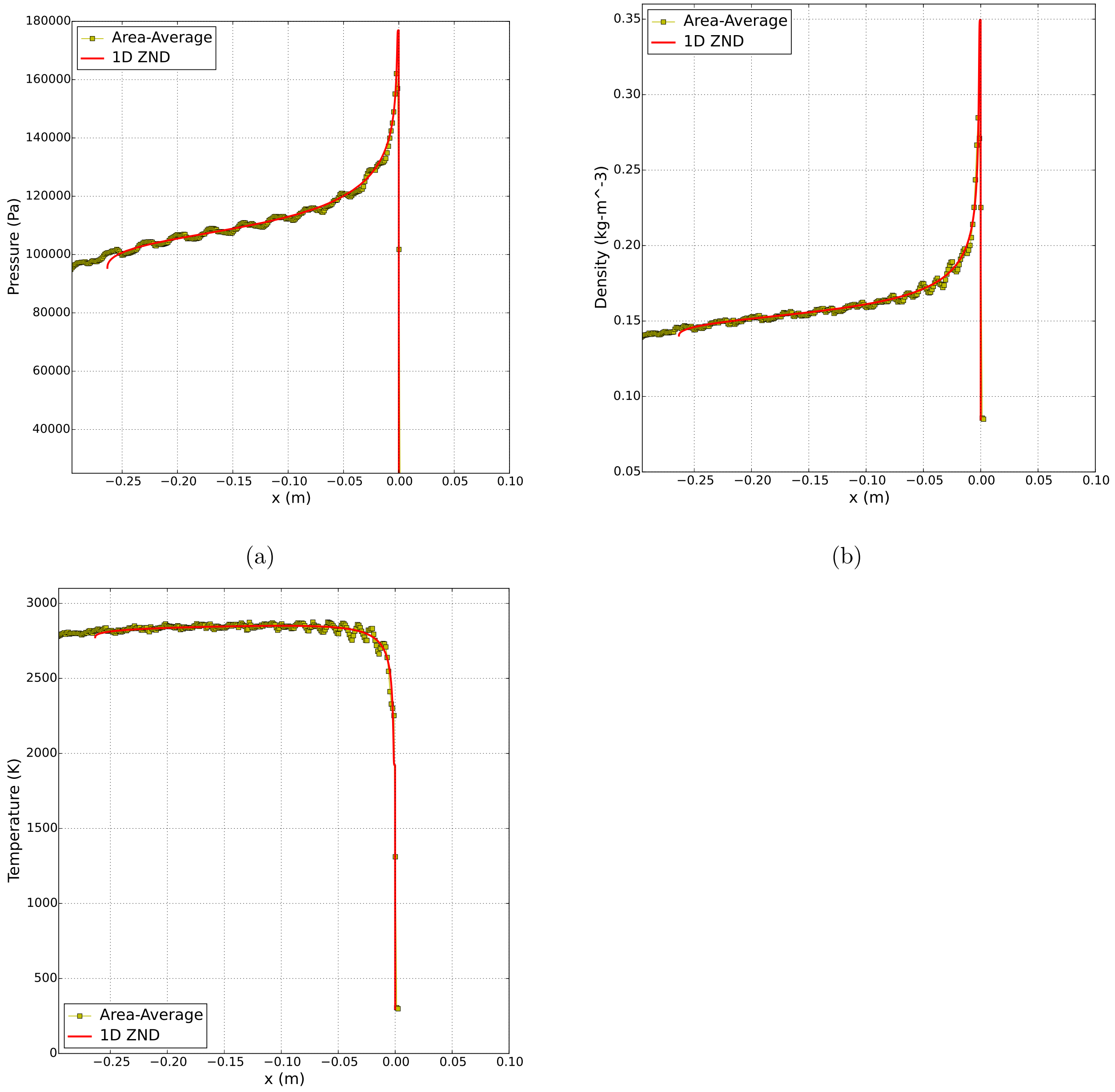

(a)

(b)

(c)

Figure 5.17: Area-averaged pressure (a), density (b), and temperature (c) compared to the computed one-dimensional ZND solution at t = 555 μs.

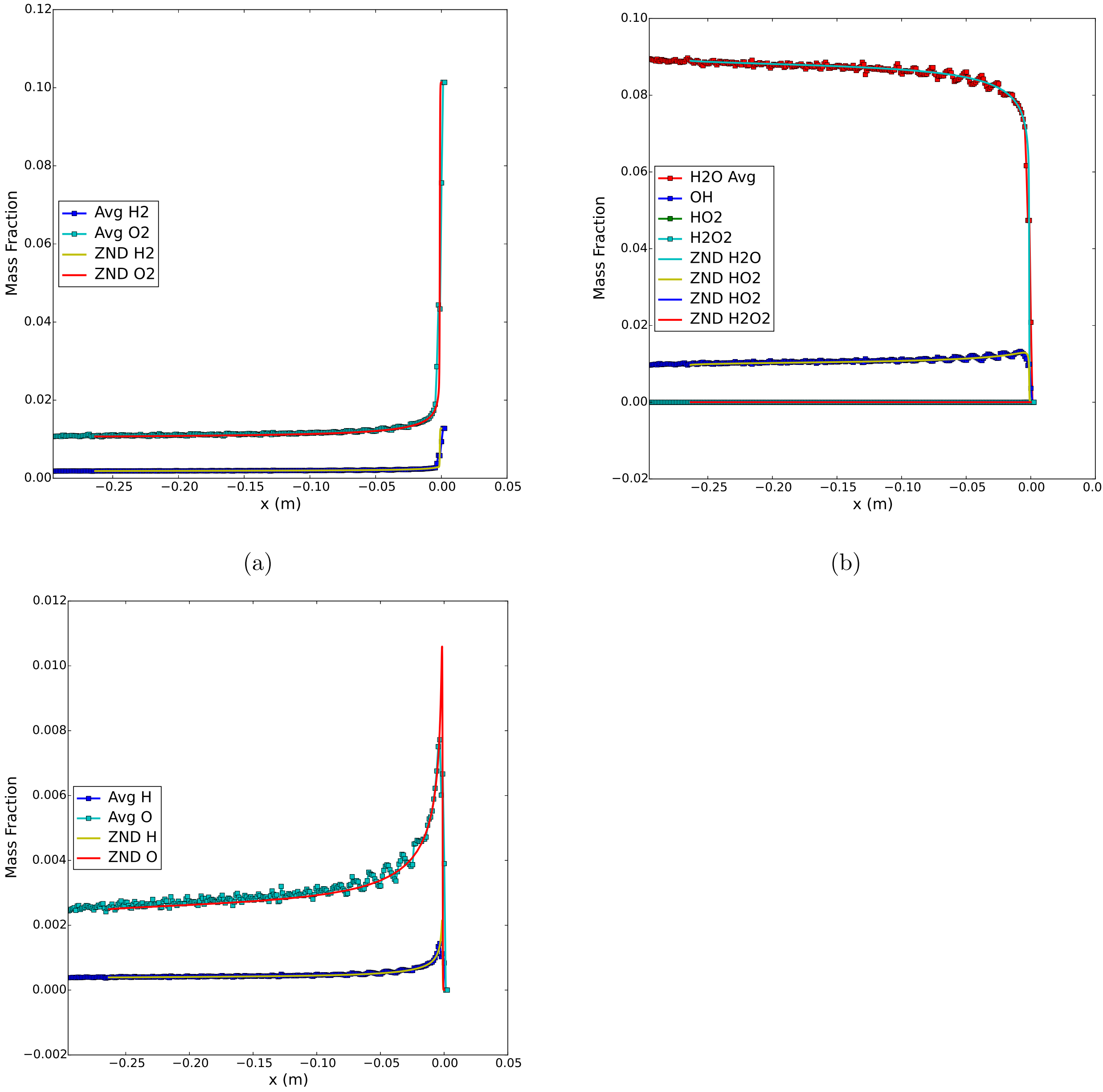

(a)

(b)

(c)

Figure 5.18: Area-averaged mass fraction of species compared to the computed one-dimensional ZND solution at t = 555 μs.

ZND structure as shown in Fig. 5.22. The oscillations and slight drift from the one-dimensional structure is expected due to the transverse wave, but the overall agreement verifies the quasi one-dimensional nature of the two-dimensional detonation in a duct as a whole. We also note that the area-averaged structure is steady with time, similar to how the ZND solution is steady, as shown in Fig. 5.19 for Mach and pressure. The comparisons of the other flow properties are located in Appendix A.4 which also support the steady-state of the area-averaged properties.

Next, comparing the area-averaged results with the analytical post-CJ structure shows excellent agreement for u-velocity and density while there is disagreement in temperature and pressure which also manifests in a disagreement in Mach. There is also a distinct constant state region and an expansion fan region as expected from the theory.

The disagreement in temperature is large because of the combination of the adiabatic wall boundary conditions and the unreacted pocket that remains behind as the detonation front propogates forward. Adiabatic walls do not allow heat flux through the walls and the unreacted pocket continues to produce chemical reactions which generates heat that is trapped within the duct. Because there is now heat being added, our isentropic assumption fails and the flow quantities we expect increasingly disagrees with the post-CJ structure as time progresses further and more heat is added.

The $H_2 - O_2 - AR$ composition is known to result in a weak detonation, otherwise known as the eigenvalue detonation, where the chemical equilibrium is not achieved at the sonic point. These eigenvalue detonations are known to result in the supersonic motion of the fluid particles relative to the detonation front at the CJ-plane (Fickett & Davis, 1979). This indicates that the sonic plane and CJ-plane are not at the same location as the idealized detonation theory predicts. The results shown in Fig. 5.22 agree with these predictions where the absolute value of the fluid particle Mach is approximately 1.03, supersonic. The CJ-plane indicated in Fig. 5.22 was located by where the area-averaged pressure equals the CJ-pressure calculated from Eqn. (2.11). This difference between the CJ-plane and sonic-plane results in the step between the analytical post-CJ structure and ZND solution at the

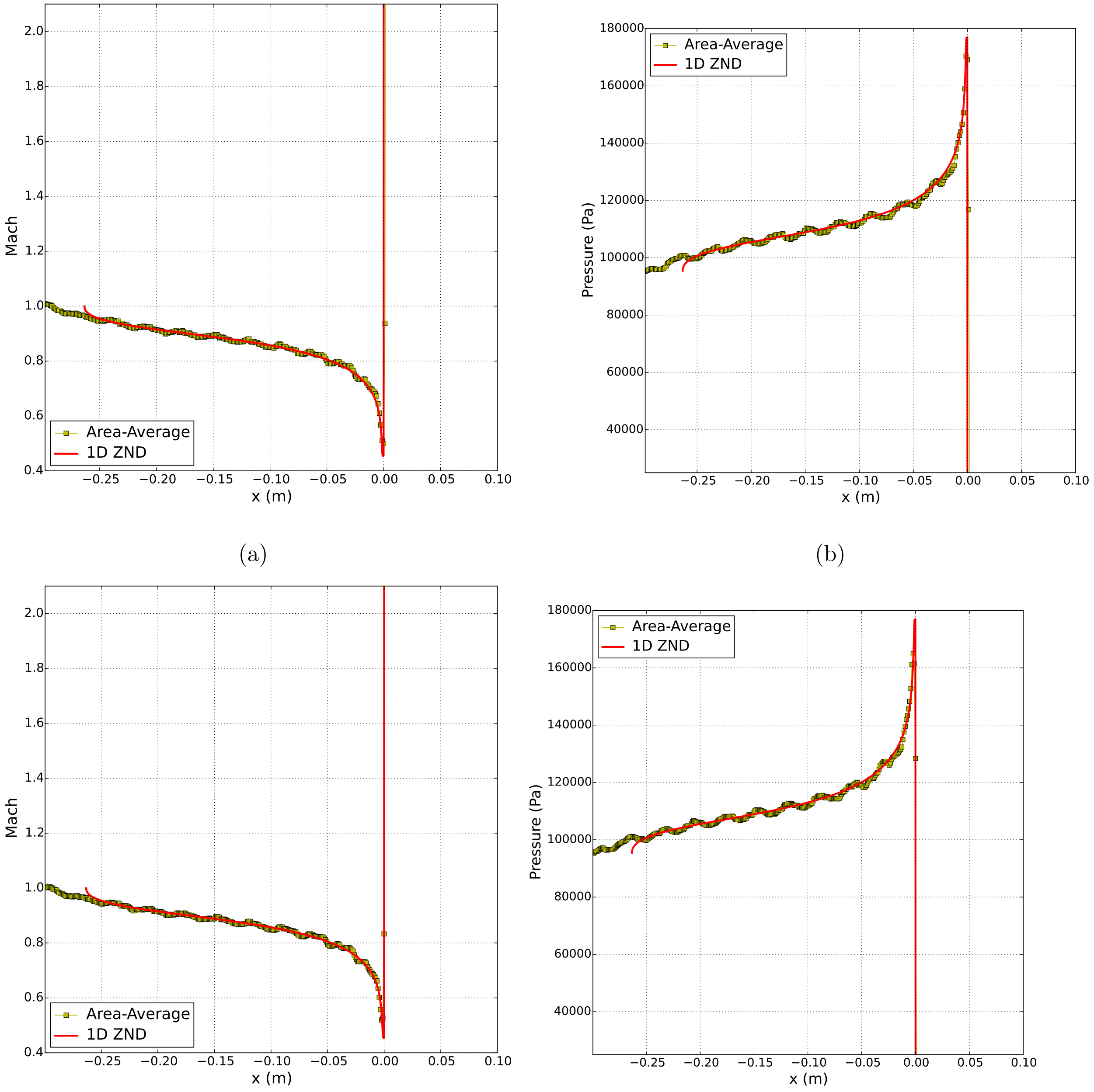

(a) (b)

(c) (d)

Figure 5.19: Area-averaged Mach and pressure in the reference frame attached to the detonation front compared to the computed one-dimensional ZND solution at t = 575 μs (a,b) and 605 μs (c,d).

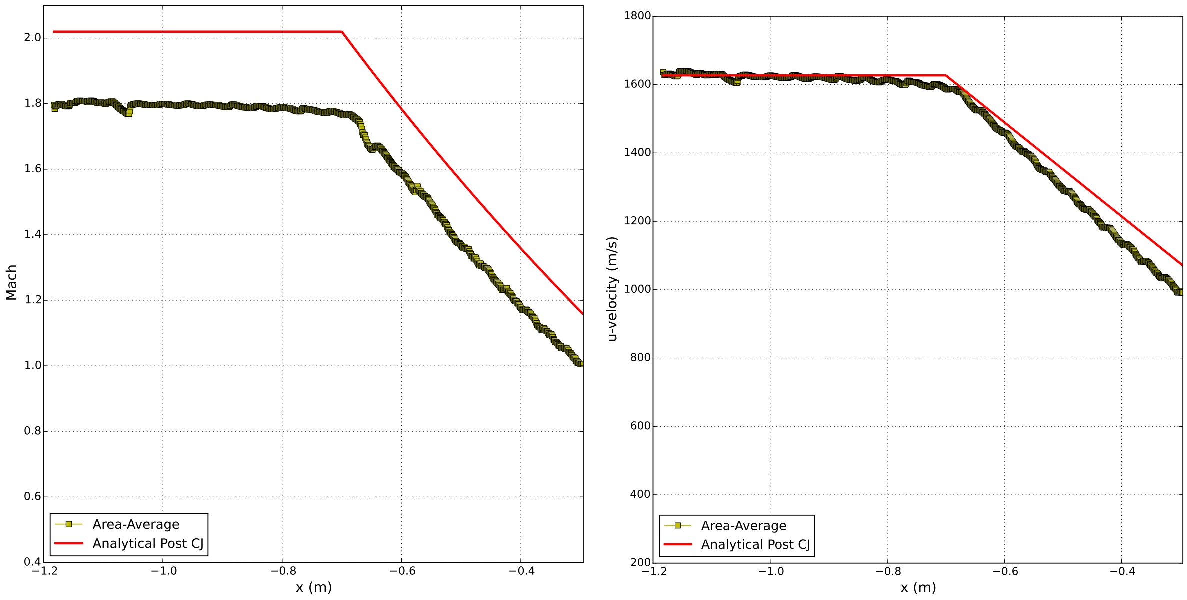

(a) (b)

Figure 5.20: Area-averaged Mach (a) and u-velocity (b) in the reference frame attached to the detonation front compared to the the analytical post CJ-structure at t = 555 μs.

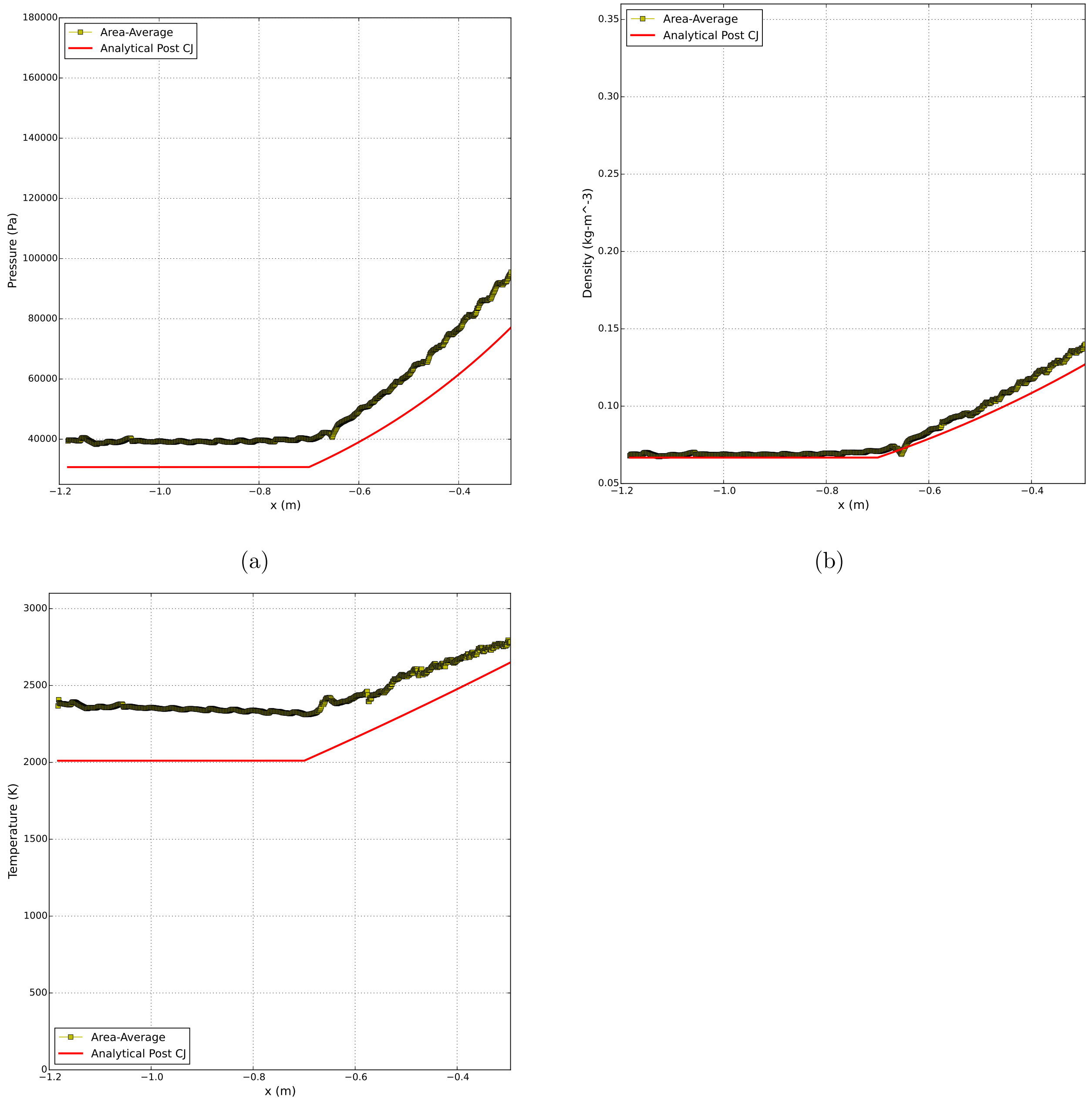

(a)

(b)

(c)

Figure 5.21: Area-averaged pressure (a), density (b), and temperature (c) compared to the the analytical post CJ-structure at t = 555 μs.

sonic plane.

5.2.4 Particle Tracking Comparisons

With the area-averaged flow properties showing excellent agreement with the one-dimensional ZND solution, it will now be used for comparisons of fluid particles' properties that are tracked from the detonation front to the sonic point. Seven particles were chosen roughly symmetrically along the detonation front, as shown in Fig. 5.24. The particles were tracked by taking the particle velocity, in the detonation front reference frame, in the x and y-direction and progressing it forward to the next time step, Fig. 5.23. Consequently, the particle paths were only as accurate as the time step size between each point. For efficiency reasons, the time step size used for the particle paths near the detonation front was much smaller than that used as the particles were tracked further from the detonation front because the flow became increasingly one-dimensional away from the detonation front.

Although the detonation is complex and two-dimensional, the movement of the particles are dominated by a quasi one-dimensional behavior as shown in Fig. 5.24. There is little movement in the y-direction compared to the x-direction as the particles move downstream from the detonation front because the cross-current dynamics of the detonation front quickly decays. In fact, it seems that the particles always stayed either above or below the centerline of the duct. This indicates that the flow behavior becomes increasingly one-dimensional away from the front and that the two-dimensional behavior of the flow is concentrated near the detonation front as expected from the cross-current dynamics. Further movement of the particles in the y-direction downstream from the detonation front are attributed to the vorticity generated from the detached shear lines.

The ratio of the v-velocity to u-velocity, in the reference frame attached to the detonation front, of the particles is examined in Fig. 5.25. The velocity ratio for the particles quantifies the quasi one-dimensional nature of the particles away from the detonation front. The particles experience greater movement in the vertical direction compared to the horizontal direction at the detonation front due to the cross-current dynamics; however, the

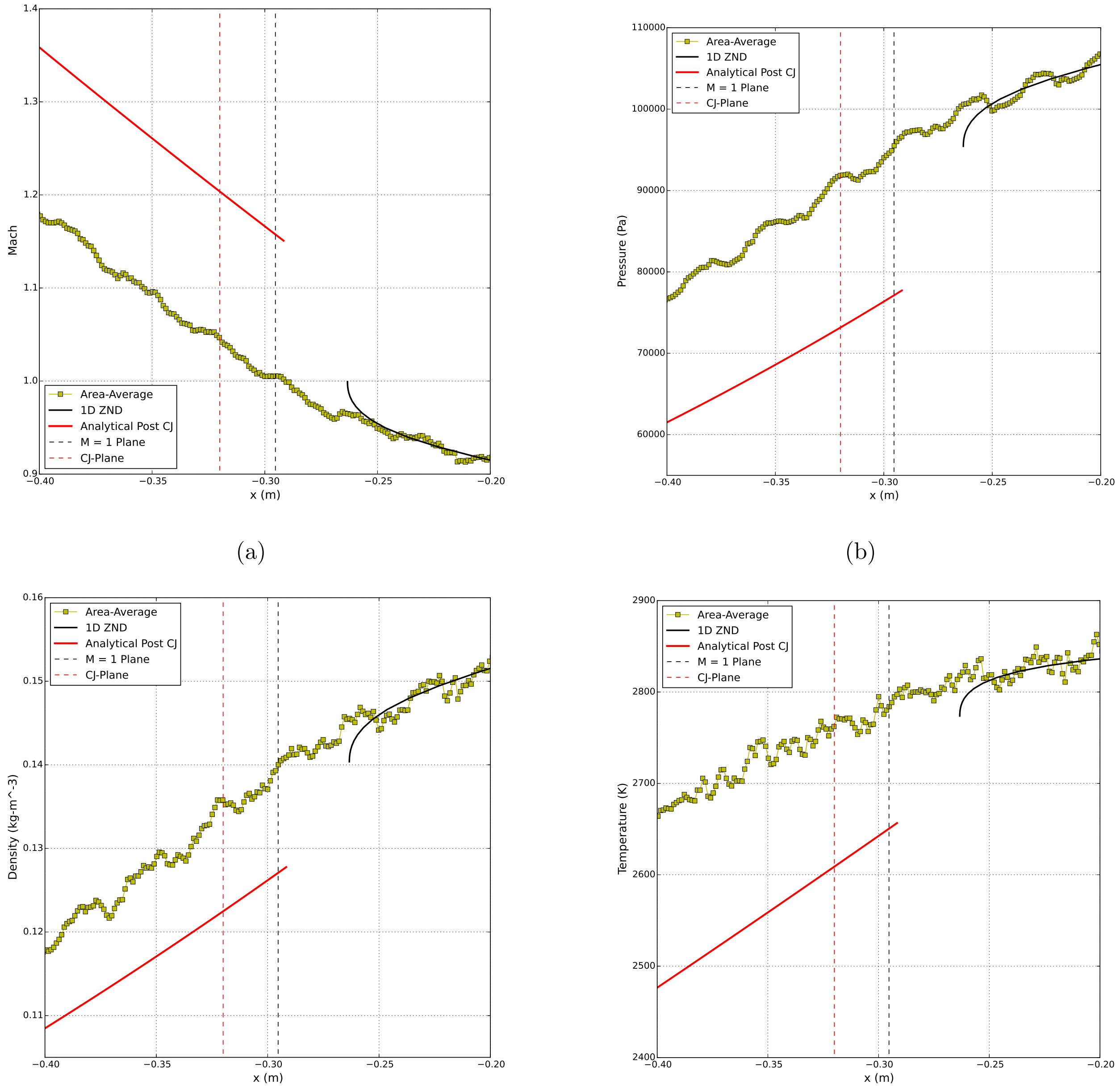

(a) (b)

(c) (d)

Figure 5.22: Magnified view of the area-averaged Mach (a), pressure (b), density (c), and temperature (d) in the reference frame attached to the detonation front compared to the computed one-dimensional ZND solution and the analytical post CJ-structure at t = 555 μs. The sonic plane and CJ-plane are both also shown.

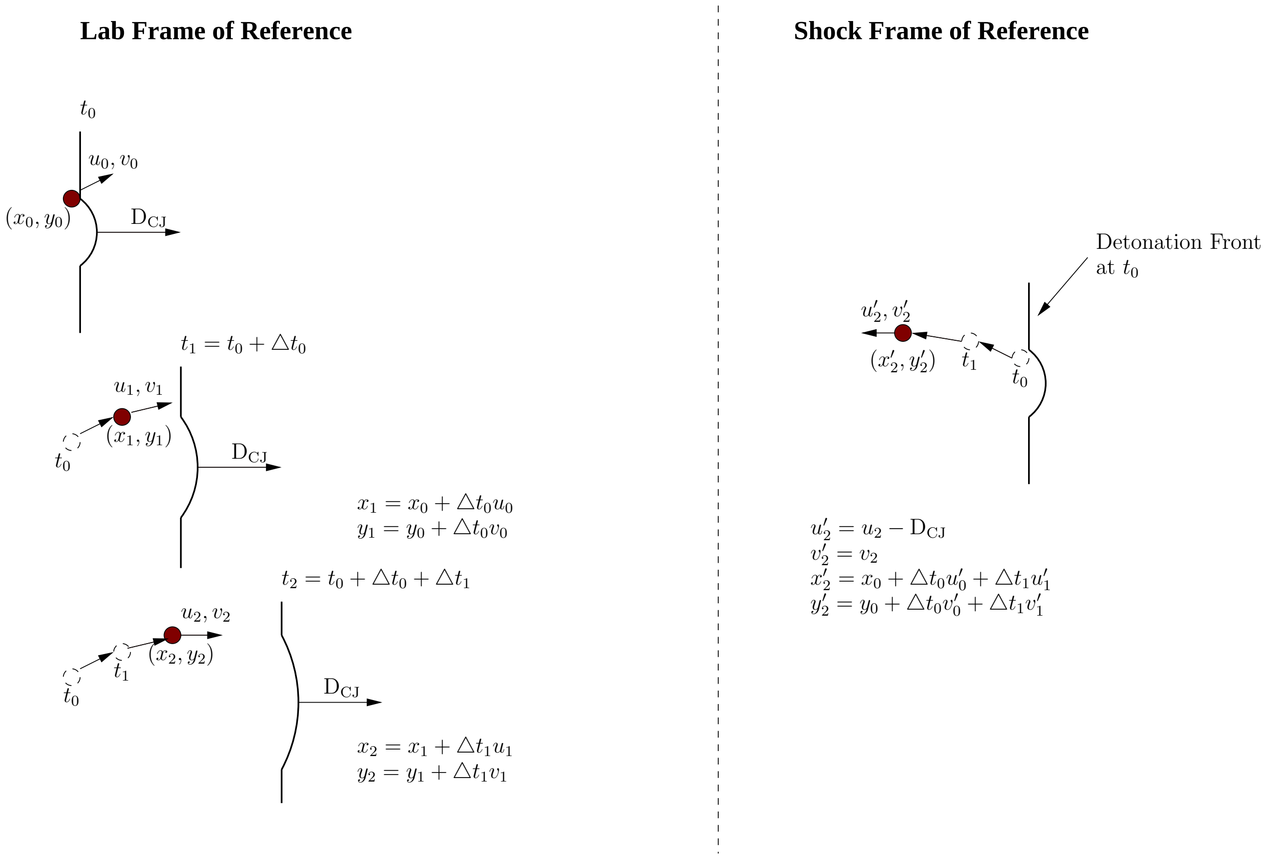

Figure 5.23: Visual representation of the particle tracking method. In the shock reference frame, the detonation front from the initial release time of the particles is shown.

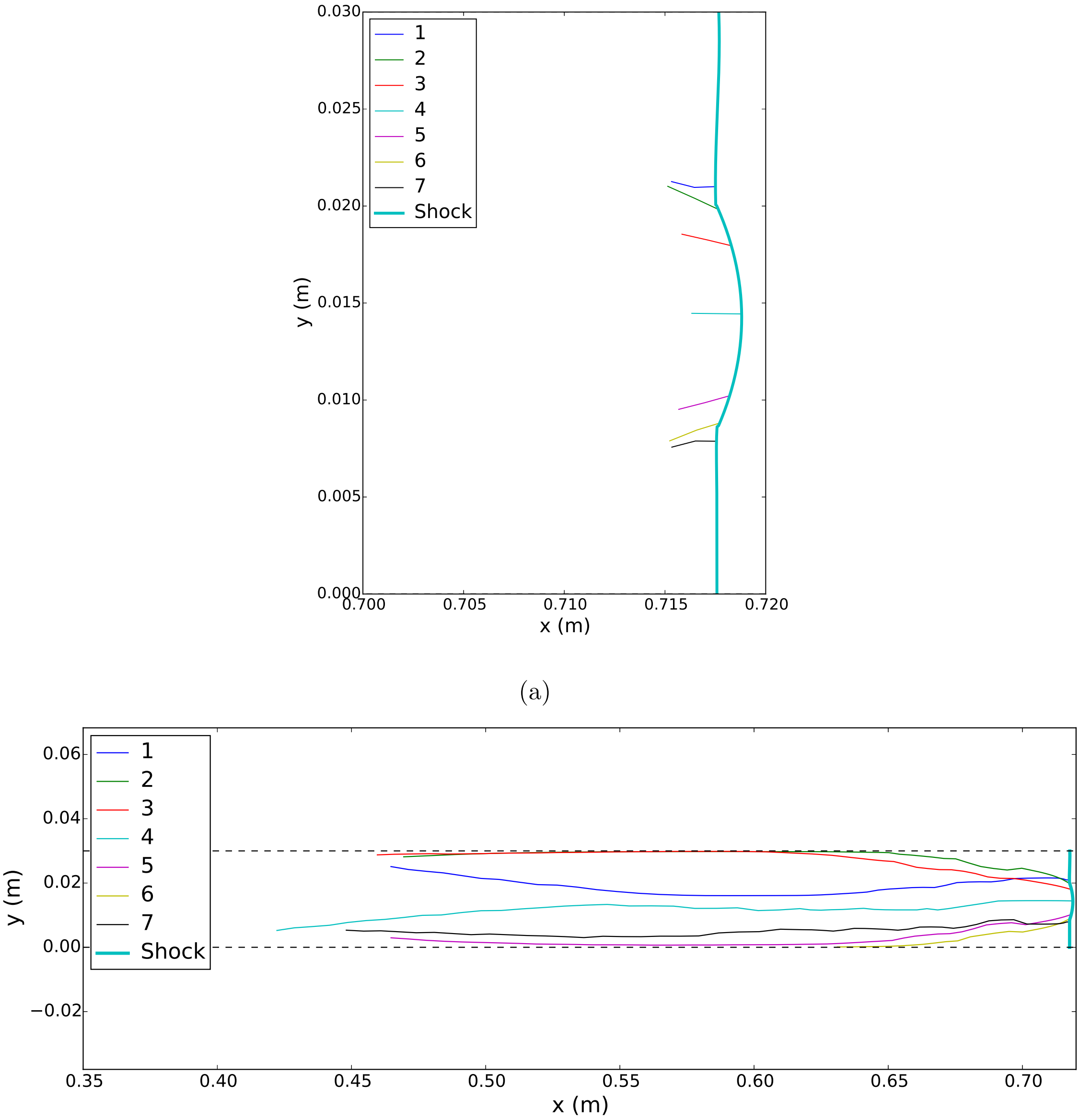

(a)

(b)

Figure 5.24: (a) Zoomed in view of the origin of the particle pathlines and (b) detonation front reference frame of 7 particle pathlines tracked to the sonic point where the dashed black line represents the upper and lower walls of the duct. The particles were tracked from t = 270 μs to 645 μs.

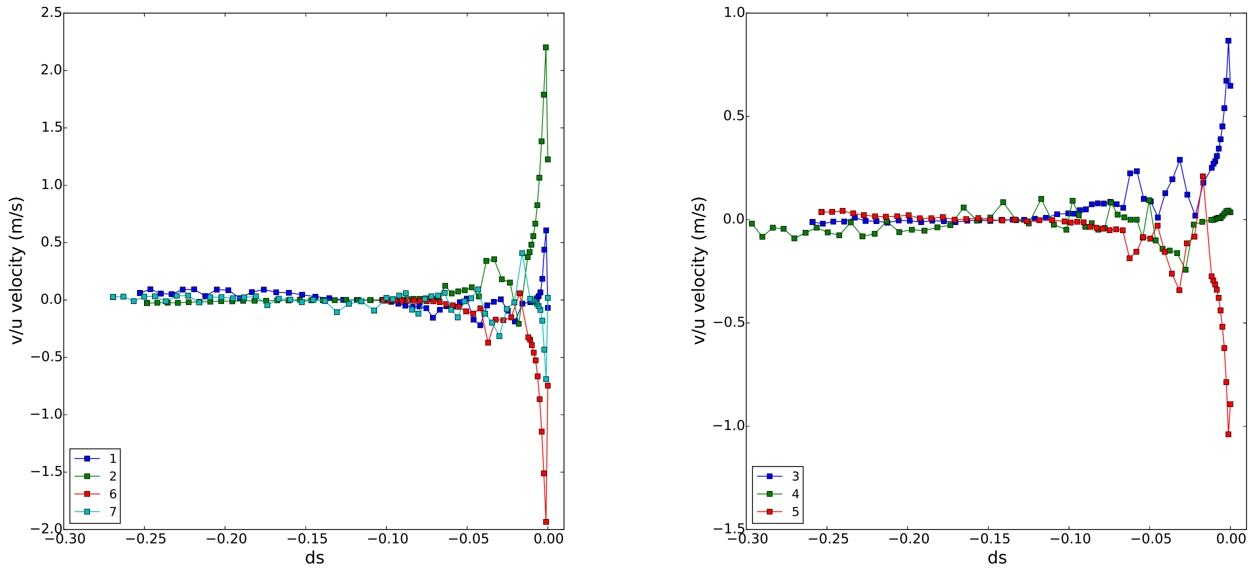

(a)

(b)

Figure 5.25: Ratio of v-velocity to u-velocity, in the reference frame attached to the detonation front, of particles that are tracked from the detonation front to after the sonic plane.

cross-current quickly decays downstream. The particles quickly accelerate away from the detonation front as the lateral movement decays which transitions the particles to move in a quasi one-dimensional trajectory.

Figure 5.26 to 5.29 plots the particle properties along the particle path, ds, along with the area-averaged flow properties along the duct at t = 555 μs up to the sonic point of each particle. The results show overall that the particles also follow the one-dimensional ZND structure along their path. Near the detonation front, the particles naturally overshoot the ZND structure because of the two-dimensional detonation front, but they quickly converge to oscillate around the ZND structure. The combination of the transverse wave and Mach stem produces a larger jump in the particle properties than the ZND adiabatic shock, especially at the triple points. The oscillation of u-velocity, pressure, density, and temperature is attributed to the particles passing through the old shear lines, triple point tracks, and the transverse wave downstream of the detonation.

The relative u-velocity of the particles have a greater spread than the other properties relative to the ZND structure. As a result, the particles reach the sonic point at different times. Particles 6 was noted to leave the domain before reaching the sonic point because we assumed the slip-walls to be a symmetry boundary. Particles 1, 2, and 7 are noted to be the first particles to reach the sonic point, before the ZND model, and these are the particles that were tracked near the triple points. The particle that was tracked from the middle region of the Mach stem, 4, traveled a further distance to reach a sonic velocity.

Particle Tracking of Multiple Particles

Another interesting observation was that the sonic plane is not a straight line perpendicular to the horizontal duct walls as the ZND theory predicts. In fact, the particles tend to reach the sonic point fastest at the upper and lower walls and last near the middle of the domain as shown in Fig. 5.30, which illustrates multiple particles tracked along the detonation front up to the sonic point. The pattern of when the particles reach the sonic point seems to be correlated to the shape of the detonation front such that particles reach the sonic point last in the center of the domain and first near the walls.

The same particle properties from the original seven particles are shown in Fig. 5.31 and 5.32. All the particles that were tracked follow the original one-dimensional ZND detonation that was used to initiate the simulation. At the detonation front, the majority of the particles experience a larger jump in their properties than the ZND jump as previously explained, but the properties quickly converge to oscillate around the one-dimensional solution. The v-velocity to u-velocity ratio of all the particles that were tracked also illustrates how the particles quickly transitions to a one-dimensional motion as they move away from the detonation front.

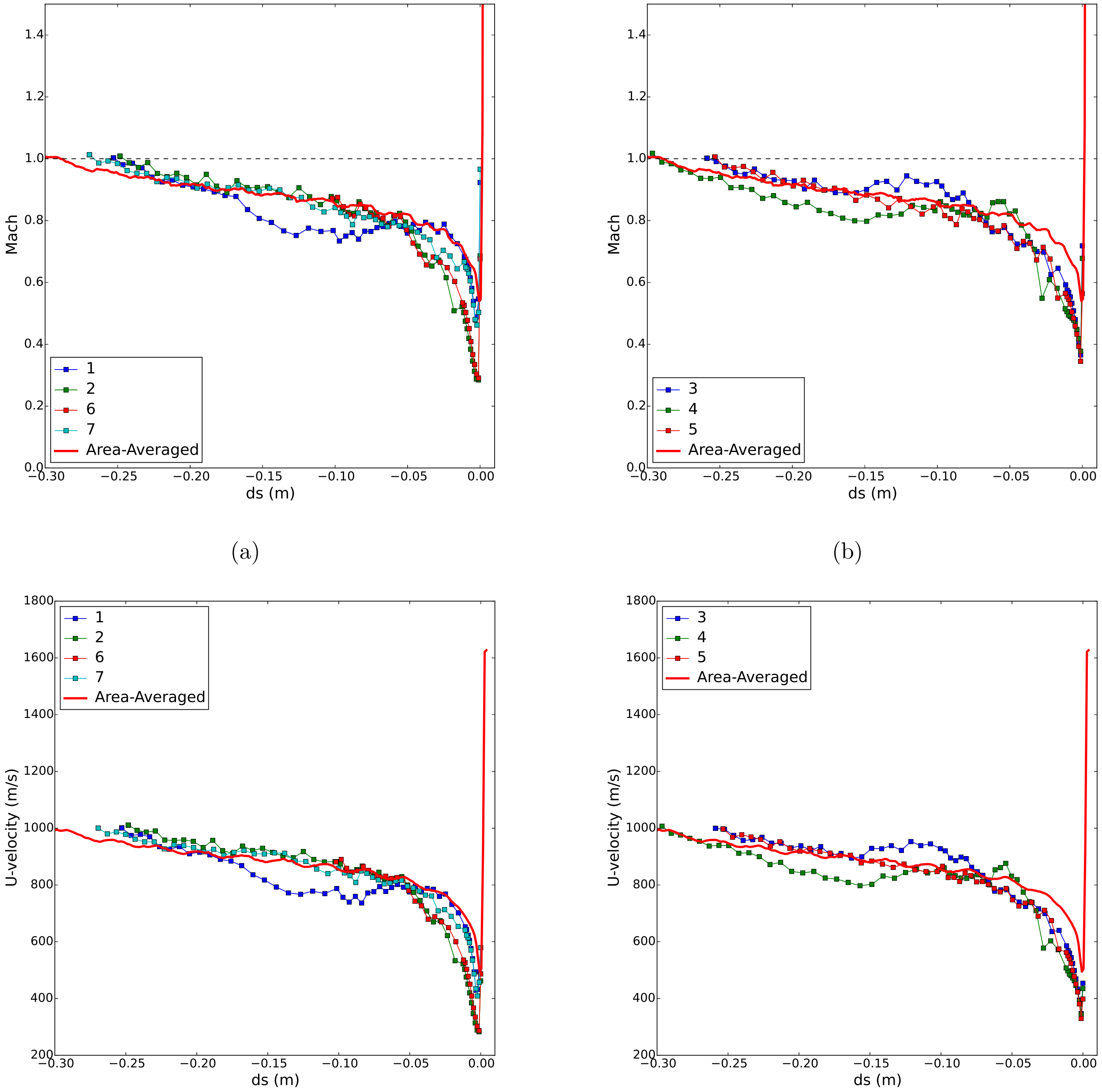

(a)

(b)

(c)

(d)

Figure 5.26: Mach (a,b)) and u-velocity (c,d) in the reference frame attached to the detonation front of particles that are tracked from the detonation front to after the sonic plane are plotted with the area-averaged properties.

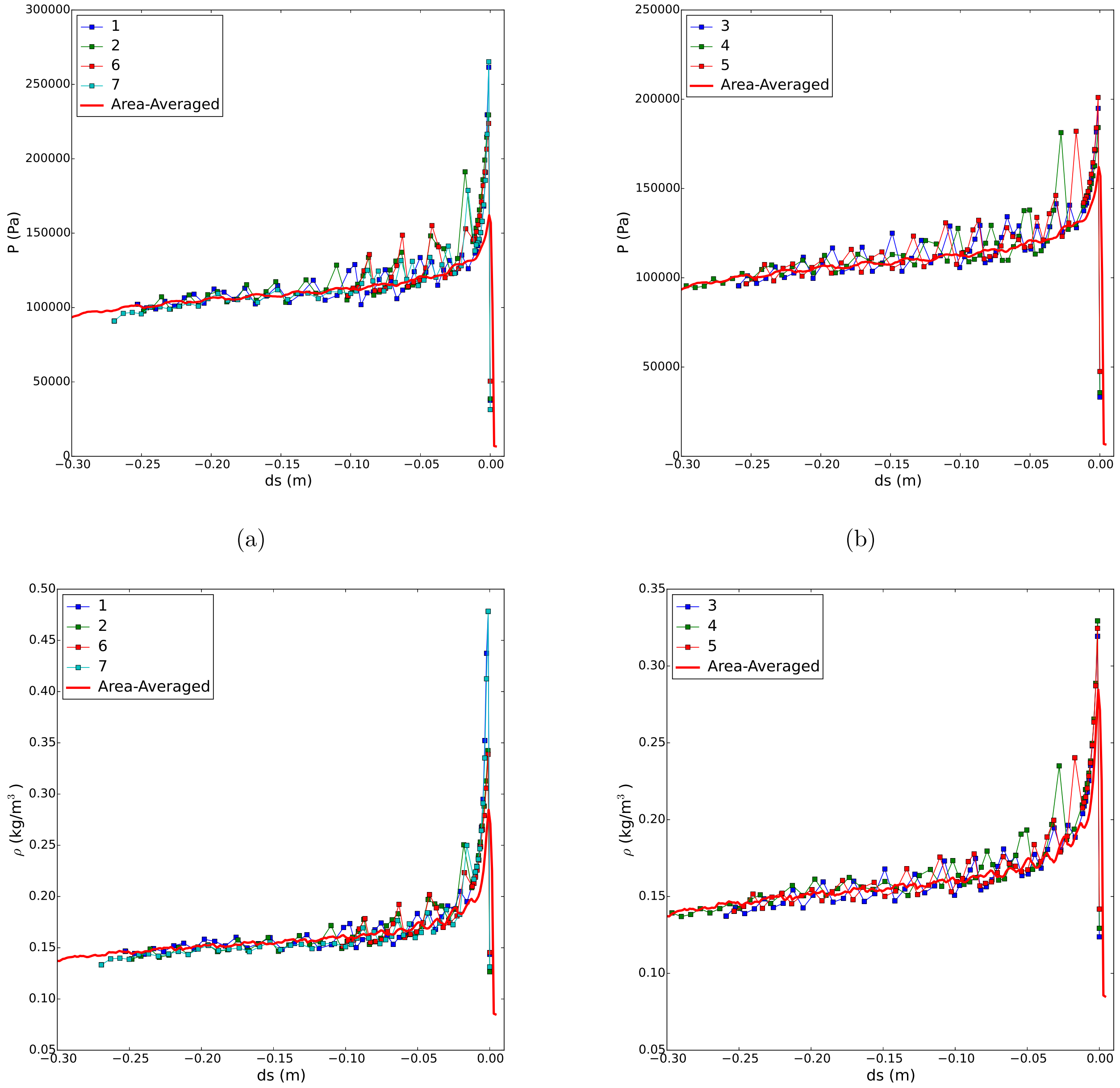

(a)

(b)

(c)

(d)

Figure 5.27: Pressure (a,b) and density (c,d) of particles that are tracked from the detonation front to after the sonic plane are plotted with the area-averaged properties.

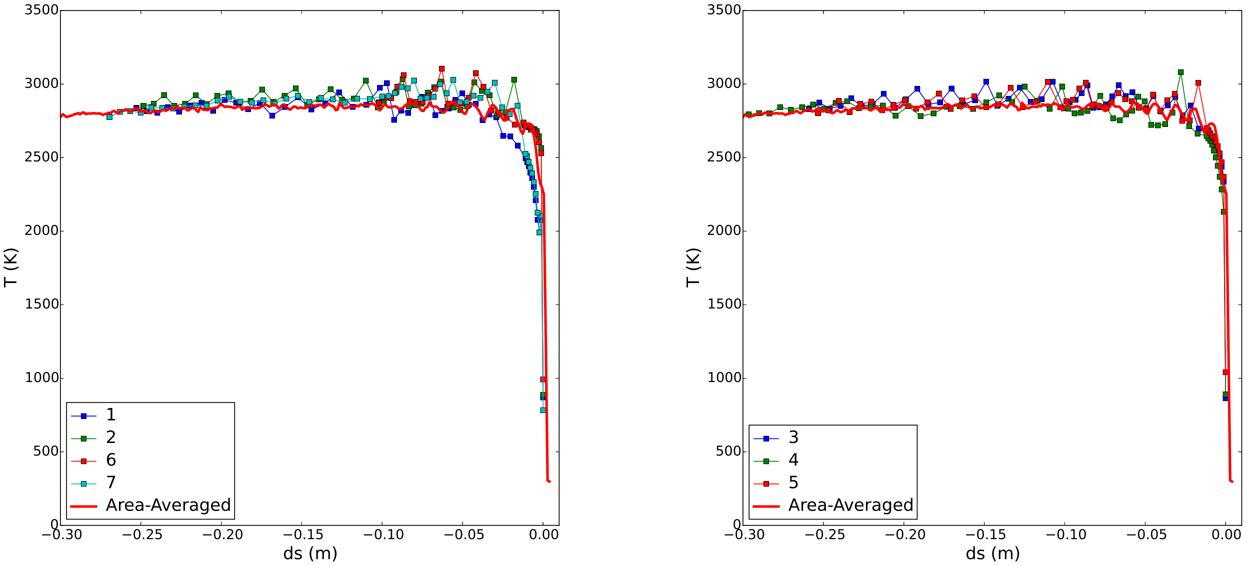

(a)

(b)

Figure 5.28: Temperature of particles that are tracked from the detonation front to after the sonic plane.

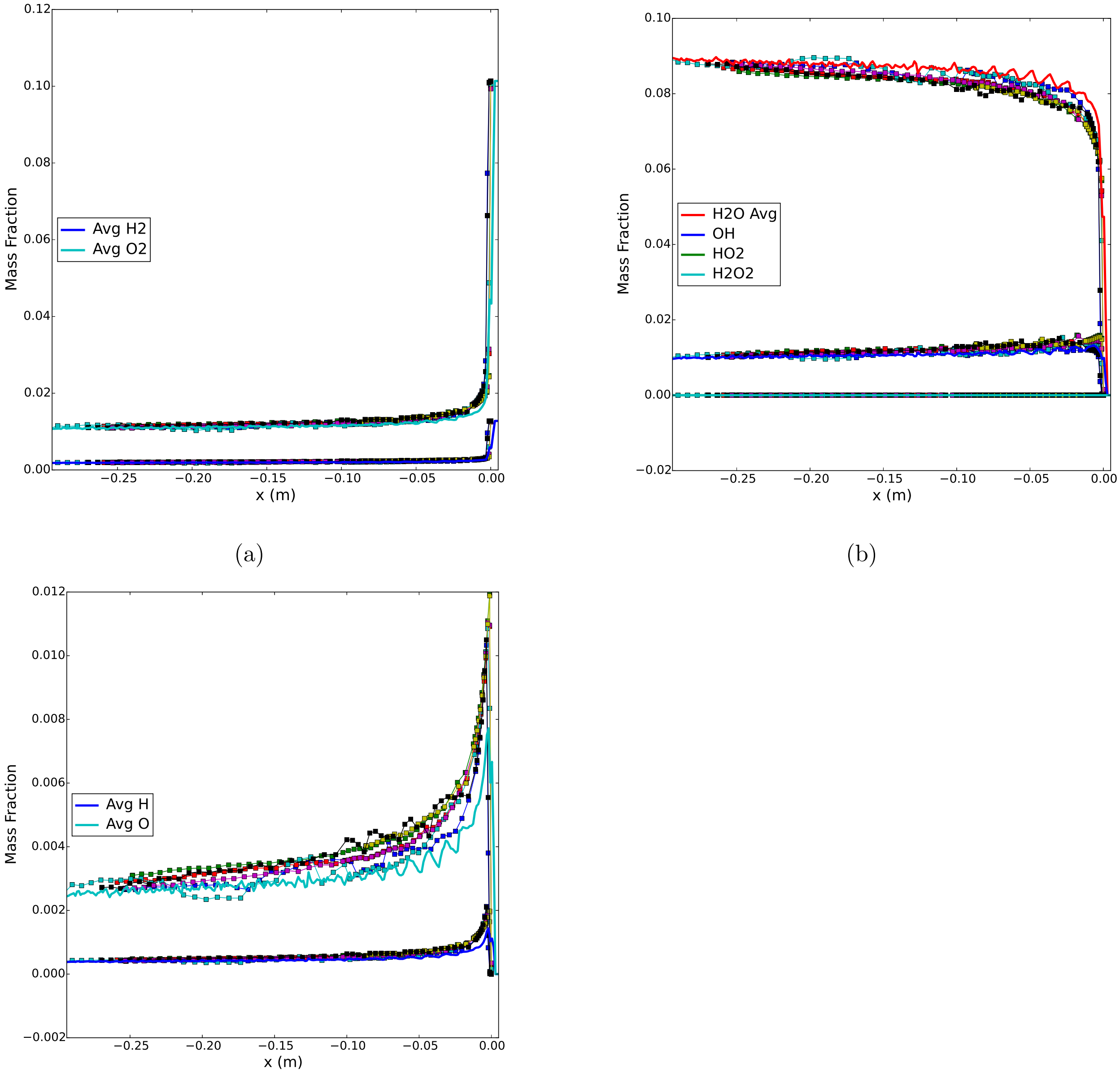

(a)

(b)

(c)

Figure 5.29: Species mass fraction of particles that are tracked from the detonation front to after the sonic plane are plotted with the area-averaged properties.

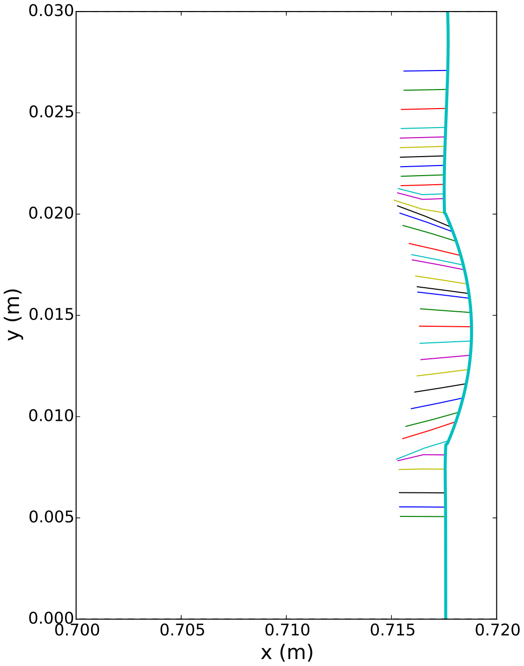

(a)

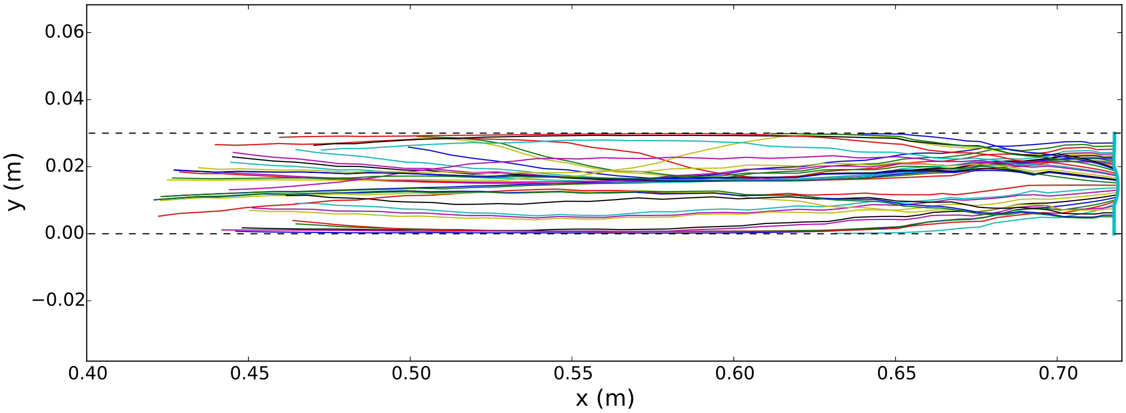

(b)

Figure 5.30: (a) Zoomed in view of the origin of the particle pathlines and (b) detonation front reference frame of multiple particle pathlines to their sonic point. The particles were tracked from t = 270 μs to 645 μs.

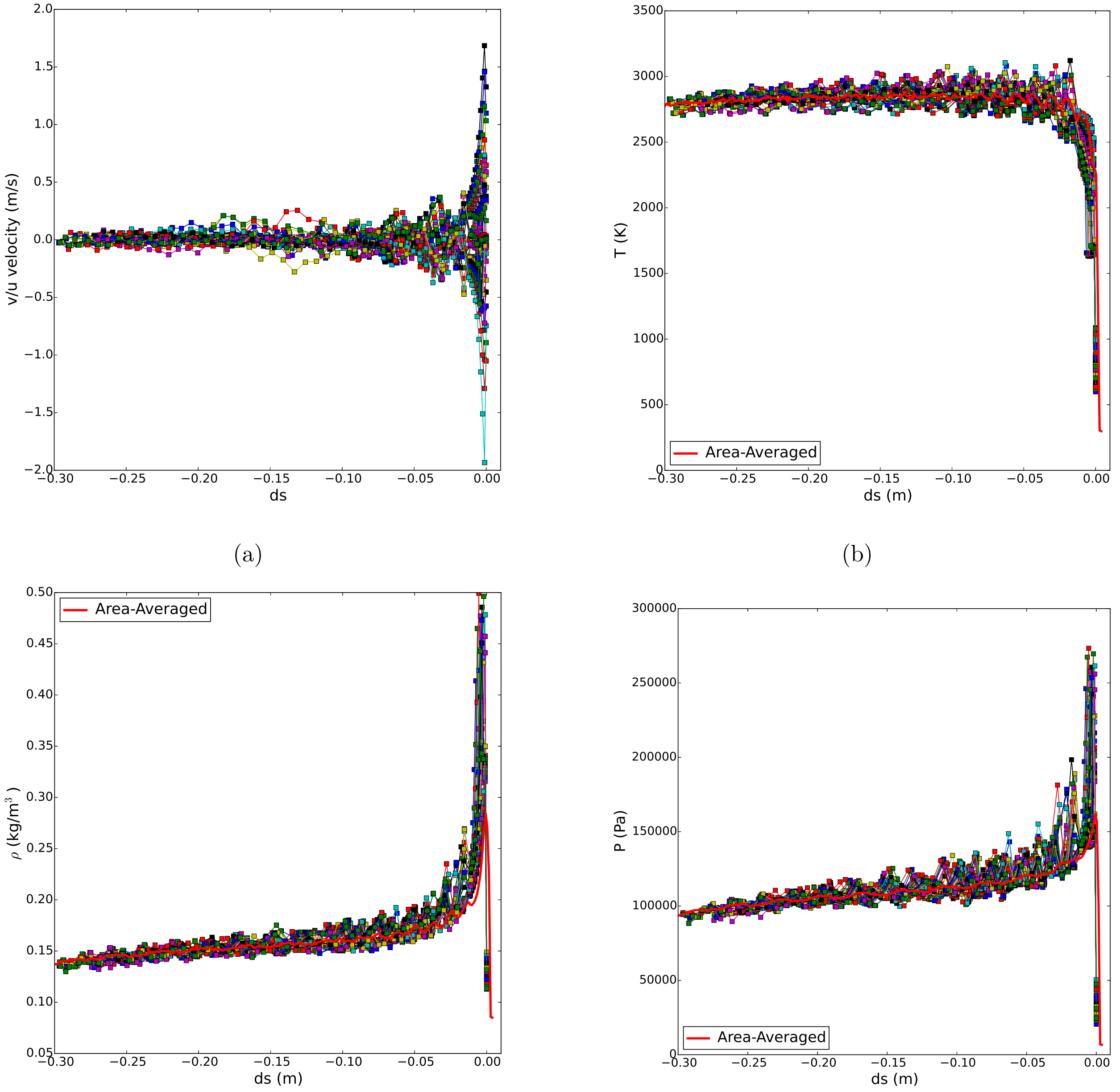

(a) (b)

(c) (d)

Figure 5.31: Ratio of v-velocity to u-velocity, in the reference frame attached to the detonation front (a), temperature (b), density (c), and pressure (d) of multiple particles that are tracked from the detonation front to after the sonic plane are plotted with the area-averaged properties.

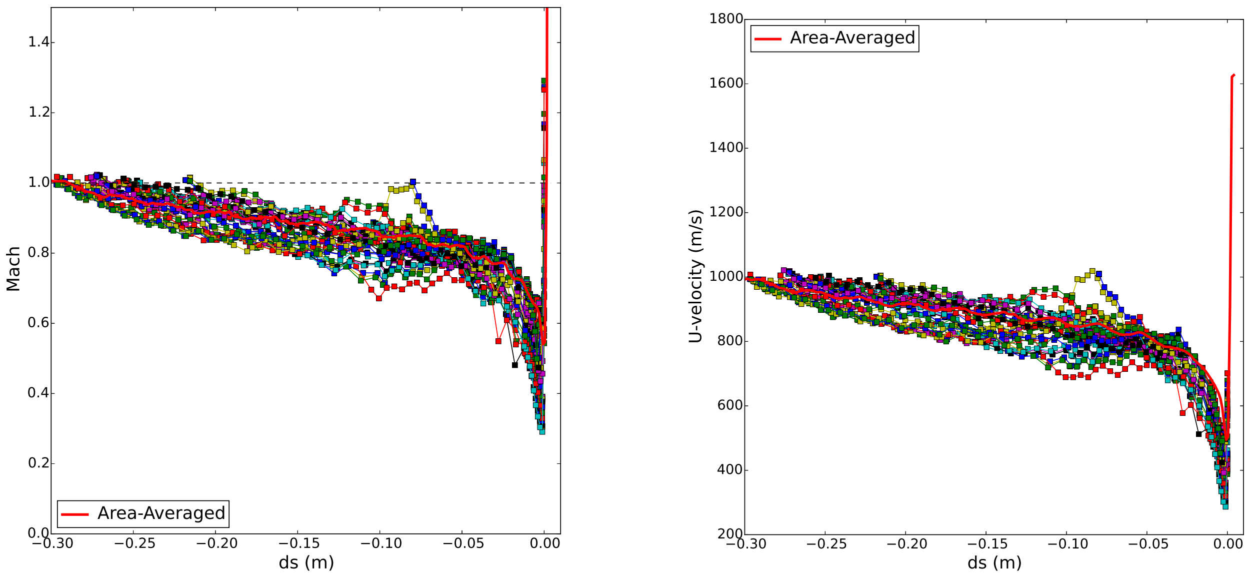

(a) (b)

Figure 5.32: Mach (a) and u-velocity (b), in the reference frame attached to the detonation front, of particles that are tracked from the detonation front to after the sonic plane are plotted with the area-averaged properties.

Chapter 6

CONCLUSIONS

The one-dimensional ZND theory has laid the foundation for detonation research and we have used it illustrate the quasi one-dimensional behavior of the two-dimensional detonations in a duct. We analyzed the area-averaged and particle properties of a detonation propagating in a duct from the closed end and discovered how well the one-dimensional detonation solution can model these properties. The area-averaged properties almost perfectly follow the one-dimensional solution and proved to be steady with time. Despite all the complex processes within the detonation, even the particle properties followed the one-dimensional structure. There was greater disagreement in the properties near the detonation front because the Mach stem and incident shock was stronger than the idealized ZND shock, and the existence of the transverse wave at the triple points produced another large jump in the flow properties in addition to the detonation front. Further downstream from the detonation front, the particle properties converged to slightly oscillate around the ZND solution.

As the particles traversed downstream from the detonation front, we also discovered how quickly the motion of the particles transitioned to a one-dimensional motion, in the reference frame attached to the detonation front. At the front of the detonation front, the cross-current dynamics influenced the motion of the particles. Away from the detonation front, the cross-current dynamics decayed and the particles accelerated in a quasi one-dimensional direction.

The simulations used in this work have adopted the AMR capabilities from the AMROC framework and follow the work of Deiterding and Oran to first verify our results. We incorporated a high order WENO-TCD discretization method which has been praised for its accuracy in solving hyperbolic conservation equations with discontinuities in the solution. This allowed us to solve the complex processes within the detonation and recreate the same results that Deiterding, Oran, and many other researchers have found as well as analyze the particle properties.

BIBLIOGRAPHY

Berger, M.J. & Colella, P. 1989 Local adaptive mesh refinement for shock hydrodynamics. *J. Comput. Physics* **82** (1), 64–84.

Berger, M.J. & Oliger, J. 1984 Adaptive mesh refinement for hyperbolic partial equations. *J. Comput. Physics* **53**, 484–512.

Boris, J. P., Oran, E. S., Peters & Rogg 1982 H2-o2-ar reaction mechanism from: Weak and strong ignition.

Browne, S., Ziegler, J. & Shepherd, J. E. 2004 Numerical solution methods for shock and detonation jump conditions. *Tech. Rep.*. GALCIT.

Deiterding, R. 2003 *Parallel Adaptive Simulation of Multi-dimensional Detonation Structures*. PhD thesis, Brandenburgische Technische Universität Cottbus.

Fickett, W. & Davis, W. 1979 *Detonation*. University of California Press.

Hill, D. J. & Pullin, D. I. 2004 Hybrid tuned center-difference-WENO method for large eddy simulations in the presence of strong shocks. *J. Comput. Physics* **194**, 435–450.

Hirsch, C. 2007 *Numerical Computation of Internal and External Flows*, 2nd edn., , vol. 1. Elsevier.

Kerr, R.J., Miller, J.A & Jefferson, T.H 1980 CHEMKIN: A General-Purpose, Problem-Independent, Transportable, Fortran Chemical Kinetics Code Package. Rep. Sandia National Laboratory.

Kurosaka, M. & Tsuboi, N. 2014 Spinning detonation, cross-currents, and the chapman-jouguet velocity. *Journal of Fluid Mechanics* **756**, 728–757.

LEE, J. H.S. 2008 *The Detonation Phenomenon*. Cambridge University Press.

LEVEQUE, R. J. 2002 *Finite Volume Methods for Hyperbolic Problems*. Cambridge University Press.

LOMBARDINI, M. 2008 Richtmyer-Meshkov instability in converging geometries. PhD thesis, California Institute of Technology.

RADULESCU, M.I., SHARPE, G.J., LAW, C.K. & LEE, J.H.S. 2007 The hydrodynamic structure of unstable cellular detonations. *J. Fluid Mech.* **580**.

SHEPARD, J. E. 2000 Znd structure computation. http://www.galcit.caltech.edu/ jeshep.

STREHLOW, R.A. 1968 Gas pase detonations: Recent developments. *Combustion and Flame* **12** (2), 81–101.

Appendix A

APPENDICES

A.1 Derivation of Analytical ZND Structure

The derivation of the ZND structure as a function of the progress variable, λ, will now be proven for a detonation in a constant area duct. We first start with the governing equations.

$$\rho_0 u_0 = \rho_1 u_1 \tag{A.1}$$

$$\mathrm{p}_0 + \rho_0 u_o^2 = \mathrm{p}_1 + \rho_1 u_1^2 \tag{A.2}$$

$$h_{t_1} - h_{t_0} = q \tag{A.3}$$

where $h_t = h + \frac{u^2}{2}$. Setting Eqn. (A.1) in terms of Mach, $\mathrm{M} = \frac{u}{a}$

$$\begin{gathered} \rho_0 \mathrm{M}_0 \sqrt{\mathrm{T}_0} = \rho_1 \mathrm{M}_1 \sqrt{\mathrm{T}_1} \\ \frac{\rho_1}{\rho_0} = \frac{\mathrm{M}_0}{\mathrm{M}_1}\sqrt{\frac{\mathrm{T}_0}{\mathrm{T}_1}} \end{gathered} \tag{A.4}$$

Dividing Eqn. (A.2) by (A.1) gives

$$\begin{gathered} \frac{\mathrm{p}_0}{\rho_0 u_0} + u_0 = \frac{\mathrm{p}_1}{\rho_1 u_1} + u_1 \\ \mathrm{R}\frac{\mathrm{T}_0}{u_0} + u_0 = \mathrm{R}\frac{\mathrm{T}_1}{u_1} + u_1 \end{gathered} \tag{A.5}$$

Equation (A.5) may now be written in terms of Mach by

$$\begin{gathered} \left(\frac{1}{\mathrm{M}_0} + \gamma \mathrm{M}_0\right)\sqrt{\mathrm{T}_0} = \left(\frac{1}{\mathrm{M}_1} + \gamma \mathrm{M}_1\right)\sqrt{\mathrm{T}_1} \\ \frac{\mathrm{T}_1}{\mathrm{T}_0} = \left(\frac{\mathrm{M}_1}{\mathrm{M}_0}\right)^2 \left(\frac{1+\gamma \mathrm{M}_0^2}{1+\gamma \mathrm{M}_1^2}\right)^2 \end{gathered} \tag{A.6}$$

Substituting Eqn. (A.6) into (A.4)

$$\frac{\rho_1}{\rho_0} = \left(\frac{\mathrm{M}_0}{\mathrm{M}_1}\right)^2 \frac{1+\gamma \mathrm{M}_1^2}{1+\gamma \mathrm{M}_0^2} \tag{A.7}$$

Using the ideal gas law to define a pressure ratio yields

$$\frac{\mathrm{p}_1}{\mathrm{p}_0} = \frac{\rho_1}{\rho_0}\frac{\mathrm{T}_1}{\mathrm{T}_0} \tag{A.8}$$

which is used to write Eqn. (A.7) as

$$\frac{\mathrm{p}_1}{\mathrm{p}_0} = \frac{1+\gamma \mathrm{M}_0^2}{1+\gamma \mathrm{M}_1^2} \tag{A.9}$$

We now define the total enthalpy in terms of Mach

$$h_t = \mathrm{c_p T}\left(1+\frac{\gamma-1}{2}\mathrm{M}^2\right) \tag{A.10}$$

such that we can use this definition in Eqn. (A.3) and divide by $\mathrm{c_p T_0}$ to yield

$$\frac{\mathrm{T}_1}{\mathrm{T}_0}\left(1+\frac{\gamma-1}{2}\mathrm{M}_1^2\right) - \left(1+\frac{\gamma-1}{2}\mathrm{M}_0^2\right) = \frac{q}{\mathrm{c_p T_0}} \tag{A.11}$$

Now we substitute Eqn. (A.6) into (A.11) to get

$$\frac{q}{\mathrm{c_p T_0}} = \left(\frac{\mathrm{M}_1}{\mathrm{M}_0}\right)^2 \left(\frac{1+\gamma \mathrm{M}_0^2}{1+\gamma \mathrm{M}_1^2}\right)^2 \left(1+\frac{\gamma-1}{2}\mathrm{M}_1^2\right) - \left(1+\frac{\gamma-1}{2}\mathrm{M}_0^2\right) \tag{A.12}$$

At the CJ-point, the reaction is assumed to have ceased and the total heat release is Q. We also know at the CJ-point $\mathrm{M}_1 = 1$ and that the detonation front propagates with speed $\mathrm{M}_0 = \mathrm{M_{CJ}}$. Using these known conditions at the CJ point, Eqn. (A.12) becomes

$$\begin{gathered}\frac{\mathrm{Q}}{\mathrm{c_p T_0}} = \left(\frac{1}{\mathrm{M_{CJ}}}\right)^2 \left(\frac{1+\gamma \mathrm{M_{CJ}^2}}{1+\gamma}\right)^2 \left(1+\frac{\gamma-1}{2}\right) - \left(1+\frac{\gamma-1}{2}\mathrm{M_{CJ}^2}\right) \\ \frac{\mathrm{Q}}{\mathrm{c_p T_0}} = \frac{(\mathrm{M_{CJ}^2}-1)^2}{2(1+\gamma)\mathrm{M_{CJ}^2}}\end{gathered} \tag{A.13}$$

Equation (A.13) may now be solved for $\mathrm{M_{CJ}}$ in terms of the total heat release, Q, by

$$\mathrm{M_{CJ}} = \sqrt{1 + \frac{\mathrm{Q}(1+\gamma)}{\mathrm{c_p T_0}}} + \sqrt{\frac{\mathrm{Q}(1+\gamma)}{\mathrm{c_p T_0}}} = \sqrt{1 + \frac{\mathrm{Q}(\gamma^2-1)}{2a_0^2}} + \sqrt{\frac{\mathrm{Q}(\gamma^2-1)}{2a_0^2}} \tag{A.14}$$

Now we will use the progress variable to determine the intermediate heating such that $q = \lambda \mathrm{Q}$ and M_1 corresponds to the $M(\lambda)$. Using these relations in Eqn. (A.12) with $\mathrm{M_0} = \mathrm{M_{CJ}}$ yields

$$\frac{\lambda \mathrm{Q}}{\mathrm{c_p T_0}} = \left(\frac{\mathrm{M_1}}{\mathrm{M_{CJ}}}\right)^2 \left(\frac{1+\gamma \mathrm{M_{CJ}^2}}{1+\gamma \mathrm{M_1^2}}\right)^2 \left(1 + \frac{\gamma-1}{2}\mathrm{M_1^2}\right) - \left(1 + \frac{\gamma-1}{2}\mathrm{M_{CJ}^2}\right) \tag{A.15}$$

Finally substituting Eqn. (A.13) into (A.15) and solving for M_1 yields

$$\mathrm{M_1} = \sqrt{\begin{aligned} &\frac{1 + \mathrm{M_{CJ}^2}\gamma^2(\sqrt{1-\lambda} - \mathrm{M_{CJ}^2}(\sqrt{1-\lambda} - 1)) + \sqrt{1-\lambda} - \mathrm{M_{CJ}^2}\sqrt{1-\lambda}}{(1 + \gamma(-\gamma + 2\mathrm{M_{CJ}^2}(1+\gamma) + (\mathrm{M_{CJ}^2} - 1)^2\gamma\lambda)} \\ &+ \frac{\gamma(1 + \sqrt{1-\lambda} - \lambda + 2\mathrm{M_{CJ}^2}\lambda - \mathrm{M_{CJ}^4}(\lambda + \sqrt{1-\lambda} - 1))}{(1 + \gamma(-\gamma + 2\mathrm{M_{CJ}^2}(1+\gamma) + (\mathrm{M_{CJ}^2} - 1)^2\gamma\lambda)} \end{aligned}} \tag{A.16}$$

Using the above relation we then are able to derive the following pressure, density, and temperature structure as a function of lambda as shown in Sec. 2.2.2.

A.2 Chemical Reaction

```
ELEMENTS H O AR

SPECIES H2 H O2 O H2O OH HO2 H2O2 AR

REACTIONS
H    + OH       => O    + H2           8.43E+09  1.00    6954.5
O    + H2       => H    + OH           1.81E+10  1.00    8901.8
H    + HO2      => H2   + O2           2.53E+13  0.00     695.5
H2   + O2       => H    + HO2          5.48E+13  0.00   57821.7
H    + HO2      => OH   + OH           2.53E+14  0.00    1887.7
OH   + OH       => H    + HO2          1.20E+13  0.00   40137.4
H    + HO2      => O    + H2O          5.00E+13  0.00     993.5
O    + H2O      => H    + HO2          1.05E+12  0.45   56430.8
H    + H2O2     => HO2  + H2           1.69E+12  0.00    3775.3
HO2  + H2       => H    + H2O2         7.23E+11  0.00   18677.8
H    + H2O2     => OH   + H2O          3.18E+14  0.00    8941.5
OH   + H2O      => H    + H2O2         2.40E+14  0.00   80473.5
OH   + H2       => H    + H2O          1.10E+09  1.30    3656.1
H    + H2O      => OH   + H2           1.08E+10  1.20   19095.1
OH   + OH       => H2   + O2           6.57E+10  0.26   29208.9
H2   + O2       => OH   + OH           1.69E+13  0.00   48085.4
OH   + OH       => O    + H2O          6.02E+07  1.30       0.0
O    + H2O      => OH   + OH           1.93E+09  1.16   17426.0
OH   + HO2      => H2O  + O2           5.00E+13  0.00     999.5
H2O  + O2       => OH   + HO2          1.43E+14  0.17   73320.3
OH   + H2O2     => HO2  + H2O          1.02E+13  0.00    1808.2
HO2  + H2O      => OH   + H2O2         2.83E+13  0.00   32785.5
HO2  + H2       => OH   + H2O          7.23E+11  0.00   18697.7
OH   + H2O      => HO2  + H2           8.01E+09  0.43   71929.4
HO2  + HO2      => H2O2 + O2           1.81E+13  0.00     993.5
H2O2 + O2       => HO2  + HO2          9.46E+14 -0.38   43714.0
O    + OH       => H    + O2           1.64E+12  0.28    -160.9
H    + O2       => O    + OH           2.23E+14  0.00   16790.2
O    + HO2      => OH   + O2           5.01E+13  0.00     999.5
OH   + O2       => O    + HO2          1.33E+13  0.18   56033.4
O    + H2O2     => H2O  + O2           8.43E+11  0.00    4212.4
H2O  + O2       => O    + H2O2         3.43E+10  0.52   89017.6
O    + H2O2     => OH   + HO2          8.43E+11  0.00    4232.3
OH   + HO2      => O    + H2O2         1.25E+09  0.64   16353.0
H2   + M        => H    + H    + M     2.23E+14  0.00   95972.1
 O2 /0.4/ H2O /6.5/
H2O  + M        => H    + OH   + M     3.49E+15  0.00  105112.3
 O2 /0.4/ H2O /6.5/
HO2  + M        => H    + O2   + M     2.11E+15  0.00   45701.0
 O2 /0.4/ H2O /6.5/
H2O2 + M        => OH   + OH   + M     1.20E+17  0.00   45502.3
 O2 /0.4/ H2O /6.5/
OH   + M        => O    + H    + M     1.40E+14  0.21  101337.0
 O2 /0.4/ H2O /6.5/
HO2  + M        => O    + OH   + M     6.63E+19 -0.43   63981.4
 O2 /0.4/ H2O /6.5/
O2   + M        => O    + O    + M     1.81E+18 -1.00  118027.8
 O2 /0.4/ H2O /6.5/
H    + H    + M => H2   + M            6.53E+17 -1.00       0.0
 O2 /0.4/ H2O /6.5/
H    + OH   + M => H2O  + M            2.25E+22 -2.00       0.0
 O2 /0.4/ H2O /6.5/
H    + O2   + M => HO2  + M            1.50E+15  0.00    -993.5
 O2 /0.4/ H2O /6.5/
OH   + OH   + M => H2O2 + M            9.07E+14  0.00   -5066.9
 O2 /0.4/ H2O /6.5/
O    + H    + M => OH   + M            3.00E+19 -1.00       0.0
 O2 /0.4/ H2O /6.5/
O    + OH   + M => HO2  + M            1.02E+17  0.00       0.0
 O2 /0.4/ H2O /6.5/
O    + O    + M => O2   + M            1.89E+13  0.00   -1788.3
 O2 /0.4/ H2O /6.5/
```

A.3 Cross-Current Dynamics

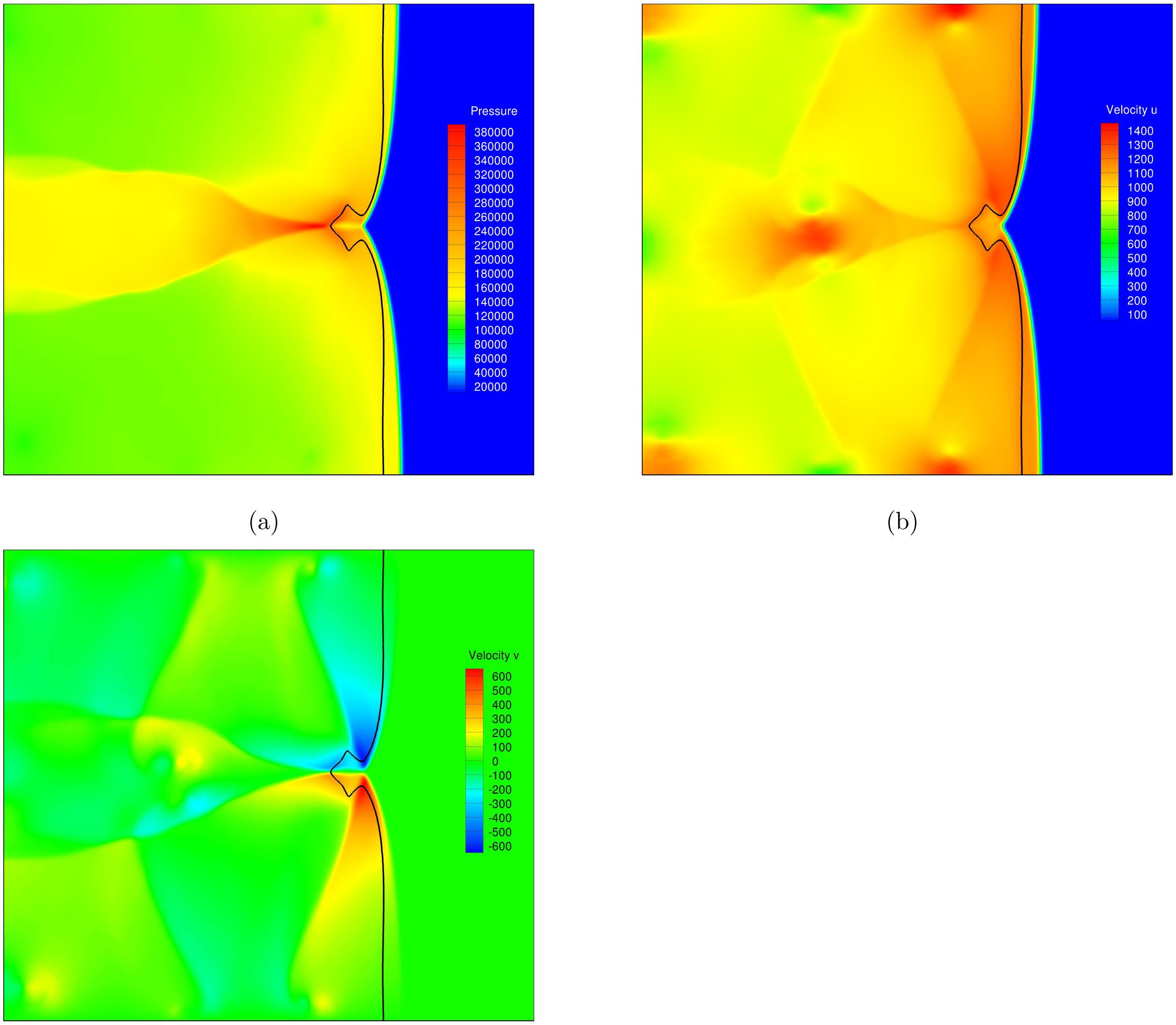

(a)

(b)

(c)

Figure A.1: Pressure (a), u-velocity (b), and v-velocity (c) at t = 232 μs with an isoline indicating the end of the induction zone.

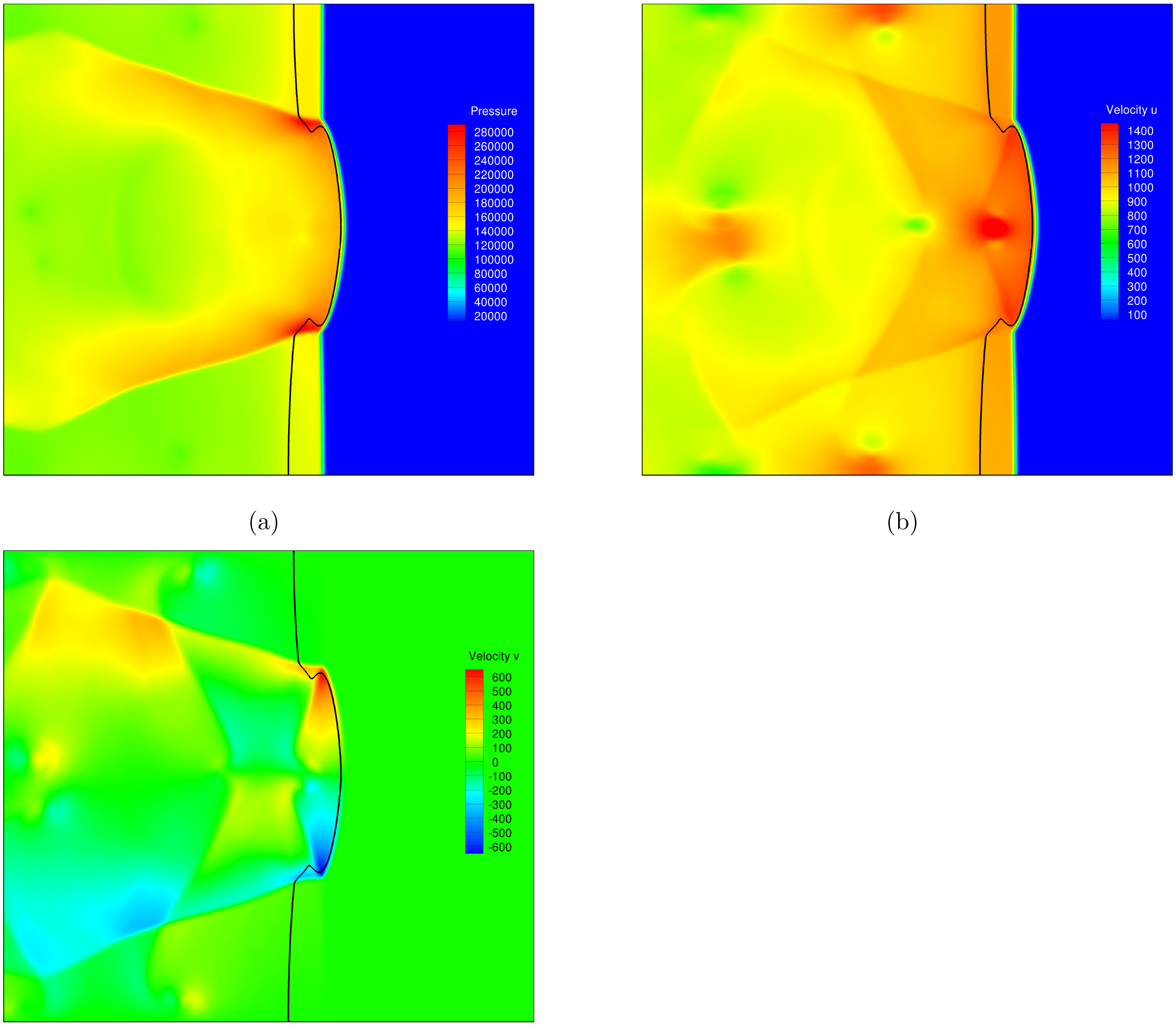

(a)

(b)

(c)

Figure A.2: Pressure (a), u-velocity (b), and v-velocity (c) at t = 240 μs with an isoline indicating the end of the induction zone.

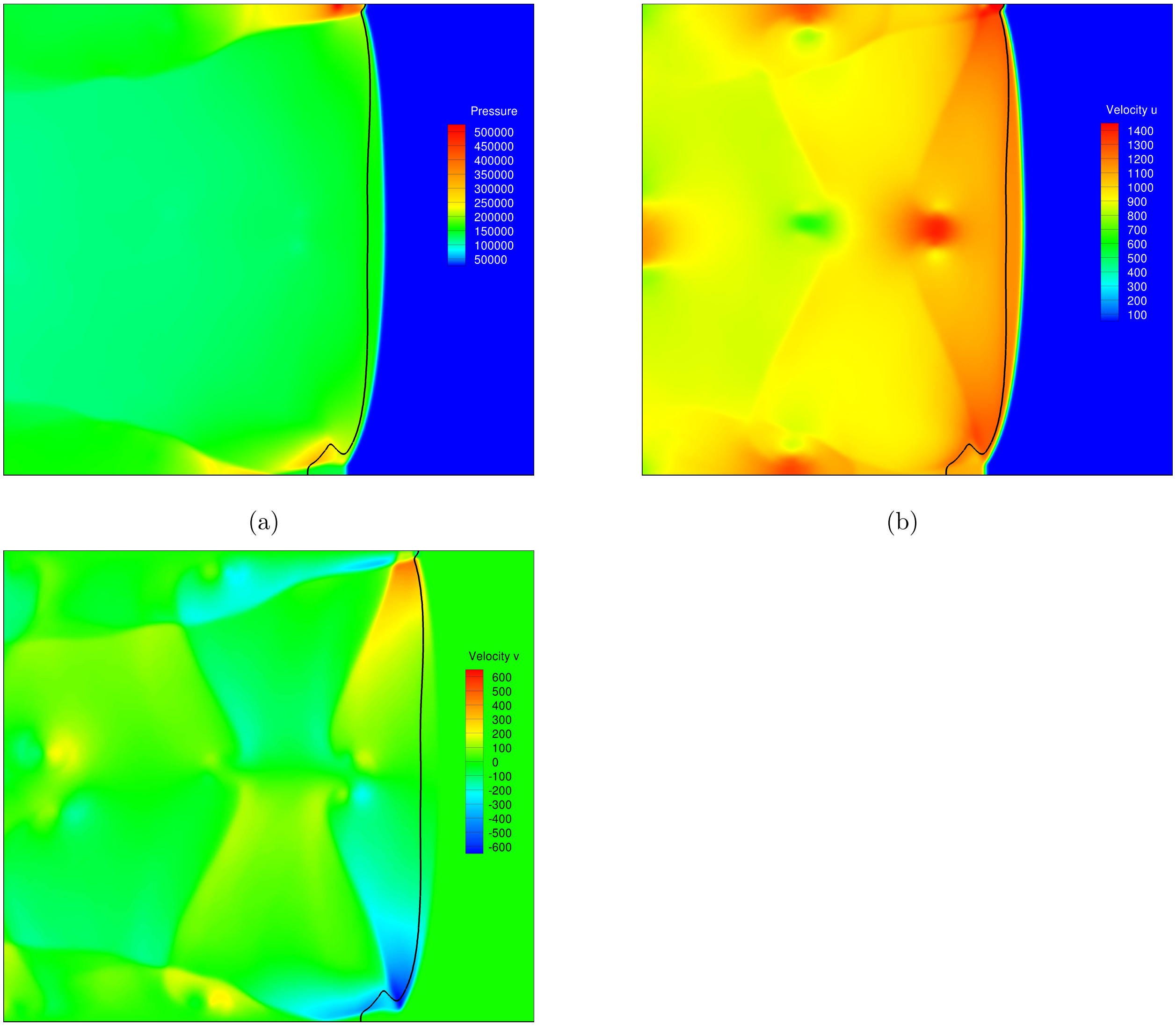

(a)

(b)

(c)

Figure A.3: Pressure (a), u-velocity (b), and v-velocity (c) at t = 248 μs with an isoline indicating the end of the induction zone.

A.4 Area-Average with One Detonation Cell at Later Times

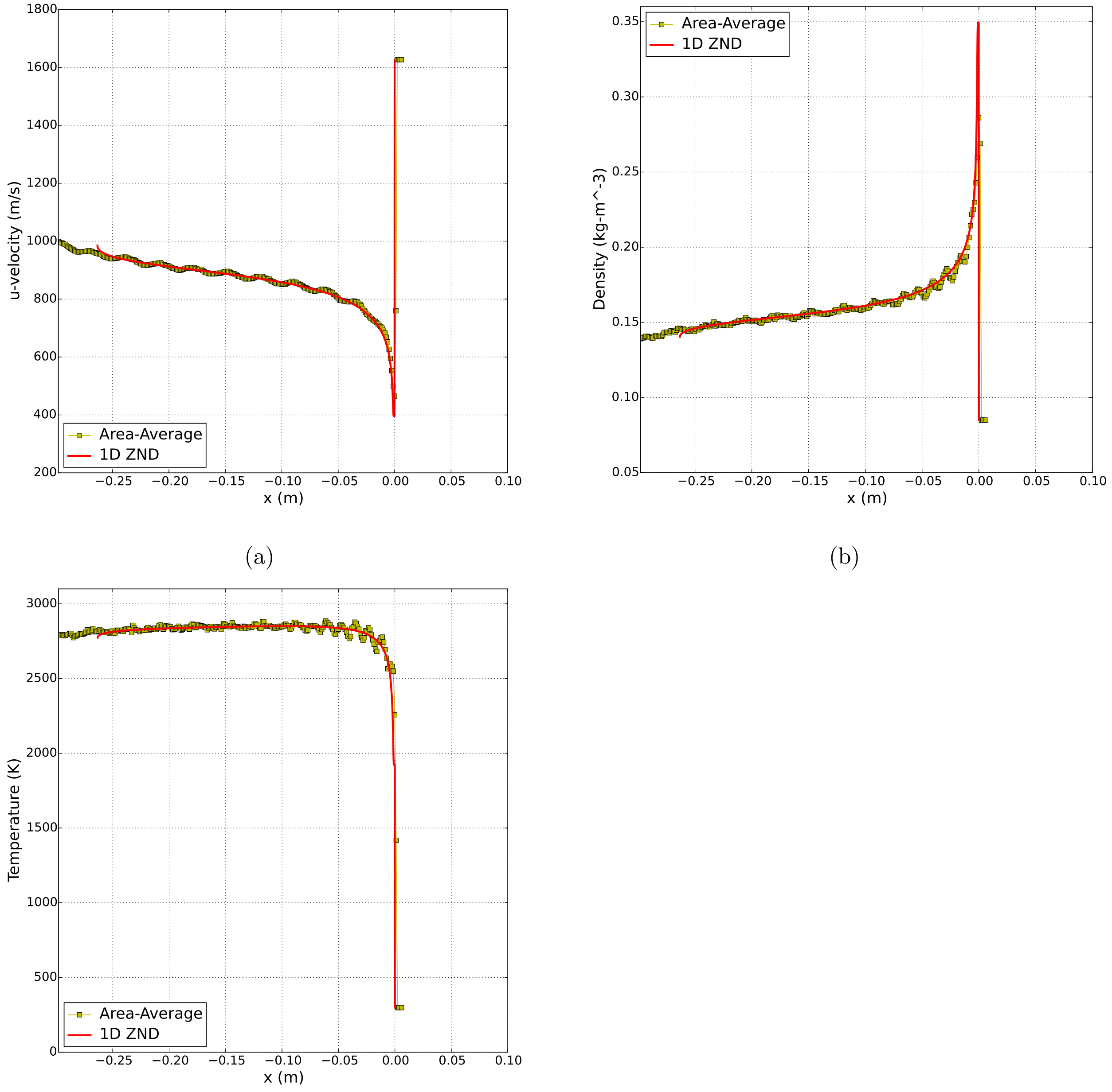

(a)

(b)

(c)

Figure A.4: Area-averaged u-velocity (a), density (b), and temperature (c) compared to the computed one-dimensional ZND solution at t = 575 μs.

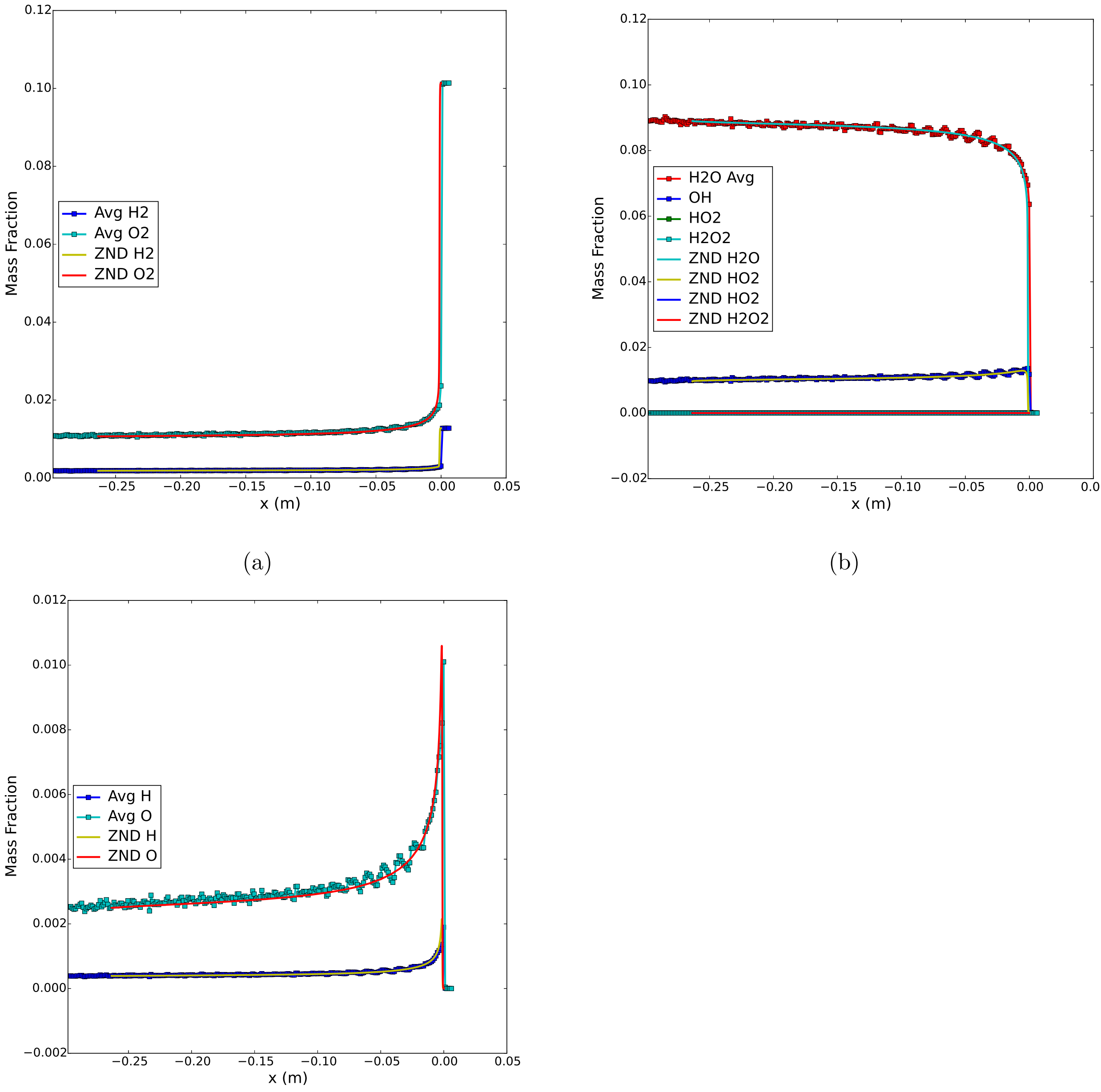

(a)

(b)

(c)

Figure A.5: Area-averaged mass fraction of species compared to the computed one-dimensional ZND solution at t = 575 μs.

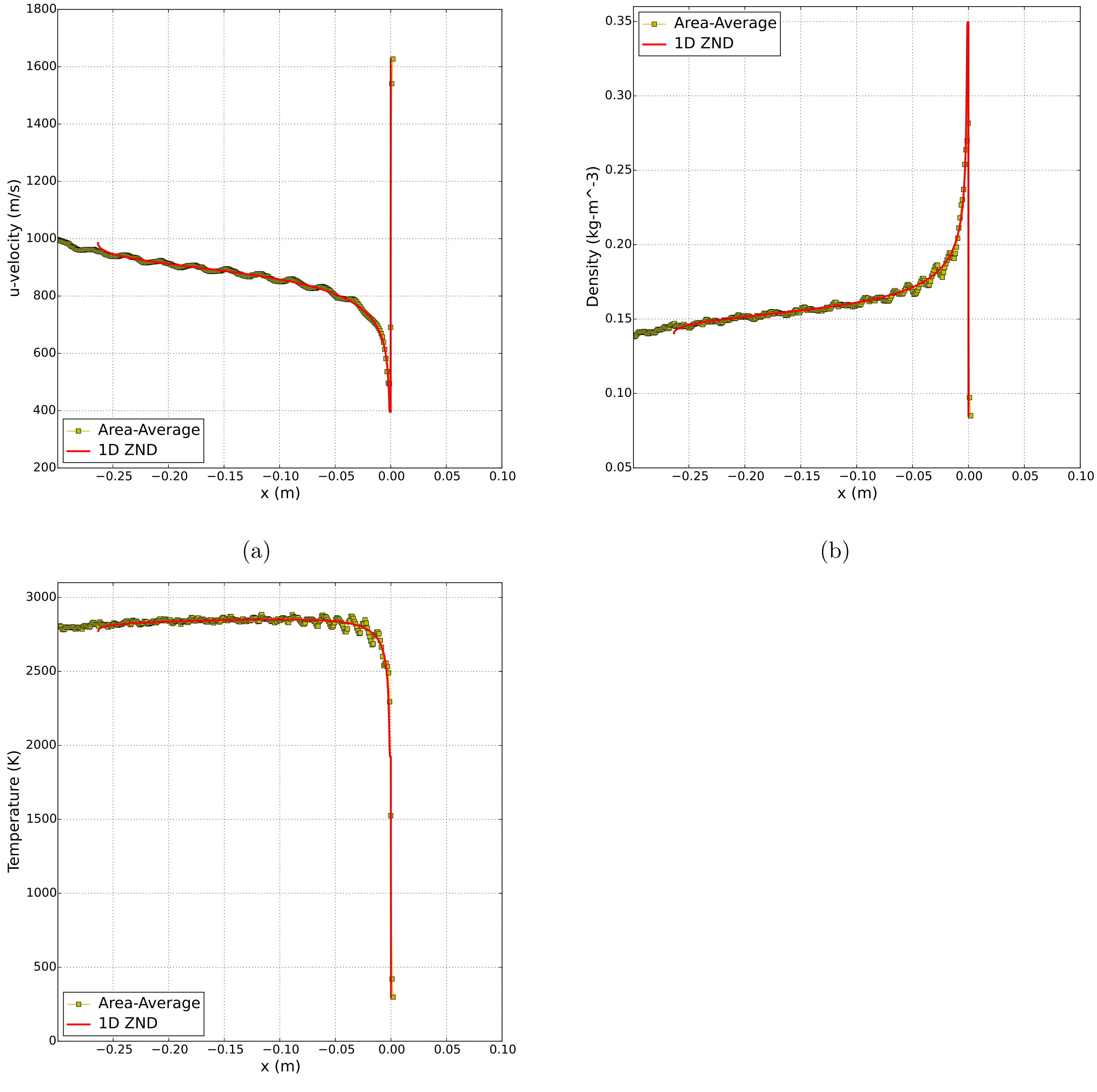

(a)

(b)

(c)

Figure A.6: Area-averaged u-velocity (a), density (b), and temperature (c) compared to the computed one-dimensional ZND solution at t = 605 μs.

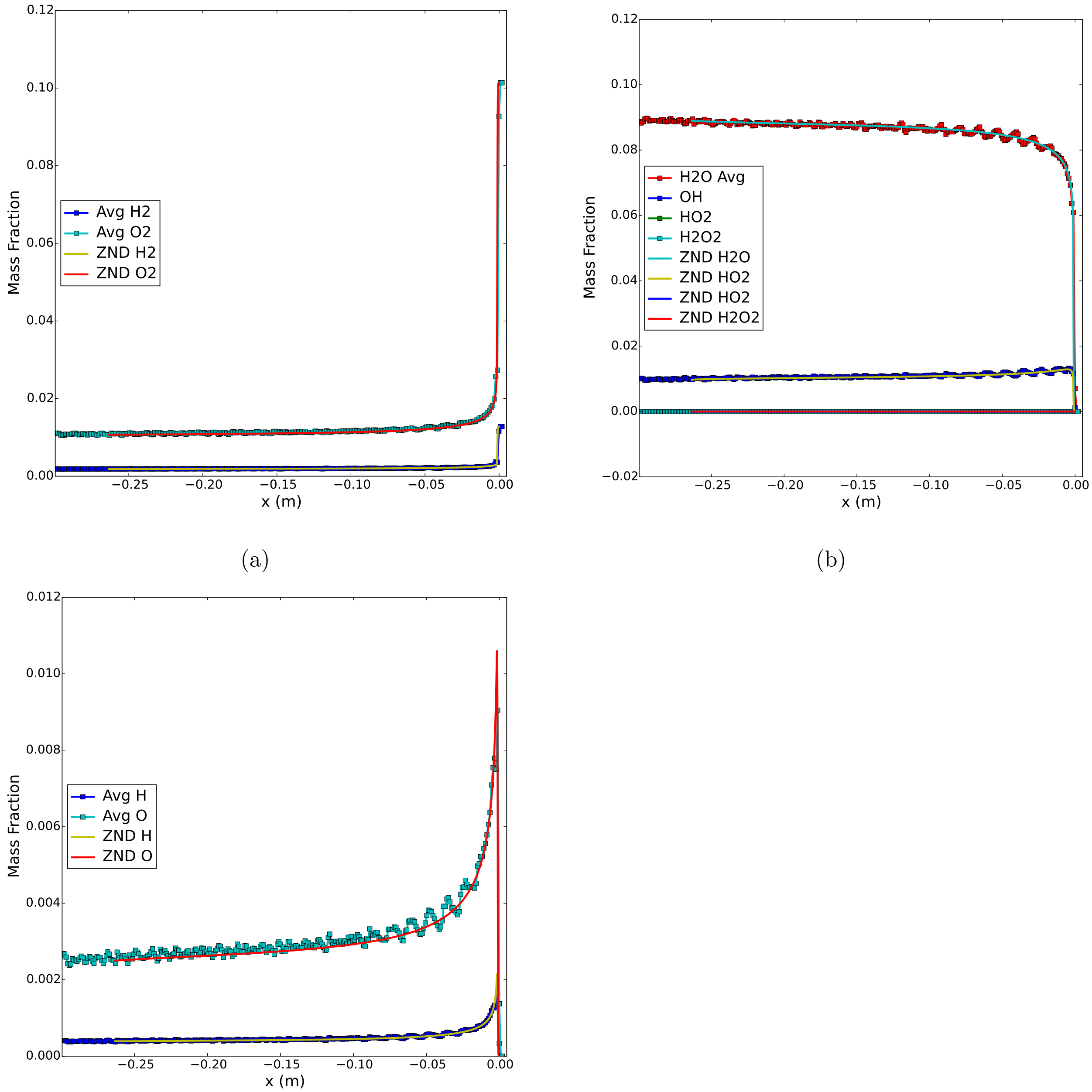

(a)

(b)

(c)

Figure A.7: Area-averaged mass fraction of species compared to the computed one-dimensional ZND solution at t = 605 μs.

A.5 Area-Averages During Transient Phase of Mach

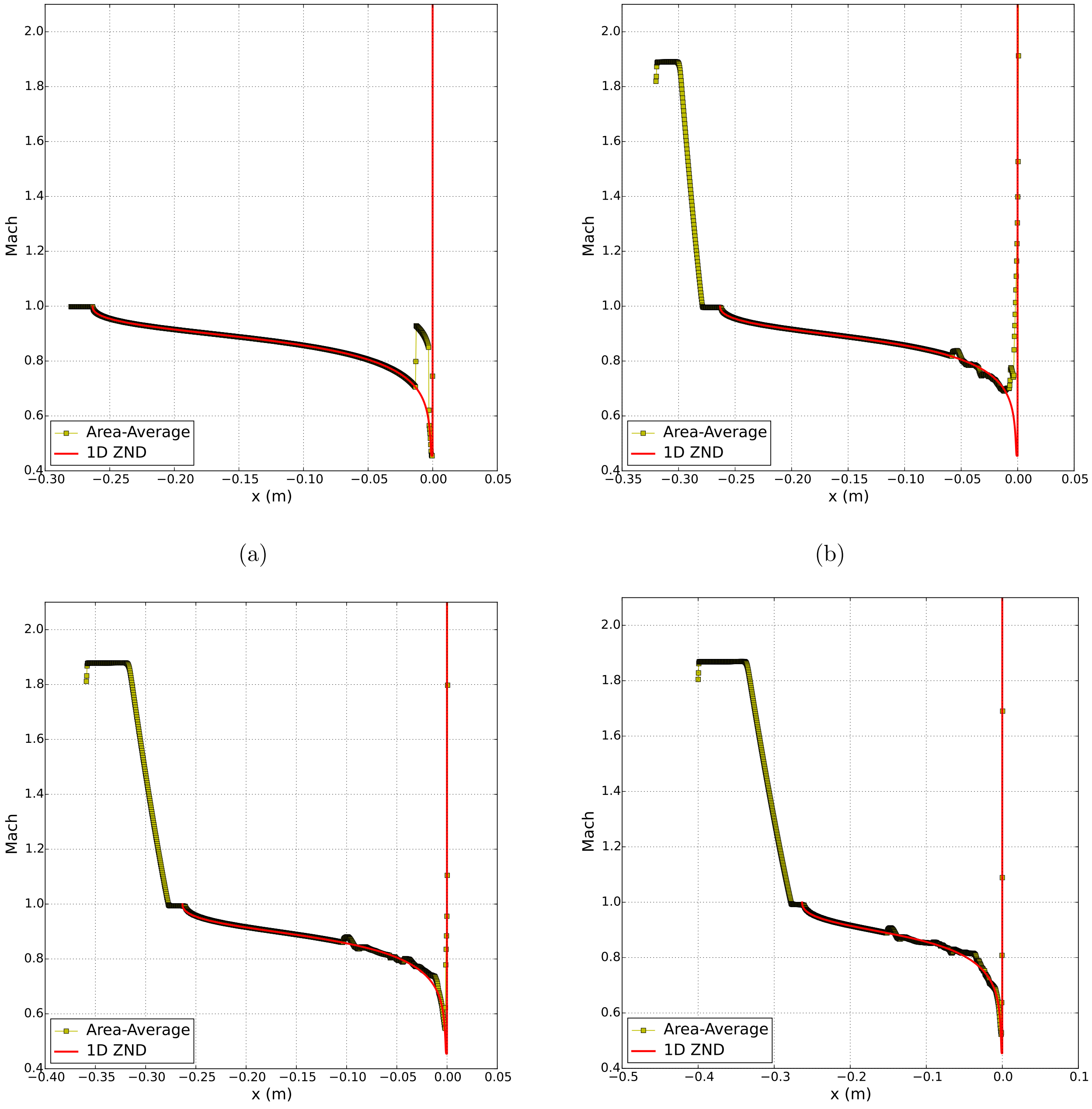

(a)

(b)

(c)

(d)

Figure A.8: Area-averaged Mach in reference frame attached to detonation front compared to the computed one-dimensional ZND solution at t = 0 (a), 25 (b), 50 (c), and 75 (d) μs.

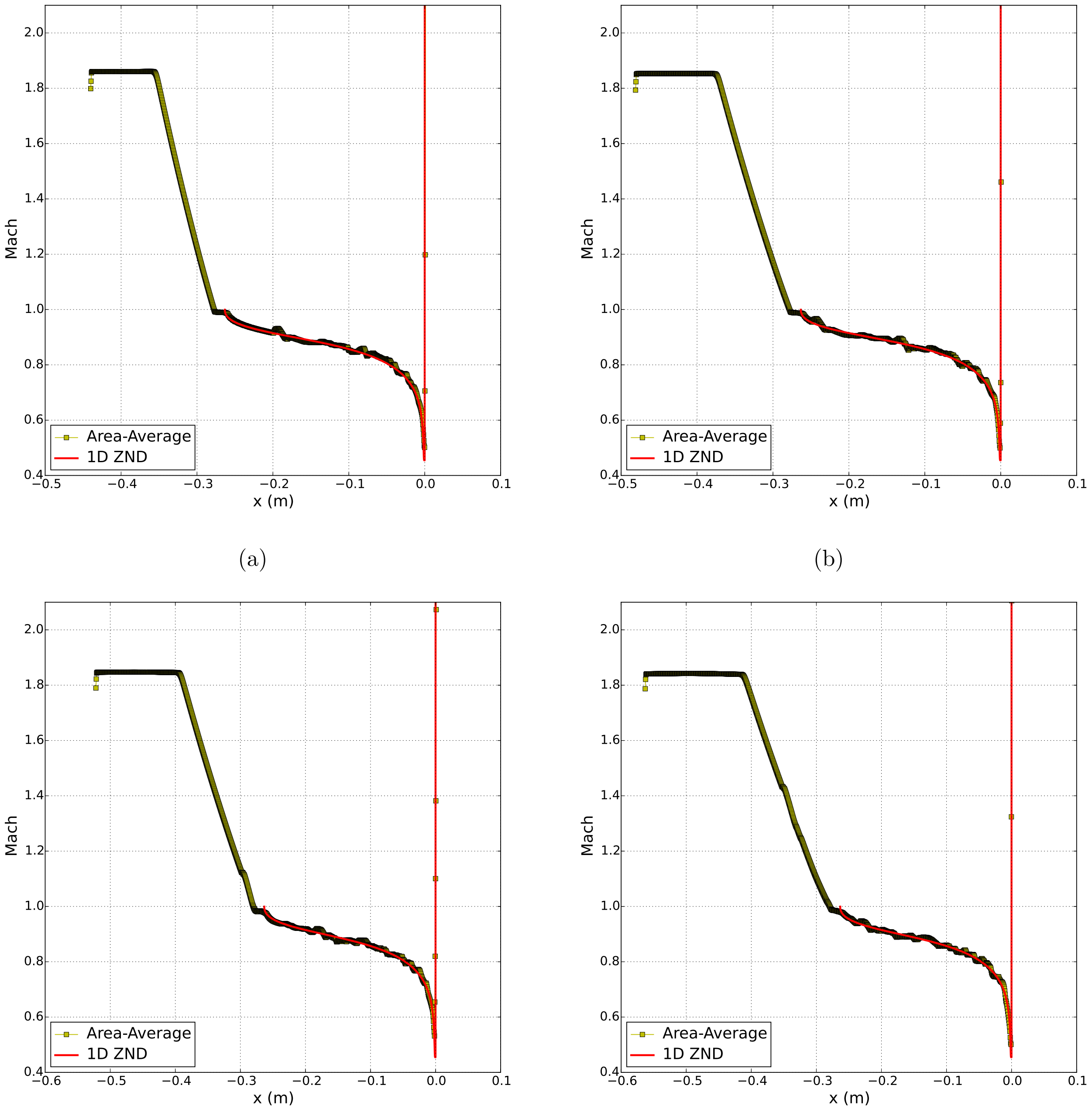

(a) (b)

(c) (d)

Figure A.9: Area-averaged Mach in reference frame attached to detonation front compared to the computed one-dimensional ZND solution at t = 100 (a), 125 (b), 150 (c), and 175 (d) μs.

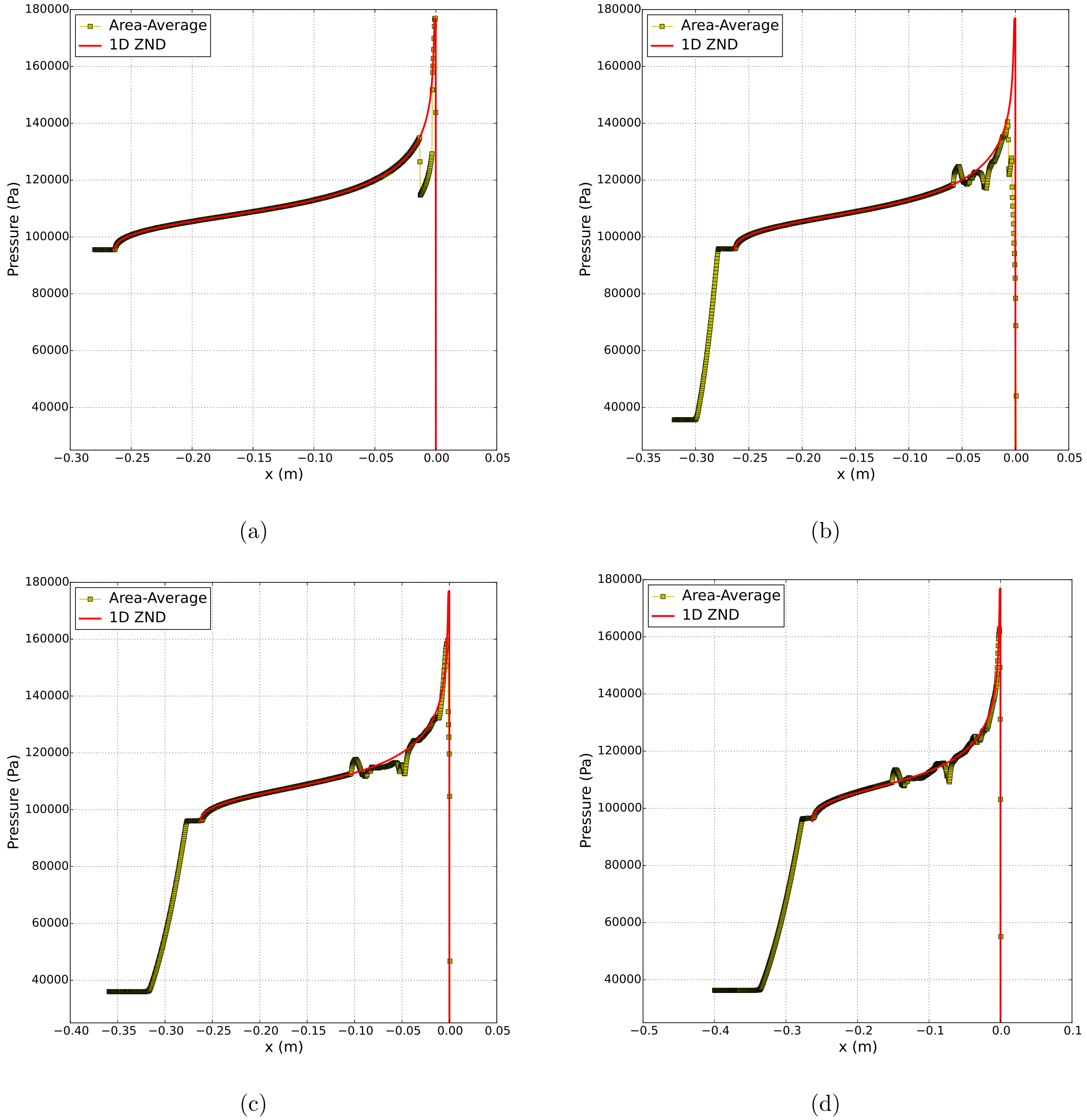

(a) (b)

(c) (d)

Figure A.10: Area-averaged pressure compared to the computed one-dimensional ZND solution at t = 0 (a), 25 (b), 50 (c), and 75 (d) μs.

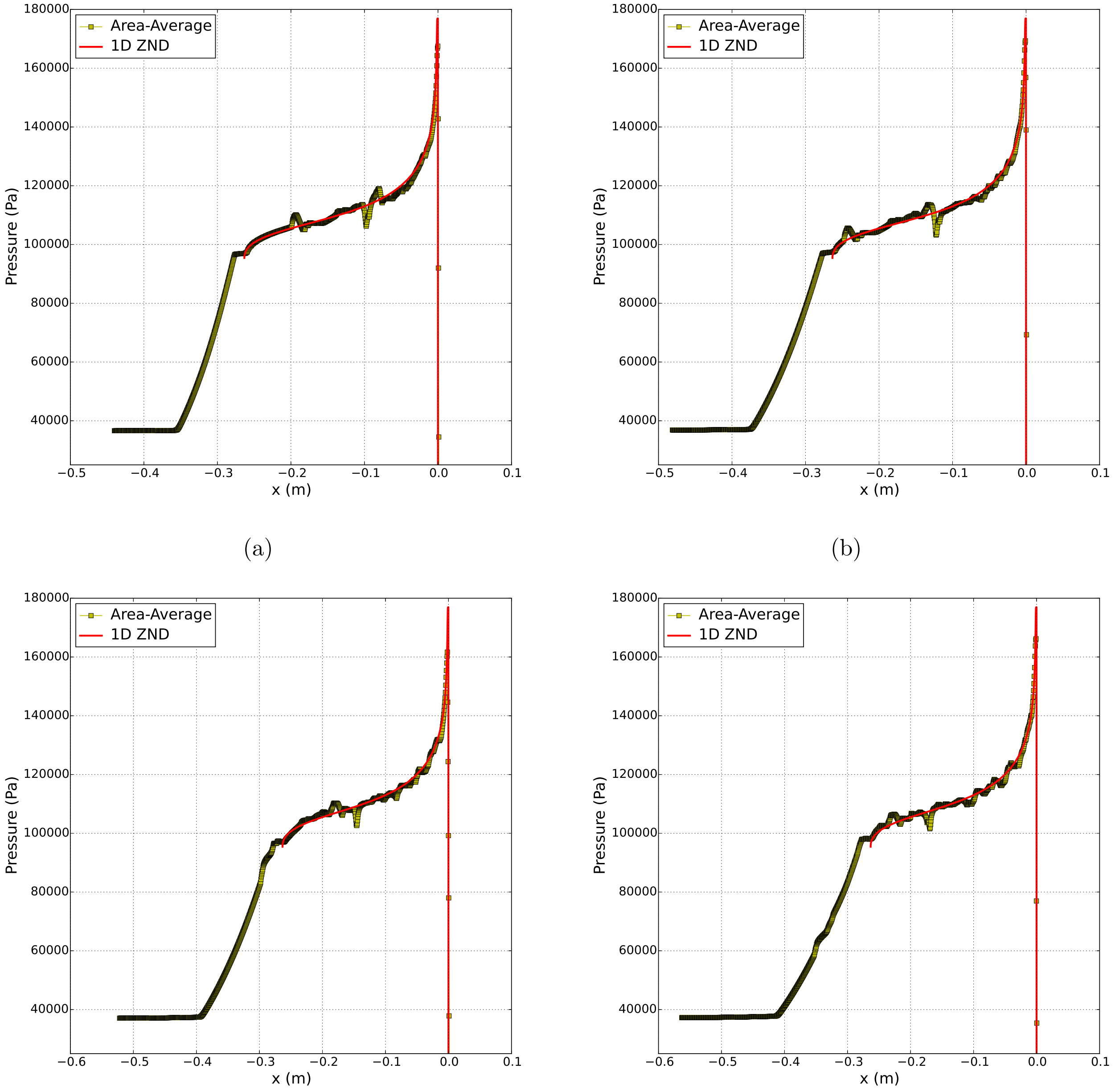

(a) (b) (c) (d)

Figure A.11: Area-averaged pressure compared to the computed one-dimensional ZND solution at t = 100 (a), 125 (b), 150 (c), and 175 (d) μs.

A.6 Detonations in Open/Closed Duct with Two Detonation Cells

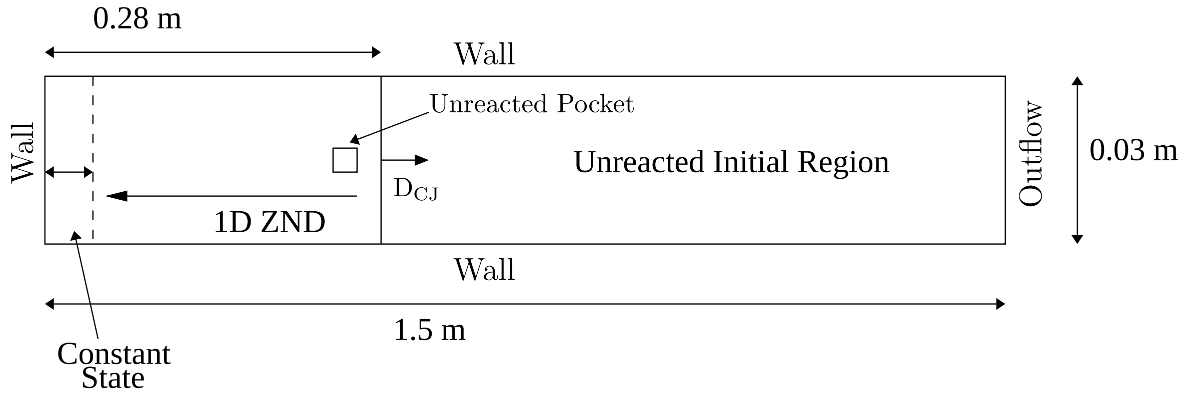

Figure A.12: The computational setup of detonations in a duct with an open and closed end that produced two detonation cells.

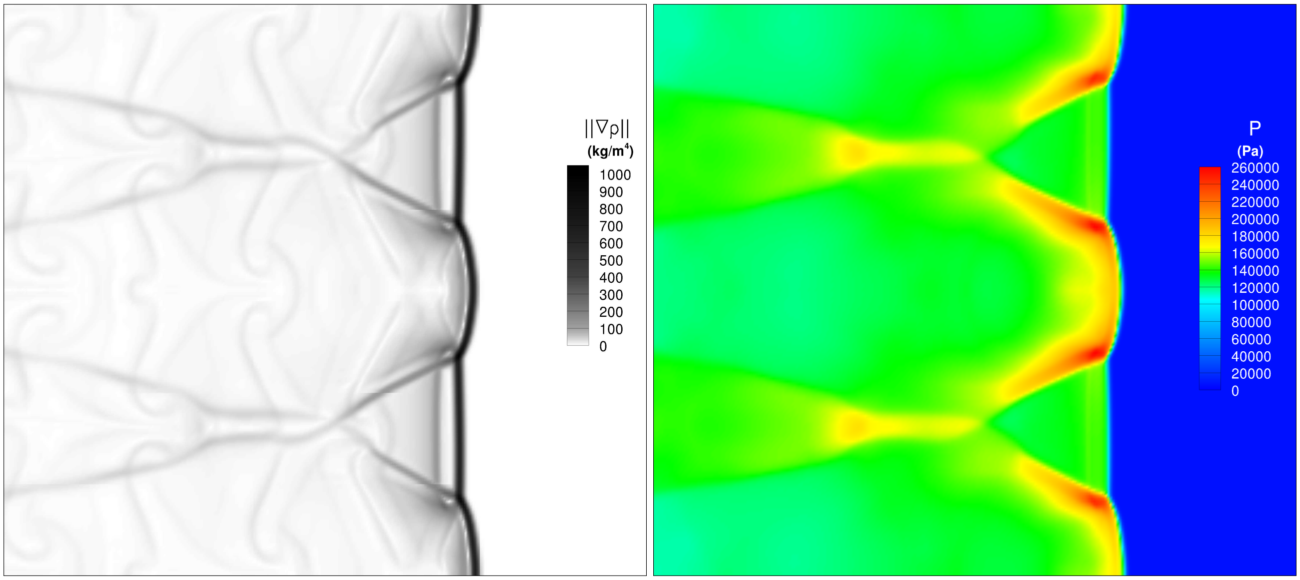

(a) (b)

Figure A.13: a). Density schlieren contour and b). pressure contour of the detonation front at t = 266 μs with two cells.

A.6.1 Area-Averaged and Particle Properties with Two Detonation Cells

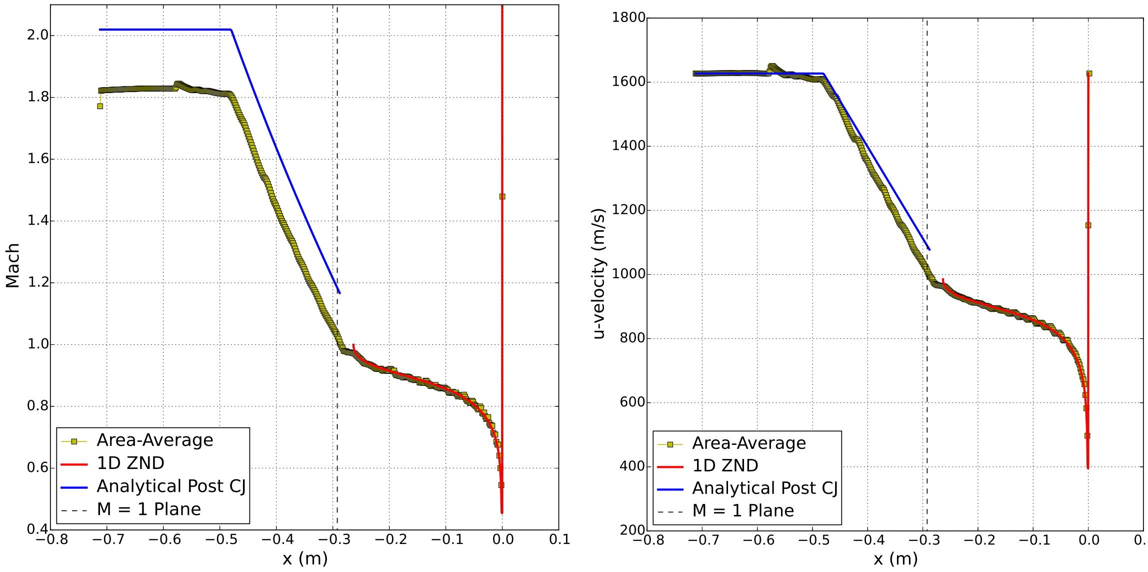

(a) Mach

(b) U-velocity

Figure A.14: Area-averaged Mach (a) and u-velocity (b) in the reference frame attached to the detonation front compared to the computed one-dimensional ZND solution and the analytical post CJ-structure at t = 266 μs.

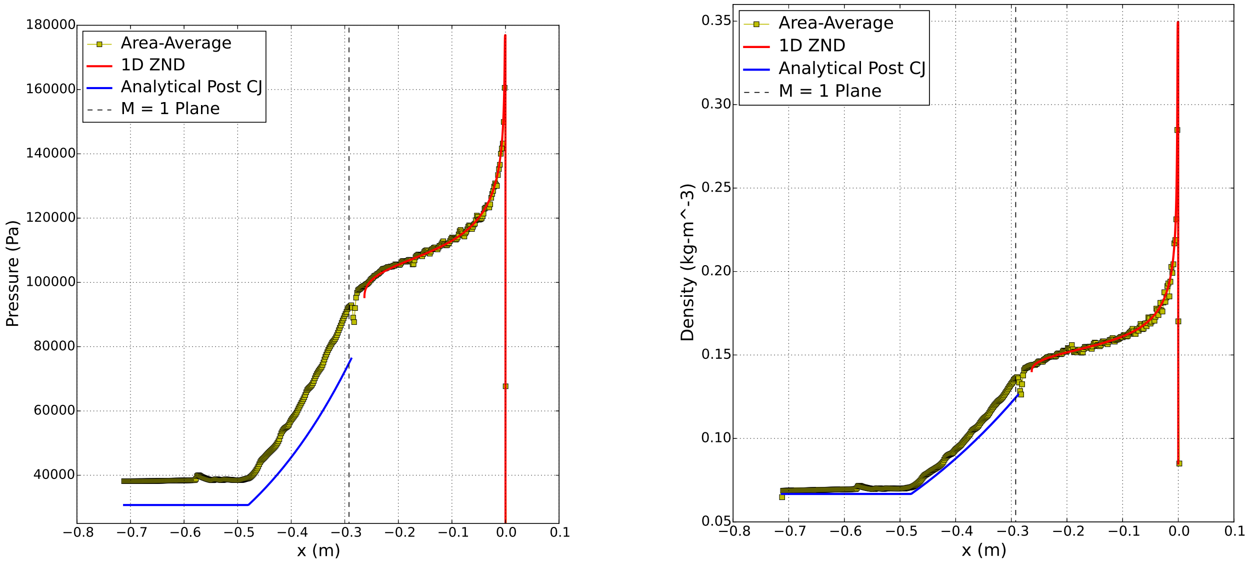

(a) Pressure

(b) Density

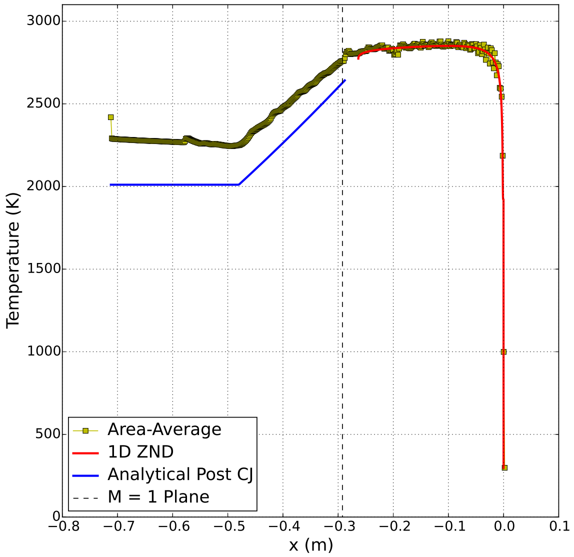

(c) Temperature

Figure A.15: Area-averaged pressure (a), density (b), and temperature (c) compared to the computed one-dimensional ZND solution and the analytical post CJ-structure at t = 266 μs.

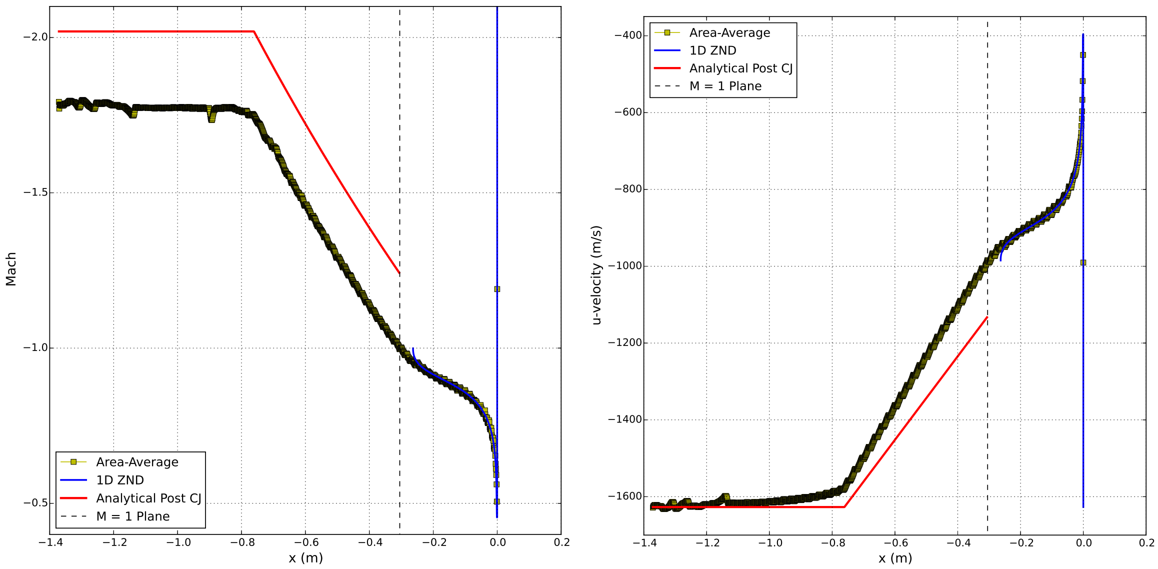

(a) Mach

(b) U-velocity

Figure A.16: Area-averaged Mach (a) and u-velocity (b) in the reference frame attached to the detonation front compared to the computed one-dimensional ZND solution and the analytical post CJ-structure at t = 670 μs.

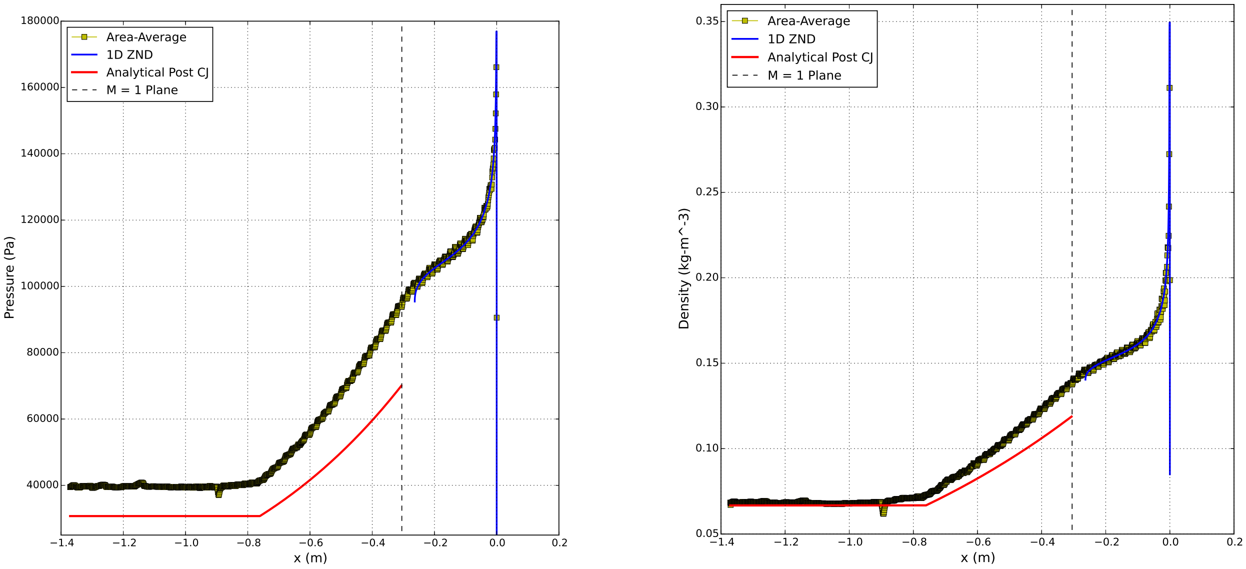

(a) Pressure

(b) Density

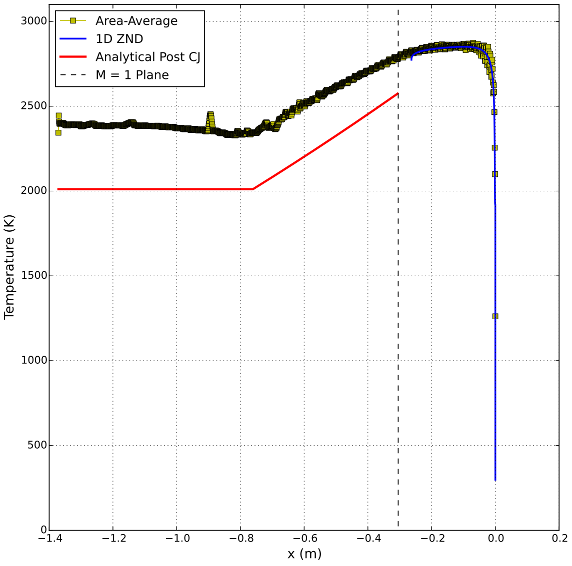

(c) Temperature

Figure A.17: Area-averaged pressure (a), density (b), and temperature (c) compared to the computed one-dimensional ZND solution and the analytical post CJ-structure at t = 670 μs.

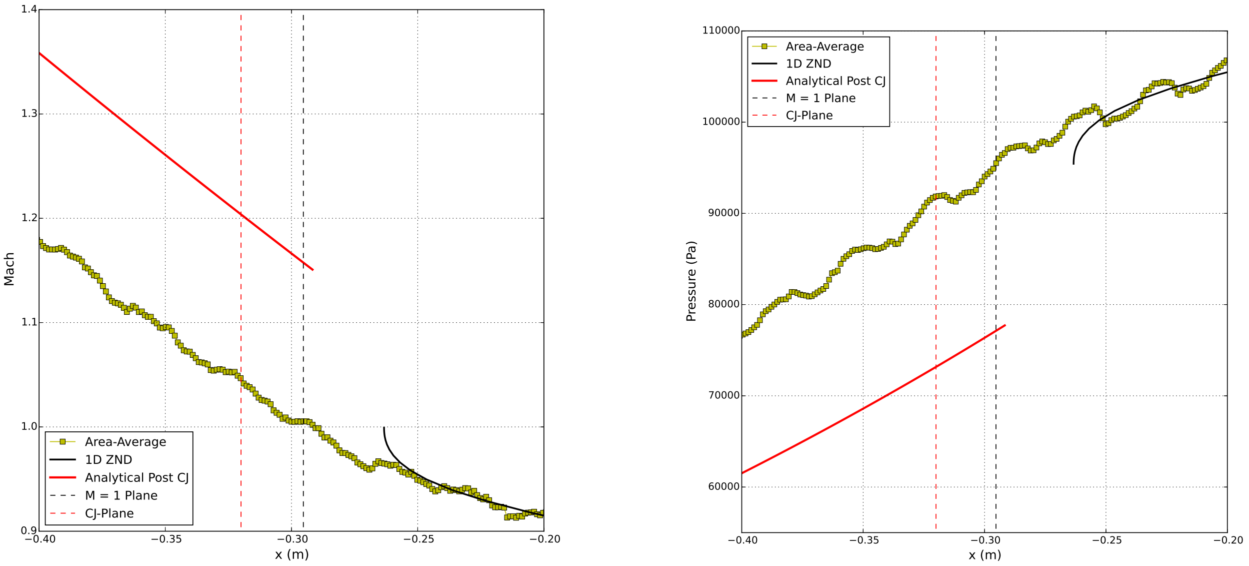

(a) Mach

(b) Pressure

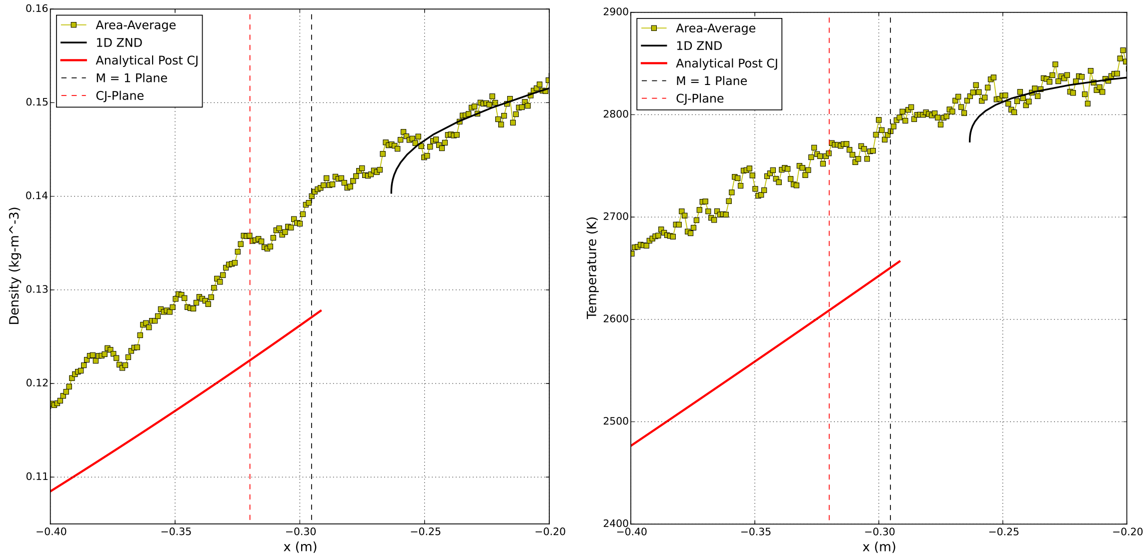

(c) Density

(d) Temperature

Figure A.18: Magnified view at t = 690 μs of the area-averaged Mach (a), pressure (b), density (c), and temperature (d) in the reference frame attached to the detonation front compared to the computed one-dimensional ZND solution and the analytical post CJ-structure. The sonic plane and CJ-plane are both also shown.

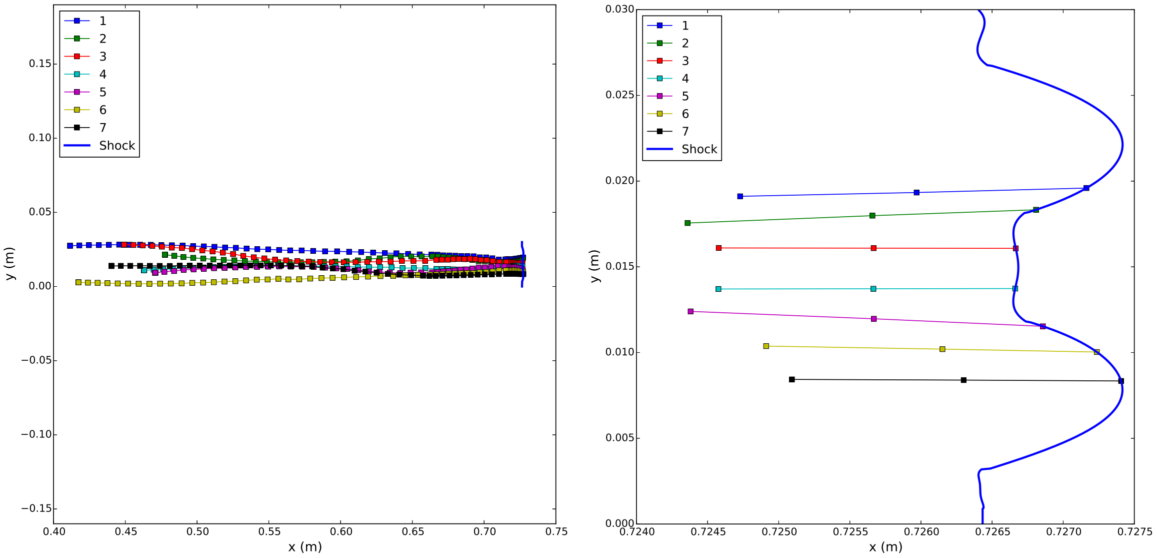

(a) (b)

Figure A.19: a). Shock reference frame of 7 particle paths and b). zoomed in view of the origin of the particle paths. The particles were tracked from t = 275 μs to 690 μs.

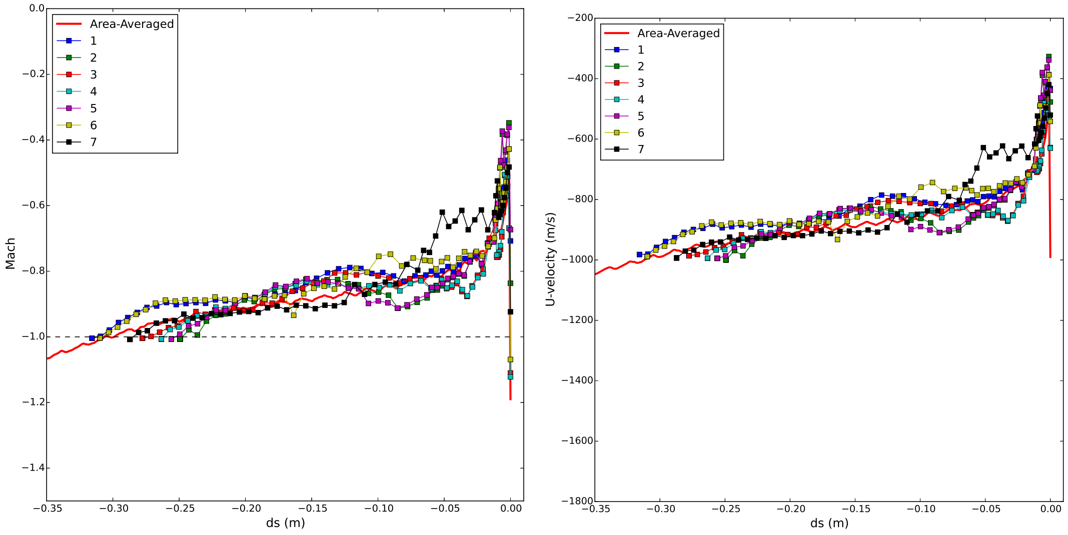

(a) (b)

Figure A.20: Flow properties of 7 randomly chosen particles that are tracked from the detonation front to after the sonic plane are plotted with the area-average for Mach (a) and u-velocity (b) in the reference frame attached to the shock.

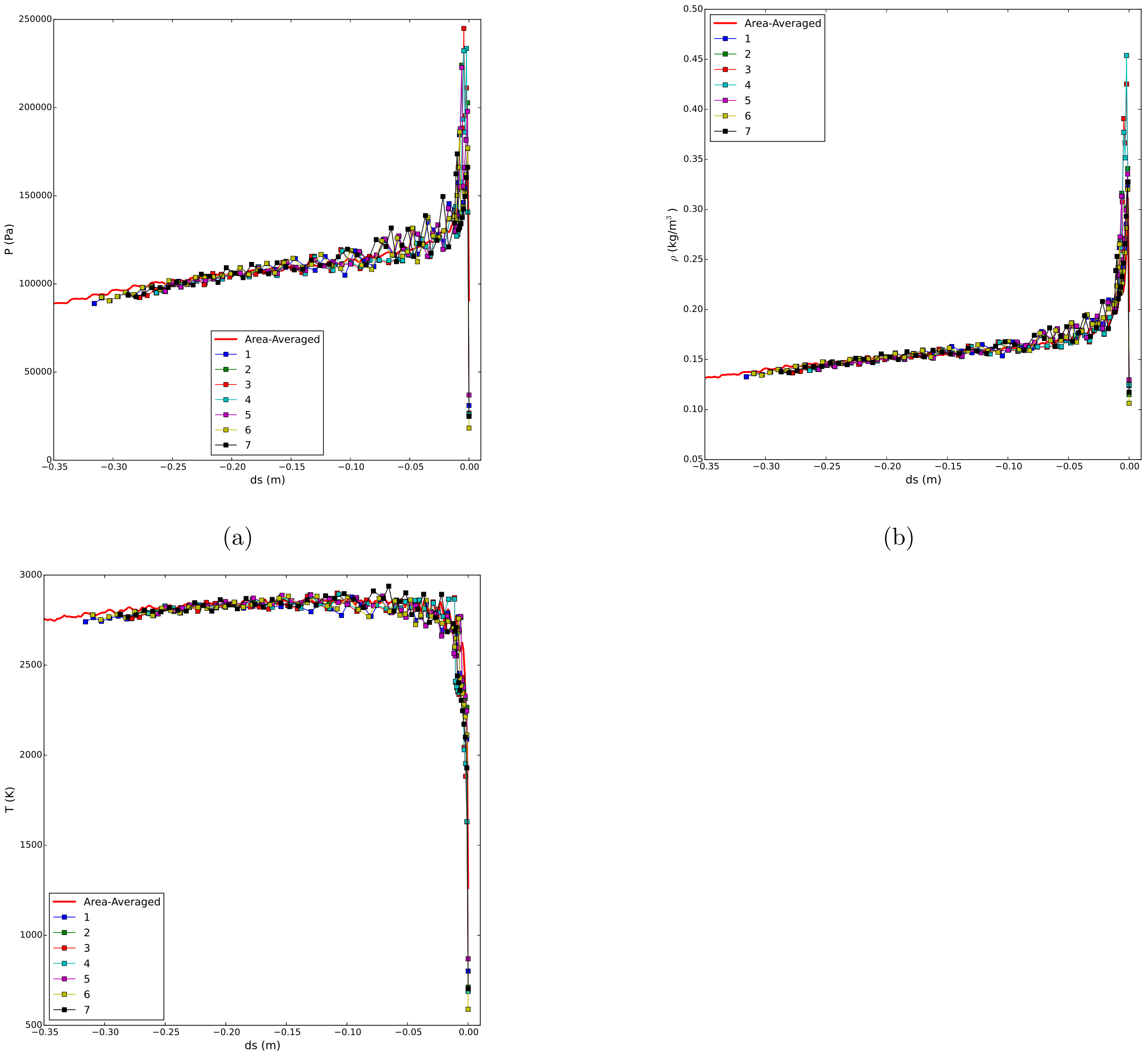

(a)

(b)

(c)

Figure A.21: Flow properties of 7 randomly chosen particles that are tracked from the detonation front to after the sonic plane are plotted with the area-average for pressure (a), density (b), and temperature (c).

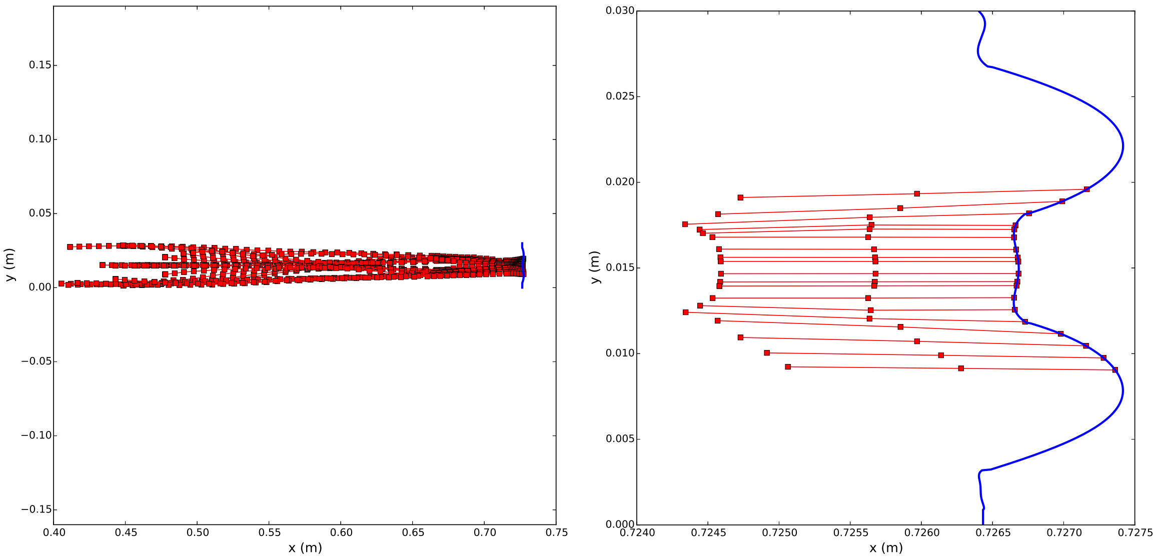

(a) (b)

Figure A.22: a). Shock reference frame of multiple particle paths and b). zoomed in view of the origin of the particle paths. The particles were tracked from t = 275 μs to 690 μs.